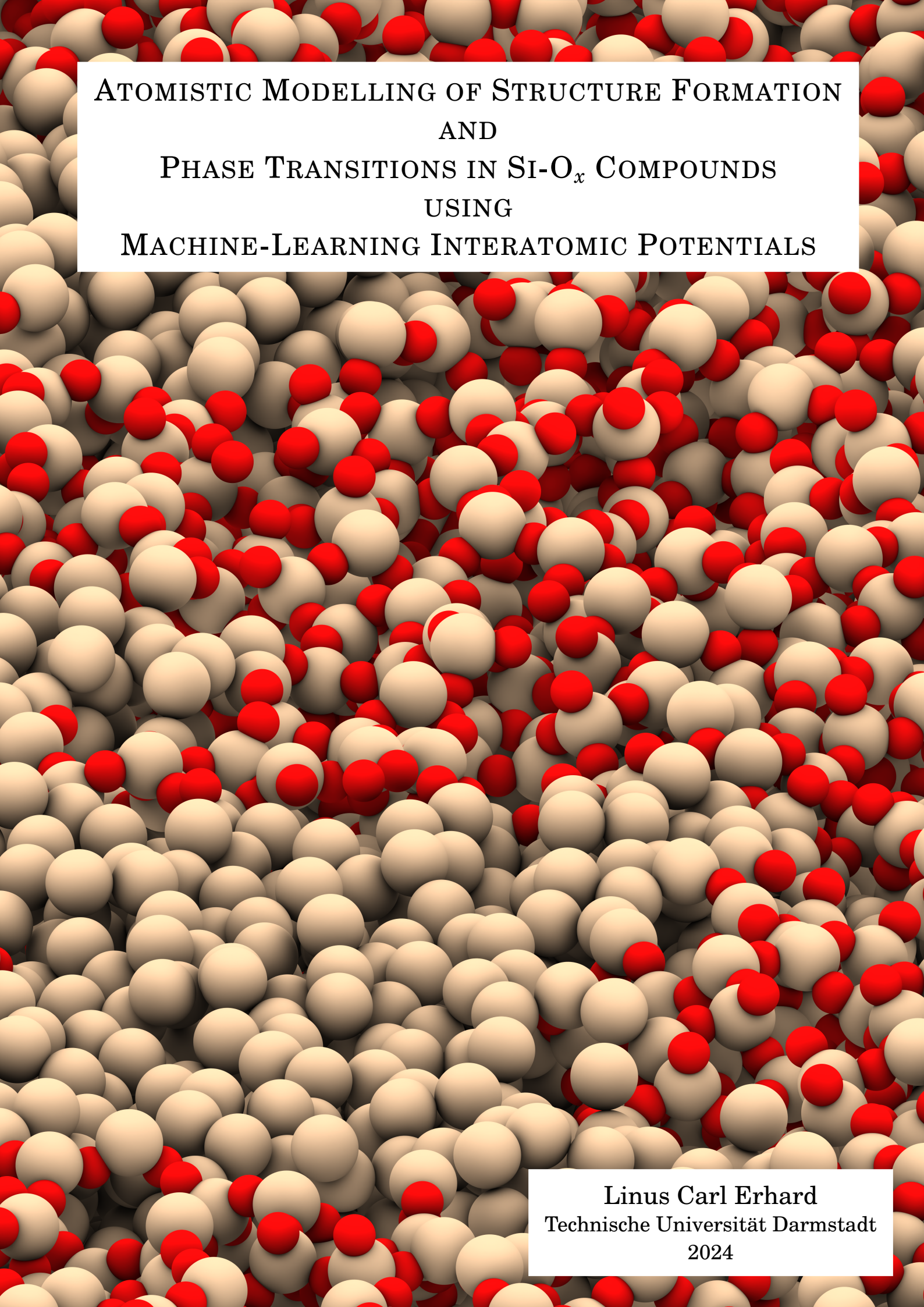

Atomistic Modelling of Structure Formation and Phase Transitions in Si-O_x Compounds using Machine-Learning Interatomic Potentials

Linus Carl Erhard
Technische Universität Darmstadt
2024

On the cover: Interface between amorphous silicon and amorphous silica within a structural model of silicon monoxide. Silicon atoms are marked brown and oxygen atoms are red.

Atomistic Modelling of Structure Formation and Phase Transitions in Si-O_x Compounds using Machine-Learning Interatomic Potentials

Zur Erlangung des akademischen Grades Doktor der Naturwissenschaften (Dr. rer. nat.)
genehmigte Dissertation vorgelegt
von Linus Carl Erhard

Fachgebiet: Materialmodellierung
Fachbereich: Material- und Geowissenschaften
Technische Universität Darmstadt

Berichter:	Prof. Dr. Karsten Albe Technische Universität Darmstadt
Mitberichter:	Prof. Dr. Volker Deringer University of Oxford
1. Prüfer:	Prof. Dr. Hongbin Zhang Technische Universität Darmstadt
2. Prüfer:	Prof. Dr. Clemens Prescher Universität Freiburg

Tag der Einreichung:	28.06.2024
Tag der Prüfung:	02.09.2024
Jahr der Veröffentlichung:	2024

Darmstadt 2024
D17

Please cite this document as:
URN: urn:nbn:de:tuda-tuprints-281919
URL: https://tuprints.ulb.tu-darmstadt.de/id/eprint/28191

Erhard, Linus Carl: Atomistic Modelling of Structure Formation and Phase Transitions in Si-O_x Compounds using Machine-Learning Interatomic Potentials
Darmstadt, Technische Universität Darmstadt
Jahr der Veröffentlichung auf TUprints: 2024
URN: urn:nbn:de:tuda-tuprints-281919
URL: https://tuprints.ulb.tu-darmstadt.de/id/eprint/28191
Tag der mündlichen Prüfung: 02.09.2024

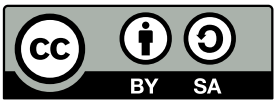

Erklärung laut Promotionsordnung

§8 Abs. 1 lit. c PromO

Ich versichere hiermit, dass die elektronische Version meiner Dissertation mit der schriftlichen Version übereinstimmt.

§8 Abs. 1 lit. d PromO

Ich versichere hiermit, dass zu einem vorherigen Zeitpunkt noch keine Promotion versucht wurde. In diesem Fall sind nähere Angaben über Zeitpunkt, Hochschule, Dissertationsthema und Ergebnis dieses Versuchs mitzuteilen.

§9 Abs. 1 PromO

Ich versichere hiermit, dass die vorliegende Dissertation – abgesehen von den in ihr ausdrücklich genannten Hilfen – selbstständig verfasst wurde und dass die „Grundsätze zur Sicherung guter wissenschaftlicher Praxis an der Technischen Universität Darmstadt“ und die „Leitlinien zum Umgang mit digitalen Forschungsdaten an der TU Darmstadt“ in den jeweils aktuellen Versionen bei der Verfassung der Dissertation beachtet wurden.

§9 Abs. 2 PromO

Die Arbeit hat bisher noch nicht zu Prüfungszwecken gedient.

Darmstadt, October 7, 2024

Linus Carl Erhard

Abstract

Silica is used in a wide range of applications from catalysis to construction to microelectronics. The related silicon monoxide is promising for applications as an anode material in lithium batteries. Although these materials have been extensively studied for more than a century, there are still many open questions. For example, the high-pressure transformations of silica are not fully understood. Moreover, in the case of silicon monoxide, there is not even an atomistic structure model that captures the complexity of the structure.

In this work, we use atomistic modelling to investigate these problems. For this purpose, we developed several machine learning interatomic potentials (MLIP). First, we developed a Gaussian approximation potential (GAP) model based on a database with focus on bulk silica. Later, we switched to the atomic cluster expansion (ACE) framework. The final ACE potential is fitted to a more comprehensive training database labeled with energies and forces from strongly constrained and appropriately normed (SCAN) exchange-correlation density functional theory (DFT) data. The database covers a wide range of structures, including amorphous and crystalline silica, silica surfaces, high-pressure silica, and silicon-silica interfaces. Several approaches were used to build the database including 'batch' learning and active learning. Moreover, we present an active learning technique that extracts DFT feasible small-scale images from large-scale simulations (Chapter 3). The MLIPs are extensively tested in reproducing the thermodynamics of the systems and show excellent behavior, outperforming existing classical models. Nevertheless, to generate realistic amorphous structures of silica, we rely on a 'hybrid' protocol using a combination of our MLIP and a classical interatomic potential (Chapter 4).

We apply the ACE potential to two cases. First, we study the high-pressure behavior of amorphous silica and quartz under shock (Chapter 5). We find that there is an intermediate structure between the amorphous state and the crystalline stable state of stishovite. This phase is based on the defective nickel arsenide (d-NiAs) structure. The structure has a disordered silicon sublattice and an ordered hexagonal close-packed (HCP) oxygen sublattice. While the oxygen lattice appears to form fast on the molecular dynamics (MD) time scales, the ordering of the silicon and hence the formation of stishovite takes significantly longer. Moreover, we found that a direct transition between quartz and rosiaite-structured silica is also possible, which seems to require certain strain boundary conditions.

Second, we generate structural models of silicon monoxide using melt-quench simulations (Chapter 6). These models show the same nanoscale segregation of silicon and silica as observed in experiment. Moreover, the energetics, grain sizes and X-ray structure factors of these models are in excellent agreement with the experiment. Using 20 ns annealing simulations, we are able to partially crystallize these structures and generate structural models with crystalline silicon in an amorphous silica matrix.

Zusammenfassung

Siliziumoxide sind ein äußerst relevantes Forschungsgebiet. Siliziumdioxid wird beispielsweise in einem breiten Spektrum von Anwendungen eingesetzt, von der Katalyse über die Bauindustrie bis hin zur Mikroelektronik. Das verwandte Siliziummonoxid ist vielversprechend für Anwendungen als Anodenmaterial in Lithiumbatterien. Obwohl diese Materialien seit mehr als einem Jahrhundert eingehend untersucht werden, gibt es noch viele offene Forschungsfragen. So sind beispielsweise die Hochdruckphasenübergänge von Siliziumdioxid noch nicht vollständig verstanden. Für Siliziummonoxid gibt es bis heute noch kein atomistisches Strukturmodell, das die Komplexität dieser Struktur erfasst.

In dieser Arbeit wurden atomistische Simulationen benutzt, um mehrere Probleme in diesem System zu analysieren. Zu diesem Zweck wurden mehrere interatomare Potentiale auf maschinellen Lernen („machine-learning interatomic potentials“, MLIP) basierend entwickelt, mit einem ersten Modell basierend auf den Gaußschen Näherungspotentialen („Gaussian approximation potentials“, GAP) und einem finalen Modell basierend auf der atomaren Clusterexpansion („atomic cluster expansion“, ACE). Das finale ACE Potential wurde auf eine Trainingsdatenbank gefittet, die mit Energien und Kräften aus stark eingeschränkten und angemessen normierten („strongly constrained and appropriately normed“, SCAN) Austauschkorrelationsdaten der Dichtefunktionaltheorie (DFT) berechnet wurden. Die Datenbank deckt ein breites Spektrum an Strukturen ab, darunter amorphes und kristallines Siliziumdioxid, Siliziumdioxid-Oberflächen, Hochdruck-Siliziumdioxid und Grenzflächen zwischen Siliziumdioxid und Silizium. Für den Aufbau der Datenbank wurden verschiedene Ansätze wie „Batch“-Lernen, aktives Lernen und unser eigenes aktives Lernverfahren verwendet, das DFT-fähige kleine Strukturen aus großen Simulationen extrahiert (Kapitel 3). Die MLIPs zeigen eine ausgezeichnete Genauigkeit in der Beschreibung der Thermodynamik des Systems und übertreffen existierende klassische interatomare Potentiale. Um realistische amorphe Strukturen von Siliziumdioxid zu erzeugen, war es jedoch nötig ein „hybrides“ Verfahren zu benutzen, das eine Kombination aus unserem MLIP und einem klassischen interatomaren Modell beinhaltet (Kapitel 4).

Das ACE Potential wurde auf zwei Fälle angewendet. Zunächst wurde das Hochdruckverhalten von amorphem Siliziumdioxid und Quarz unter Schock untersucht (Kapitel 5). Es wurde festgestellt, dass sich als Zwischenzustand zwischen dem amorphen Zustand und dem kristallinen stabilen Stishovit eine weitere Phase mit der defekten Nickelarsenidstruktur (d-NiAs) bildet. Diese Struktur hat ein ungeordnetes Silizium-Untergitter und ein geordnetes hexagonal dicht gepacktes (HCP) Sauerstoff-Untergitter. Während sich das Sauerstoffgitter auf der Zeitskala der Molekulardynamik (MD) schnell zu bilden scheint, dauert die Ordnung des Siliziums und damit die Bildung von Stishovit wesentlich länger. Darüber hinaus wurde festgestellt, dass auch ein direkter Übergang zwischen Quarz und Siliziumdioxid in der Rosiait Struktur möglich ist, für den bestimmte Dehnungsrandbedingungen erforderlich zu sein scheinen.

Als zweite Anwendung wurden Strukturmodelle von Siliziummonoxid mit Hilfe von Schmelzabschrecksimulationen erstellt (Kapitel 6). Diese Modelle zeigen die gleiche

Entmischung von Silizium und Siliziumdioxid auf der Nanoskala wie sie im Experiment beobachtet wird. Darüber hinaus stimmen Energetik, Korngrößen und Röntgenstrukturfaktoren dieser Modelle sehr gut mit den Experimenten überein. Durch Glühsimulationen mit einer Dauer von 20 ns wurden diese Strukturen teilweise kristallisiert und es konnten Strukturmodelle mit kristallinem Silizium innerhalb einer amorphen Siliziumdioxidmatrix konnten erstellt werden.

Acknowledgements – Danksagung

Zuallererst möchte ich mich bei Prof. Dr. Karsten Albe bedanken, dafür dass Du mich seit meiner Bachelorarbeit unterstützt hast, mir zahlreiche Möglichkeiten eröffnet hast, mir viele Freiheiten im Rahmen meiner Forschung gegeben hast und natürlich für die vielen aufschlussreichen Diskussionen. Ich habe nie so viel gelernt, wie in der Zeit meiner Promotion und ohne Dich wäre dies nicht möglich gewesen.

Besonders möchte ich mich auch bei Prof. Dr. Volker Deringer bedanken, dafür dass Du mich zweimal in Deiner Gruppe in Oxford willkommen geheißen hast und Dich nun bereit erklärt hast, als Zweitgutachter der Arbeit zu dienen. In der Zeit in Oxford habe ich unglaublich viel mitgenommen, sowohl von Dir als auch von Deinen vielen Gruppenmitgliedern. Es war immer eine Freude mit Dir zusammenzuarbeiten.

Bedanken möchte ich mich auch bei Prof. Dr. Clemens Prescher für die erfolgreiche Kollaboration und dafür, dass er sich bereit erklärt hat Teil meiner Prüfungskommision zu sein. I would also like to thank Prof. Dr. Hongbin Zhang for being part of my PhD committee and contribution of his expertise to this committee.

A special thanks goes to all the members of the Deringer group in Oxford. Especially, Yuxing Zhou for all the amazing lunch breaks we had together, Nijamudheen Abdulrahiman, for having a great time while exploring Oxford together, Daniel Thomas du Toit, for having endless and always enjoyable discussions, Zakariya El-Machachi, for being an amazing inspiration on how to make science more beautiful, Thomas Nicholas, for so many discussions about structure factors, and everyone else in the group for being so kind during my stay and for all the interesting discussions.

Außerdem möchte ich mich bei Dr. Christoph Otzen bedanken, der mir geholfen hat, die Welt der SiO_2 Hochdruckpolymorphe zu verstehen und natürlich für die sehr erfolgreiche Kollaboration.

Ein großes Dankeschön geht natürlich auch an alle Mitglieder der Materialmodellierung. Ganz besonders möchte ich mich bei Gabriele Rühl bedanken, die im Hintergrund immer alles perfekt organisiert. Außerdem möchte ich bei den Ex-MMs Dr. Constanze Kalcher, Dr. Daniel Utt, Lisette Haarmann und Dr. Leonie Koch bedanken, die mir in so vielen Situationen auch schon vor der Promotion helfend zur Seite standen. Besonders Team OVITO war mir eine unheimliche Stütze beim Perfektionieren meiner OVITO Skills. I would also like to thank Dr. Vasileios Karanikolas for our collaboration, it was always enjoyable to work with you! Der gleiche Dank geht natürlich auch an Dr. Delwin Perera. Ein großes Dankeschön geht an Dr. Marcel Sadowski der sowohl fachlich als auch persönlich eine große Stütze während meiner Promotion war. Immer wenn ich während meiner Promotion eine Frage hatte, war Dr. Jochen Rohrer derjenige, den ich mal kurz fragen konnte und bei dem ich eine immer kompetente Antwort bekommen habe. Vielen Dank dafür, Jochen!

Natürlich möchte ich mich auch bei meinem besten Bürokollegen, Niklas Leimeroth, bedanken. Ohne dich wären die letzten Jahre nur halb so lustig gewesen und ohne die Diskussionen mit dir wäre meine Arbeit nur halb so gut geworden! Außerdem möchte ich mich auch bei allen MM Mitgliedern für die schöne Zeit und die tollen Erlebnisse mit euch bedanken.

Danke, an meine Freunde aus dem Studium: Maximilian Kissel, Jonas Philippi, Manuel Best, Samira Kiefer, Melanie Johanning und Tim Steingräber. Euch zu haben, hat mein Studium zu einer tollen Zeit gemacht! Und natürlich an alle anderen die mich im Studium begleitet haben, ganz besonders danke an alle Fachschaftsmitglieder.

Vielen Dank, Julia Gallenberger, dass du mich immer unterstützt hast, immer für mich da warst, ohne dich hätte ich das alles nicht geschafft!

Vielen Dank an meine Familie, besonders vielen Dank an meine Eltern, für eure Unterstützung. Ohne euch wäre ich niemals so weit gekommen.

Schlussendlich möchte ich mich noch beim Bundesministerium für Bildung und Forschung (03XP0174A) und beim Deutschen Akademischen Austauschdienst (Forschungsstipendien für Doktoranden) für deren finanzielle Unterstützung bedanken. Außerdem möchte ich mich für Rechenzeit auf dem Lichtenberg Cluster (NHR4CES) und dem HoreKa (NHR@KIT) Supercomputer bedanken.

Contents

1 Introduction

Silica (SiO_2) is one of the most common compounds on Earth, making up almost two-thirds of the upper continental crust.[1] Due to its high availability and therefore also low cost, it was a natural choice for mankind to use this material in as many applications as possible. In addition to its abundance, silica has the advantage of being structurally diverse, occurring in several crystalline phases and in an amorphous form with a wide range of properties.[2] Silica in the form of quartz sand and amorphous silica is used in significant amounts in the construction industry for concrete and window glass.[3] Porous amorphous silica with low density, so-called silica aerogel, can be used for thermal insulation, due to its extremely low thermal conductivity.[4] Besides these structural applications, there are also applications in catalysis and electronics. Silica-based zeolites are porous crystallites with a high specific surface area. Often they contain additional aluminum, however, there exist also zeolites made up purely of silica.[5] Zeolites are widely used in petrochemical industry, where they are utilized for cracking of heavy petroleum distillates.[6,7] Another possible application of zeolites is for example desalination.[8] Quartz, the most common form of silica, is a piezoelectric material,[9] and is therefore used as an oscillator in quartz crystal clocks[10] and in microelectronics.[11] Also in semiconductor industry silica plays a crucial role. The most important type of transistor is the metal oxide semiconductor field effect transistor (MOSFET), which is commonly made up of a silica layer on the semiconducting silicon.[12] This is one application, where next to the pure silica also the interface to silicon is of importance.

As previously mentioned, the atomic-level structure of silica can be extremely diverse. One way to show the structural diversity and the large interest into a material is to have a look into available structure databases. The Materials Project database contains 321 different structures for the composition of SiO_2 compared to significantly fewer entries for similar compounds such as TiO_2 (44 entries), GeO_2 (9 entries), and Al_2O_3 (89 entries).[13] Figure 1.1 illustrates a structural map[14–16] of all SiO_2 structures included in the Materials Project. Each structure in the plot is represented by a point, colored according to its volume per atom. Similar structures are located close together, while different structures are further apart. On the lower right side of the plot, there are many very low density structures. Moving to the left, the silica networks become denser, reaching the other extreme on the lower left with very high-density structures. Of course, if a structure does appear in the Materials project database, it does not mean, that it can be synthesized. However, the large number of available structures indicates already the great interest in this material.

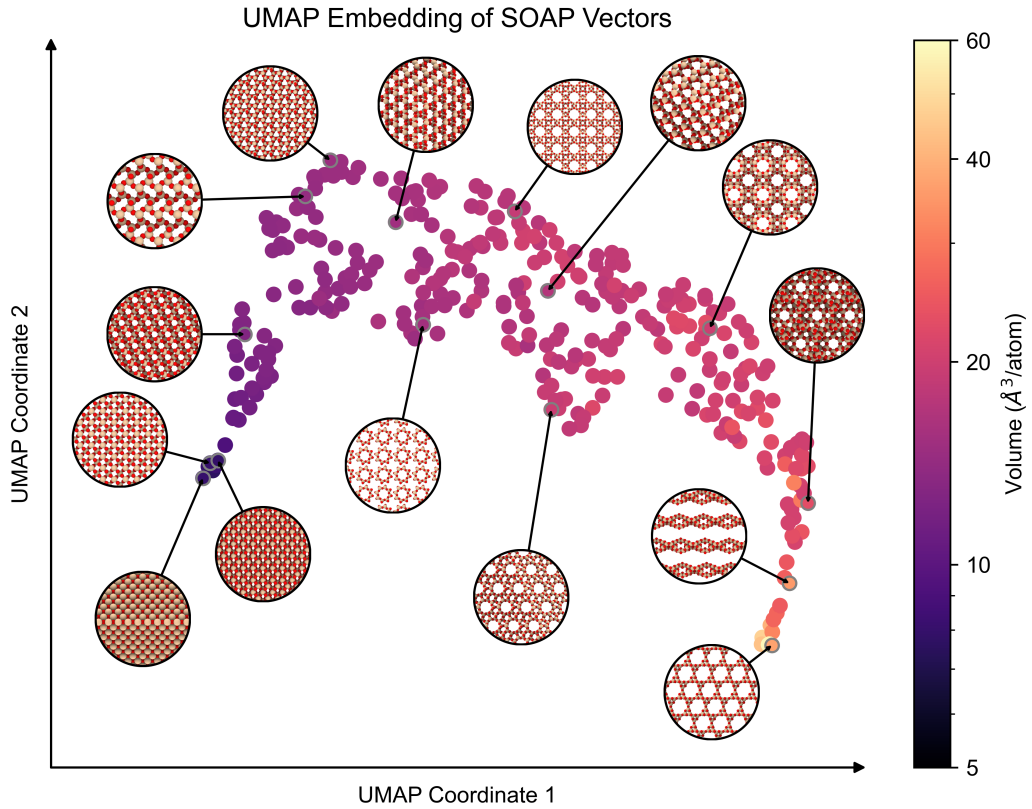

Figure 1.1: **Structural wealth of silica.** Overview of all stoichiometric SiO_2 structures included in the Materials Project database. Each data point corresponds to a structure and is color coded with the corresponding volume per atom. The coordinates of the points are based on a 2D uniform manifold approximation and projection for dimension reduction (UMAP) embedding[15] of the average smooth overlap of atomic positions (SOAP) vectors of the structures.[14] The right side contains mainly porous structures with low densities, while moving to the left the density increases.

The most important polymorph of silica is α-quartz. α-quartz is the stable structure at ambient conditions and transforms to β-quartz at a temperature of 846 K.[2] The stability range of α-quartz and β-quartz is shown in Figure 1.2. The difference between the two structures is small, as shown in Figure 1.3. Both polymorphs are built from SiO_4 tetrahedra, which in the case of β-quartz are arranged in temperature-stabilized high symmetry positions. At lower temperatures, these tetrahedra are slightly rotated, resulting in the lower symmetry structure of α-quartz.[19]

At even higher temperatures of 1140 K β-tridymite and at temperatures of 1743 K β-cristobalite becomes the stable phase (see also Figure 1.2).[2] Both structures are also based on SiO_4 tetrahedra. In the case of β-tridymite, the silicon atoms are arranged in a hexagonal diamond structure with the Si-Si bonds replaced by Si-O-Si bonds. The structure of β-cristobalite can be similarly derived from cubic diamond. However, the high-symmetry form of β-cristobalite is only a time average of the real positions of the

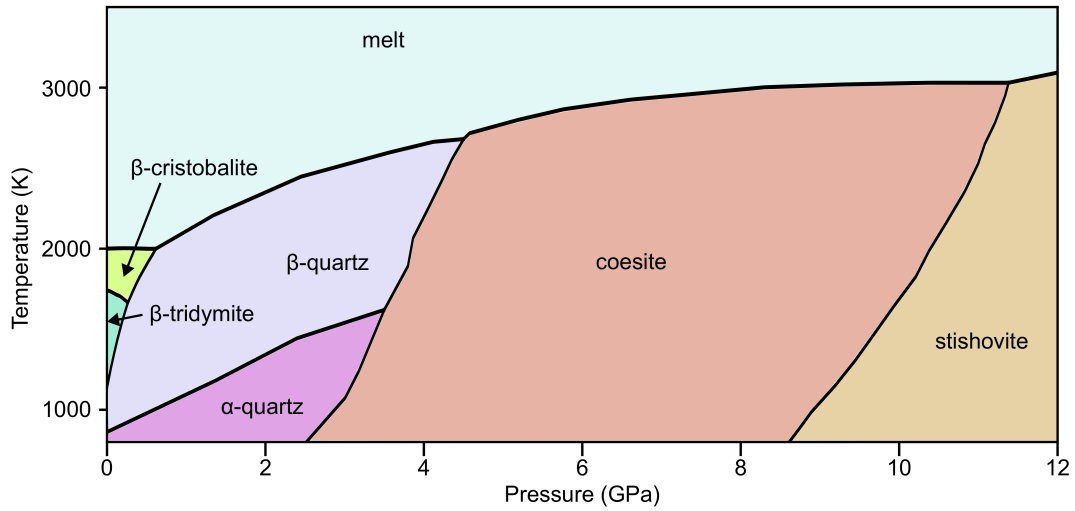

Figure 1.2: **Phase diagram of silica.** Calculated phase diagram of silica based on experimental thermodynamic data. The transition lines are taken from Swamy *et al.* [17]

oxygen atoms, which follow rotational vibrations around this ideal position.[19,20] A similar behavior was also suggested for β-tridymite.[21] At ambient pressure, β-cristobalite is the highest temperature phase of silica and melts at a temperature of 2000 K.[2] During cooling, both β-tridymite and β-cristobalite do not transform back to α-quartz, but transform into metastable low temperature structures. These phases are shown in Figure 1.3. In the case of β-cristobalite, α-cristobalite appears at temperatures below 500-550 K.[22] The structure of α-cristobalite arises from the freezing of the rotational vibrations of the connecting oxygen atoms.[19] In the case of tridymite, several crystalline phases appear during cooling. In general, the symmetry of the structure decreases with decreasing temperature. After cooling below 700-750 K, β-tridymite transforms into another hexagonal structure with slightly lower symmetry (LHP-tridymite).[18,23,24] This phase transition is accompanied by a slight displacement of the oxygen atoms (see Figure 1.3). At a temperature of about 620 K, hexagonal tridymite transforms into orthogonal OC-tridymite,[18,23] which is associated with a change in the a-b lattice parameters. This is followed by a transition around 513 K to an incommensurate OS-tridymite phase, which is not shown in Figure 1.3 due to missing data.[24] At temperatures below 423 K, the OP-tridymite phase becomes stable, another orthogonal phase with space group $P2_12_12_1$.[24] At lower temperatures, tridymite becomes monoclinic with space group Cc. This structure, called MC-tridymite, becomes stable below 370-380 K.[18,23,24] Finally, the MX-1-tridymite phase is found at temperatures below 340 K.[18,25]

Not only at high temperatures, also at high pressures there exists substantial polymorphism for silica. This can be seen in Figure 1.2 and 1.3. Both coesite and stishovite, which are two of these high-pressure polymorphs, have been synthesised[26,27] in laboratories before being found in nature, both in Meteor Crater, Arizona.[28,29] Coesite becomes more stable than quartz at a pressure of ≈3 GPa and a temperature of 1000 °C,[30] while stishovite becomes stable at pressures above ≈8.5 GPa (T=1000 °C).[31] Coesite

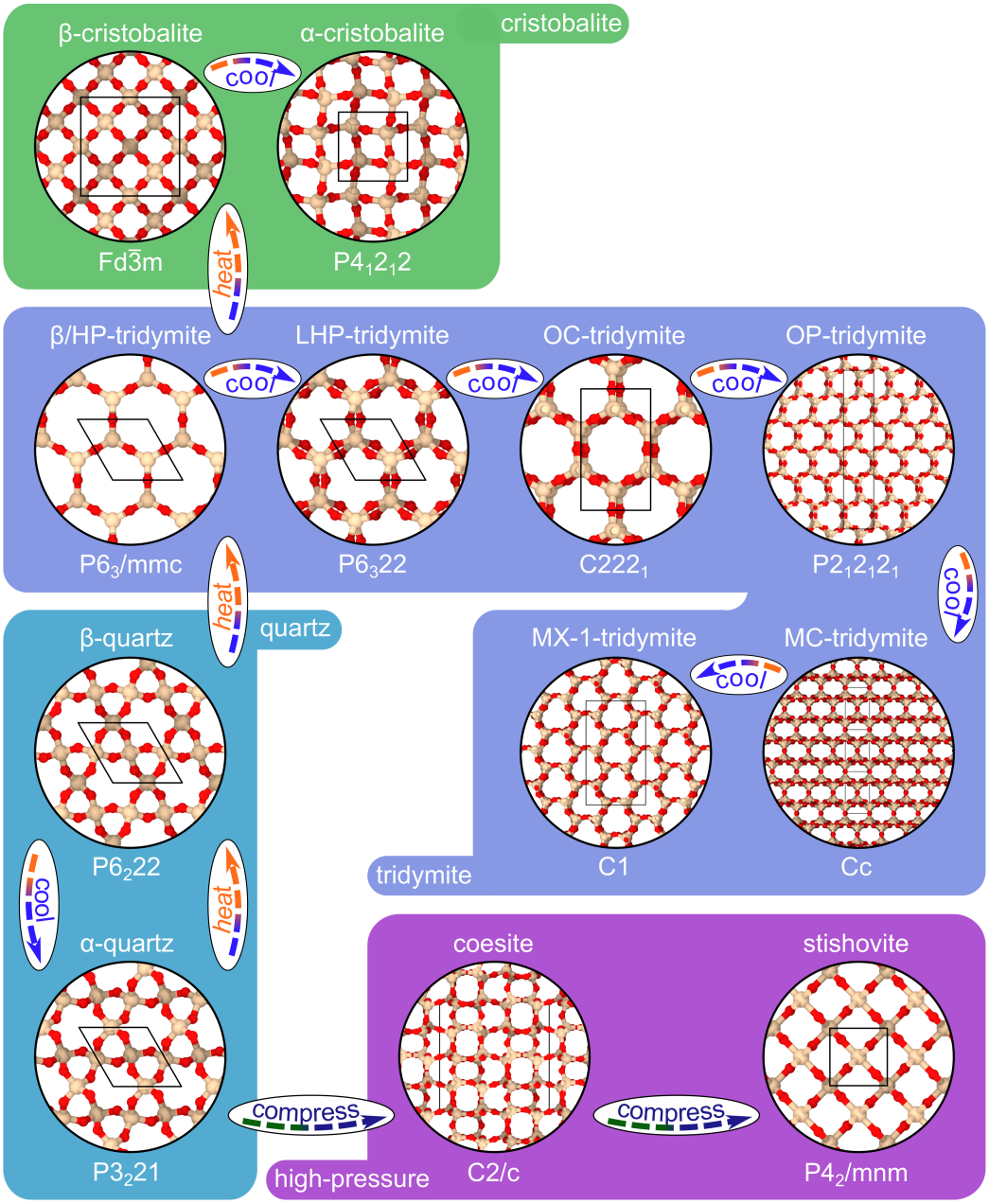

Figure 1.3: **Important polymorphs of silica.** Overview of a number of polymorphs of silica. The ground state structure at ambient conditions, α-quartz, is transforming at higher temperatures into β-quartz. At even higher temperature quartz is converting to β-tridymite, which transforms at higher temperatures to β-cristobalite. Both polymorphs do not convert to quartz during cooling, but into corresponding metastable lower temperature phases. Tridymite transforms with decreasing temperature into a number of lower temperature phases with decreasing symmetry.[18] β-cristobalite transforms to α-cristobalite. At higher pressures quartz transforms to coesite and coesite transforms to stishovite.

is still built from densely packed SiO_4 tetrahedra, while stishovite is built from SiO_6 octahedra. Silica undergoes further phase transitions at very high pressures. Stishovite transforms to $CaCl_2$-structured silica[32,33] at a pressure of 64 to 65 GPa (T=1000 °C).[34] This structure deviates only slightly from stishovite. While stishovite is tetragonal with $a = b$ lattice parameters, the $CaCl_2$ phase is orthorhombic with $a \neq b$. At even higher pressures of ≈110 GPa and the same temperature, seifertite becomes the stable phase.[35] While stishovite, $CaCl_2$-type silica and seifertite are polymorphs, in which silicon is sixfold coordinated, at pressures above 268 GPa and temperatures of 1800 K, pyrite-type silica with a coordination number of 6+2 is stable.[36] Further structural details of the high-pressure phases and also of a number of metastable high-pressure phases will be discussed in Section 1.1.

Besides the crystalline phase, silica also has an amorphous phase. While the structure of the crystalline phases is relatively easy to assess, the structure of the amorphous silica phase has long been discussed. Already in the 1930s, Zachariasen published their random network theory, according to which amorphous silica is built from randomly connected SiO_4 tetrahedra.[37] After the first experimental evidence and simple models,[38] it took more than 30 years to develop realistic structural models.[39] These models were built from SiO_4 tetrahedra made of wires and polystyrene spheres or tetrapods, and radial distribution functions could be determined by extensive interatomic distance measurements within the models.[39–41] The resulting radial distribution functions were in excellent agreement with experiment, providing even more evidence for the random network model. In later years, improved and larger models were created using reverse Monte Carlo techniques[42] and molecular dynamics simulations.[43–45] Nevertheless, there are still unknown aspects about the structure of amorphous silica. The structure factor of amorphous silica shows a distinct first sharp diffraction peak (FSDP). Its origin has been discussed extensively in the literature and is generally considered to be influenced by some medium-range order.[46,47] Various theories have been proposed for its exact origin, ranging from quasi-Bragg planes[48] to interstitial voids[47] and boundaries between cages.[49,50] However, the exact reason for the occurrence of the FSDP is still unclear. Silica glass is of high interest not only at ambient conditions, but has also been studied at elevated pressures. For example, compression experiments allowed the synthesis of the world's densest silica glass at ambient conditions.[51] Other experiments have compressed amorphous silica to pressures above 100 GPa and found that silicon with coordination numbers above six already appears at these pressures.[52,53] This is surprising in the sense that all crystalline polymorphs being stable at these pressures contain only sixfold-fold coordinated silicon. This highly coordinated silicon has often been explained by a similarity to pyrite-type silica, which contains 6+2-fold coordinated silicon.[54]

The polymorphism in silica is crucial for understanding its behavior. In the following, we will look at two problem settings in the SiO_x system, which are still not completely understood. First, we will look at the dynamic transformation behavior of quartz under high pressures. Second, we will incorporate additionally the interface to silicon and have a look at the complex structure of silicon monoxide. Based on these problems, we

will assess possible solutions using atomistic simulations with classical and machine-learning interatomic potentials.

1.1 Quartz under pressure

Quartz shows unique planar deformation features under shock[55] and can therefore be used for identifying impact events on Earth. Most notably, these features have been identified in quartz samples from Cretaceous-Tertiary boundary clays at many places in the world.[56] This gave further evidence of a giant impact event, which resulted in the distribution of huge amounts of mass in the atmosphere.[56,57] The following global winter led to a mass extinction and presumably the end of the dinosaurs.[57,58] Despite the importance of these planar deformation features, their formation mechanism is still discussed controversially.[59,60] While direct amorphization of quartz has been observed in several shock and diamond anvil cell experiments,[55,61–63] a transformation in a metastable crystalline phase with subsequent amorphisation[60,64] could also explain the formation of planar deformation features.

Indeed, several high-pressure crystalline phases have been observed in experiments or predicted by molecular dynamics simulations. For example, the quartz II structure appears at pressures of 21 GPa,[66,67] and might be identical to a $C2$ phase, which has been described in several theoretical works.[68–70] At higher pressures of 45 GPa, a $P2_1/c$ phase has been observed, experimentally.[71] This is one of several thermodynamically favorable high-pressure phases based on a HCP oxygen sublattice, which are shown in Figure 1.4.[72] While the oxygen atoms are arranged similarly in these structures, the silicon octahedra are distributed in various ways. In case of stishovite, the silicon atoms are arranged along straight lines. In seifertite, they follow a 2×2 zigzag pattern, and in the case of $P2_1/c$-type silica, a 3×2 pattern. Next to the $P2_1/c$ phase, Teter *et al.*[72] also proposed SnO_2 and $NaTiF_4$-structured silica with a 4×4 and 3×3 pattern to be thermodynamically competitive, but we have not found any experiments, which observed these phases. Additionally, besides these phases considered by Teter *et al.*, another phase also based on a HCP oxygen sublattice packing has recently been proposed by theoretical investigations[73] and later observed in several dynamic compression experiments of quartz.[60,74] In this rosiaite-structured silica, silicon atoms are arranged in graphene-like layers. Furthermore, there is a diffusionless transformation mechanism directly from quartz,[73] making it a possible intermediate state for the amorphization of quartz. There is one further structure, which we would like to discuss in detail. The most general type of structure with an oxygen HCP lattice is the defective nickel arsenide (d-NiAs) structure. In this structure, the silicon atoms are distributed with a probability of 50% in all octahedral voids (see Figure 1.4). Therefore, the oxygen sublattice is clearly ordered, while the silicon sublattice does not have any long-range order. This structure was first observed already in 1978 in diamond anvil cell experiments of amorphous silica under additional laser heating.[75] In later years, the phase was observed several other times, starting from amorphous as well as quartz samples.[64,76,77] Most remarkably, Tracy *et al.*[78] were able to observe the d-NiAs phase in *in situ* X-ray diffraction (XRD)

measurements of quartz under shock, making it another possible intermediate phase for the amorphization of quartz. Interestingly, this result deviates from very similar shock experiments by the same group for vitreous silica. There the formation of stishovite was observed. Finally, several other phases have been observed in compression experiments and simulations of quartz. Tse *et al.* [79] observed in molecular dynamics (MD) simulations of quartz using the van Beest, Kramer, van Santen (BKS)[80] potential amorphization and subsequent recrystallization at about 80 GPa within a monoclinic structure with the $I2/a$ space group, structurally related to seifertite. *Ab initio* modelling and experimental results of hydrostatically compressed quartz by Hu *et al.* [81] show the transformation to a $P2/c$ phase of silica under hydrostatic compression conditions around 25 GPa. This phase contains only sixfold-coordinated silicon. A phase containing fivefold-coordinated silicon with the space group $P3_221$ was found by Badro *et al.* [82] using non-hydrostatic MD simulations with the BKS potential. Another phase containing fivefold-coordinated silicon and sixfold-coordinated silicon has been found by *ab initio* studies of quartz hydrostatically compressed to pressures of 30-40 GPa.[83]

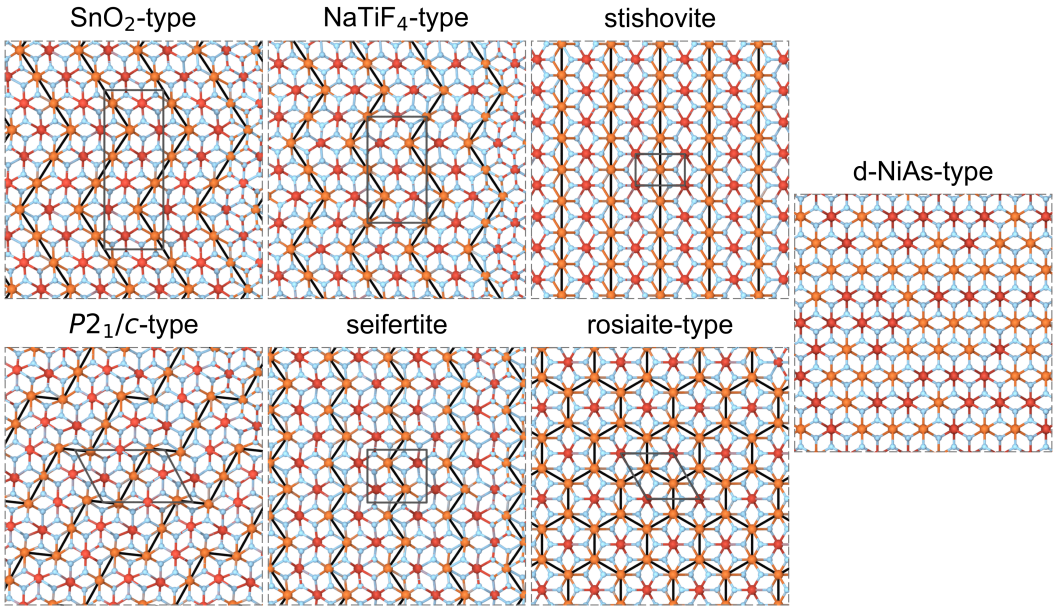

Figure 1.4: **High-pressure polymorphs of silica.** Various high-pressure structures of silica, which are all based on a hexagonal close-packed (HCP) oxygen sublattice. The blue atoms indicate oxygen atoms, whilst the red and orange atoms correspond to silicon atoms in different layers. The gray lines indicate the unit cells of the structures. The structural differences are caused by a different ordering of the silicon atoms. In stishovite, the silicon atoms are aligned along lines. In the case of SnO_2-, $NaTiF_4$- and $P2_1/c$-type silica and seifertite the silicon is arranged in different zigzag patterns. In rosiaite-structured silica the silicon atoms are arranged in graphene-like layers. Finally, in the case of d-NiAs-type silica, the silicon atoms are randomly distributed over the octahedral voids with an occupation probability of 0.5. The figure is adapted from Ref. 65.

As presented in the previous part, the understanding of high pressure silica and its phase transformations is still incomplete.

1.2 Silicon monoxide

Besides SiO_2, there also exists another oxide of silicon: silicon monoxide (SiO). SiO has a stable gas phase at high temperatures, which is well characterized.[84] However, the structure of this amorphous solid phase has been a mystery for a long time, despite its use in many applications such as a dielectric in capacitors,[85] radiative cooling coatings,[86] and protective layers on mirrors.[87] Recently, it has also attracted considerable attention as a possible anode material for lithium-ion batteries.[88–90] After its first synthesis in the 19th century,[91] various structural models have been discussed. These are illustrated in Figure 1.5. The first model, commonly called the random mixture model, assumes that solid silicon monoxide does not exist. Instead, it decomposes into a mixture of silicon and silica.[92,93] In contrast, the second model, called the random bonding model, assumes that silicon is four-fold coordinated and randomly bonded to other silicon and oxygen atoms.[94] Therefore, it would result in a homogenous amorphous material built from SiO_4, SiO_3Si_1, SiO_2Si_2, SiO_1Si_3 and $SiSi_4$ tetrahedra. Already in 1907 there has been evidence for the random bonding model by heat of combustion measurements.[95] Further studies performed X-ray and electron diffraction experiments to determine the radial distribution function. However, these experiments provide evidence for both the random mixture model[92,96,97] and the random bonding model.[98,99]

Later on, it has been found that the truth is somewhere in between. By complementing X-ray and electron diffraction with neutron diffraction, high-resolution transmission electron microscopy, Si K-edge energy-loss near-edge structure data, X-ray photoelectron spectroscopy and magnetic resonance measurements, it was found that silicon monoxide

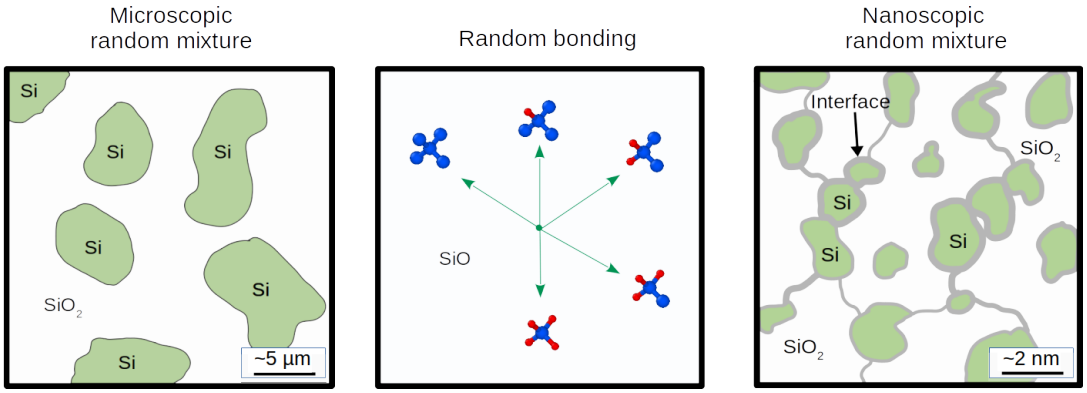

Figure 1.5: **Structural models of silicon monoxide.** The random mixture structural model of silicon monoxide assumes that it is based on a mixture of silicon and silica. In contrast, in the random bonding model, the structure is homogenous and built from SiO_xSi_{4-x} tetrahedra. The nanoscopic random mixture is also a model based on the decomposition of silicon and silica, however, with nanoscopic grains and a significant interface proportion.

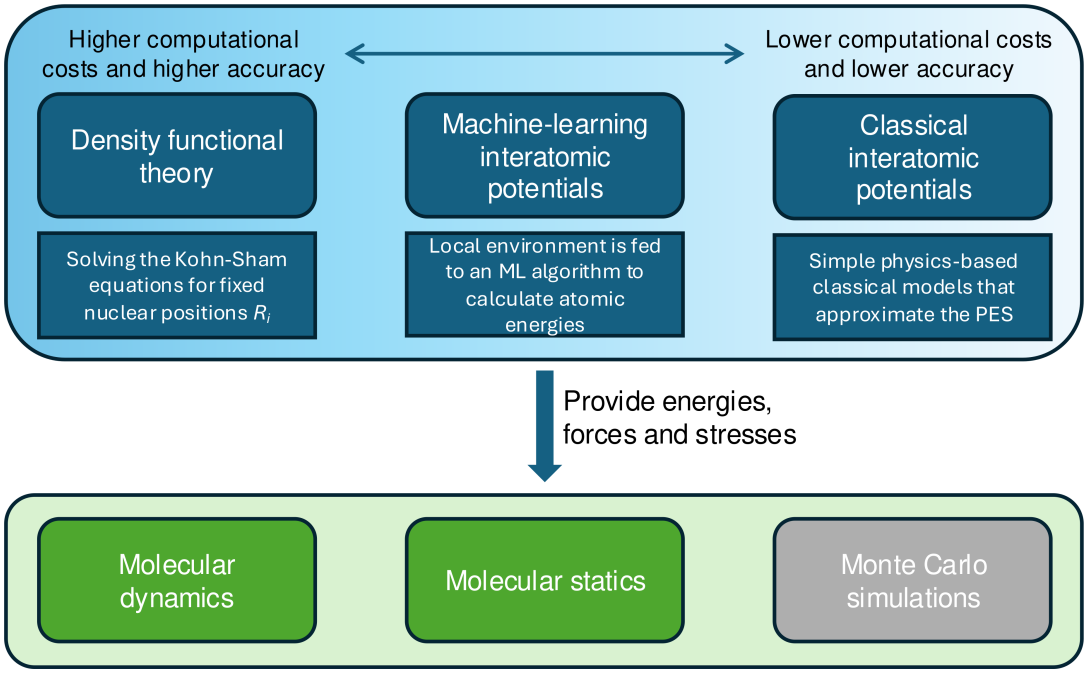

Figure 1.6: **Overview of computational methods.** The upper panel shows a number of methods to calculate energies, forces and stresses of a system. These methods have different accuracies and computational costs. The output of these methods can be used in molecular dynamics, molecular statics or Monte Carlo simulations, but we used only the first two in this work.

is indeed a mixture of silicon and silica.[100–102] However, the silicon grains have sizes of only 3-4 nm, inducing an extremely large interface proportion of 20 to 25%,[101] in which silicon is arranged similarly to the case of the random bonding model. Due to the complex structure, computational studies of the interface at the atomistic level have been scarce. Hirata *et al.*[102] generated, in their extensive and predominantly experimental study, small structural models for heterogeneous silicon monoxide with far less than 1000 atoms using classical potentials and reverse Monte Carlo techniques. Other studies have primarily focussed on the lithiation behavior of silicon monoxide.[103–105] However, these studies are *ab initio*-based and therefore have an upper limit in system size and consequently do not allow for an adequate description of the heterogeneity and interfacial structure of silicon monoxide.

1.3 Atomistic modelling of Si-O compounds

Investigating, understanding and modelling of silicon monoxide and pure silica requires accurate descriptions of the atomic interactions between silicon and oxygen. An overview of the various methods for calculating these interactions and the methods that use these interaction models is shown in Figure 1.6. Density functional theory (DFT) promises the

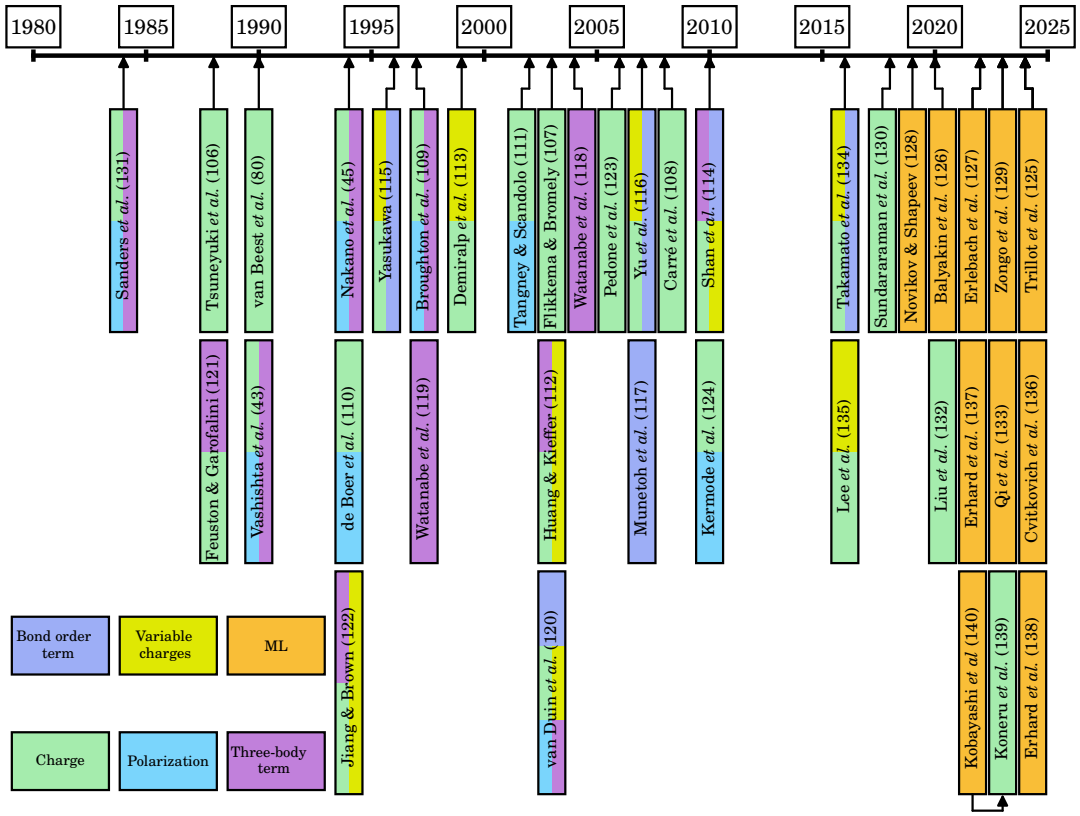

Figure 1.7: **Timeline of potentials for the SiO_x system.** The potentials shown are colored according to which physical contributions are included in the potential energy term. These include bond order terms, charge terms, terms which allow the fluctuation of the charges, polarization terms and three-body terms. In some cases like for the ReaxFF by van Duin *et al.* [120] or the potential by Lee *et al.* [135] other terms are included, which are not covered by this classification. We do not claim this list to be exhaustive.

highest accuracy, but is usually limited to systems with few thousand electrons. Details of this method are given in Section 2.9. In contrast, classical interatomic potentials (CIP) are much faster to compute, allowing system sizes of millions of atoms and simulation times of nanoseconds and above.[141] An overview of CIPs for silica is given in this section. Moreover, details of all CIPs used in this work can be found in Subsection 2.8.1. An intermediate method between DFT and CIPs are machine learning interatomic potentials (MLIP), which are trained on DFT data and promise the accuracy of DFT while being much more cost-efficient. Although MLIPs are generally more expensive than CIPs, they allow simulation times of nanoseconds and system sizes of millions of atoms. In this section, we give a brief overview of the concepts of MLIPs and their application to silica. A more detailed description can be found in Subsection 2.8.2.

The energies and forces from the above-mentioned methods can be used for MD, molecular statics (MS), and Monte Carlo simulations. MD simulations are used to study the time evolution of a system at finite temperature by integrating the equations of motion. Details are given in Section 2.1. MS calculations are used to find the energetic minimum of a structure by changing the positions of atoms and/or the lattice parameters. These calculations are performed at zero K. Finally, there are Monte Carlo simulations, which use random operations such as moving and swapping atoms to sample the configuration space.[142]

Over the last 40 years a large number of interatomic potentials have been developed for the SiO_x system (see Figure 1.7). A detailed overview of all CIPs used in this work can be found in Subsection 2.8.1. In the following, we will give an overview of different directions in the development of SiO_x potentials. In general, they share the following approach to calculate the total energy of the system,

$$E_{tot} = \sum_i V_i, \tag{1.1}$$

where the total energy of the system is divided into individual atomic contributions. Apart from MLIPs, where usually no explicit short-range term is included, the atomic energies are calculated by the following approach,

$$V_i = \frac{1}{2} \sum_{j,j\neq i} V_{ij}^{SR}(r_{ij}) + \text{Additional terms}, \tag{1.2}$$

where $V_{ij}^{SR}(r_{ij})$, is a short range potential such as the Morse or Buckingham term describing the general attraction and repulsion of the atoms, which depends only on the interatomic distance r_{ij}. In the case of silica, a very commonly used additional term is the Coulomb term given by,[80,106–108,123,132,143]

$$V_i^{\text{Coulomb}} = \frac{1}{2} \sum_{j,j\neq i} \frac{q_i q_j}{4\pi\epsilon_0 r_{ij}}, \tag{1.3}$$

where q_i and q_j are the charges of the corresponding atoms and ϵ_0 is the vacuum permittivity. Two of the most commonly used silica potentials include only these two terms: The BKS potential[80] and the Tsuneyuki, Tsukada, Aoki and Matsui (TTAM) potential.[106] Although these forms are extremely simple, they are still widely used in MD simulations.[144] Moreover, they have been reparameterized several times e.g. for silica nanoclusters[107] and amorphous silica.[108] All potentials shown in Figure 1.7 that contain such a charge term are colored accordingly. To further improve the description of the system, additional physically motivated terms have been included in other models. One example is the inclusion of variable charges, e.g. by charge equilibration[113–116,120,134,135,145] or simpler charge transfer functions.[112,122] This also has the advantage that the potentials are able to describe silica, silicon and their mixtures simultaneously. In contrast, fixed charge models have to be used in stoichiometric mixtures to fulfill charge neutrality. Other approaches to include more physics are for example three-body terms,[43,45,109,118–121,131,146] bond order terms[114–117,134] or polarization terms

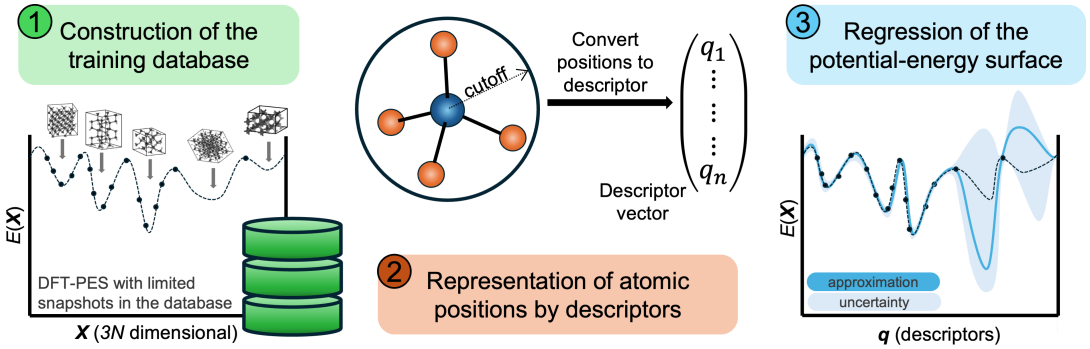

Figure 1.8: **General concept of MLIPs.** A machine-learning potential is based on a database built from *ab initio* data. The Cartesian positions are converted into a descriptor vector. This descriptor vector is used as input for a regression machine-learning algorithm. Inspired from Ref. 154.

in various forms.[43,45,111,120,124,131,147] There are also few potentials that do not contain any charges, but only short range terms. This is the case for the Watanabe *et al.*[118,119] and Munetoh *et al.*[117] potentials.

Many of the above-mentioned CIPs have been developed to describe certain structural phases. Therefore, they perform very well for these parts of configurational space but fail in other cases. For example, the BKS potential fails to describe the phase diagram of SiO_2, by predicting stishovite to be more stable than α-quartz at zero pressure.[148] In contrast, the more complex Tangney-Scandolo model[111] is performing worse than the BKS for the equation of state of stishovite.[149] However, a good description of the high-pressure phases, such as stishovite, is essential for accurate analysis of phase transition under pressure. Additionally, all fixed-charged models are restricted to stoichiometric SiO_2 and are unable to describe general SiO_x systems. This is due to the requirement of charge neutral simulation cells. Only interatomic potentials that include no charges at all or flexible charges can be used for any mixture of SiO_x. The Munetoh potential, which is in principle capable of simulating these systems, performs not very well for pure crystalline silica, because it is unable to accurately describe the phase transformations of quartz and the equation of state of stishovite.[150] A flexible charge potential, namely the Charge-Optimized Many-Body potential for Si-O[114] is also able to describe mixed systems. However, also this advanced and computationally expensive potential is not able to describe the α-β-quartz transition accurately.[151] Similarly, the complex ReaxFF model for silica[120] does not work well for high-pressure silica.[151] Moreover, many of the CIPs shown in Figure 1.7 are not implemented within established MD codes, like `LAMMPS`[152] and `GROMACS`,[153] and can therefore not easily be used by researchers.

Figure 1.7 already indicates that the development of interatomic potentials has moved away from physically based models in recent years. MLIPs were introduced by Behler and Parinello in 2007[155] and have become widely used since then. These potentials allow a higher transferability to a wide range of configurational space. If trained with complete and consistent training data, they allow achieving higher accuracies in these parts of configurational space. The general concept of MLIPs is depicted

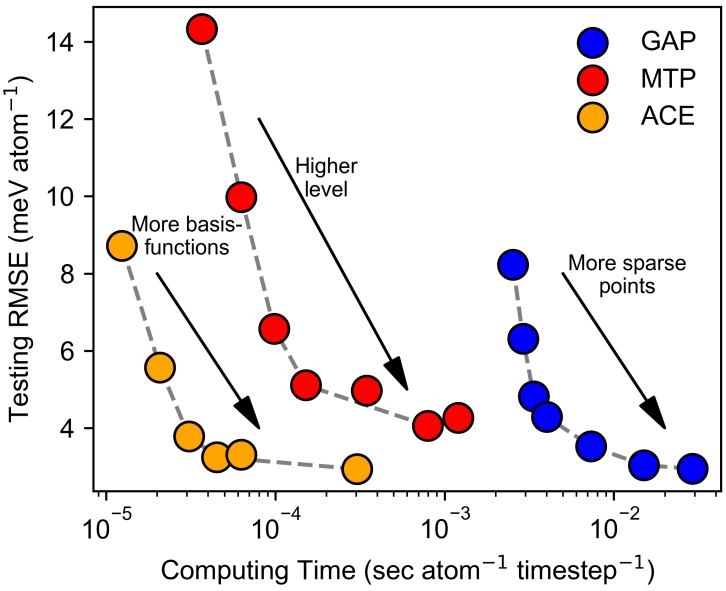

Figure 1.9: **Performance–cost trade-off of various MLIP approaches.** Exemplary accuracy versus computing time plot of the ACE,[156] MTP,[157] and GAP.[158] The tests have been performed for a pure silica database.

in Figure 1.8 and a more detailed overview is given in Subsection 2.8.2. MLIPs are generally based on their training database, which is usually built from DFT data. They can only learn the physical interactions from this database, therefore a comprehensive training database is very important for a general MLIP.[154] The Cartesian coordinates from the database cannot be used directly as input for the machine-learning algorithm. This is because the input to the machine learning (ML) algorithm has to be rotationally, translationally and permutationally invariant. Moreover, a fixed number of input numbers is usually required. Therefore, the environment of atoms is converted into descriptor vectors, which are then fed into the ML algorithm.[154] An advantage of many MLIPs over CIPs is that they often provide some method of uncertainty quantification. This allows to assess whether the potential can be used reliably in a certain range of configurational space and can also be used to extend the database by active learning (see Subsection 2.8.2).

The choice of descriptor vector and ML-method strongly influences the final accuracy and performance of the potential. This is illustrated in Figure 1.9 for three different approaches (atomic cluster expansion (ACE),[156] moment tensor potentials (MTP)[157] and Gaussian approximation potential (GAP)[158]) that combine different descriptors and ML methods. While all approaches achieve similar accuracy, they have computational time differences of several orders of magnitude. A detailed review of general MLIP approaches can be found in Subsection 2.8.2, where we also present several MLIP classes used in this work in detail.

In the recent years, several MLIPs have been developed for silica. In 2019, Novikov and Shapeev developed an MTP[157] for α-quartz.[128] The dataset contained only α-quartz structures that were rattled, deformed, and in some cases contained vacancies. The main goal of their study was not to develop a comprehensive potential for silica. Instead, they compared two fitting approaches. First, they fitted a pure MTP, and second, they combined a MTP with a charge equilibration term.[145] They found that increasing the number of parameters increased the accuracy of the MTP, but adding the charge equilibration term did not. However, since the database contained only α-quartz, this assumption may not hold for a more complex database covering the full complexity of the silica system.

Later, in 2020, Balyakin *et al.*[126] published a neural network potential (NNP) for liquid silica trained with the `DeePMD` package.[159] The database was generated using *ab initio* MD data from different MD procedures. The resulting potential was validated by comparing the radial and bond angle distribution functions, the velocity autocorrelation function, and the vibrational density of states with *ab initio* results. However, no crystalline data was included in the training, and although the potential works well for glassy states, training data for these structures are missing.

In 2022, shortly after the publication of our GAP potential for silica,[137] Erlebach *et al.*[127] published a comprehensive machine-learning interatomic potential based on the SchNet architecture.[160] The main purpose of this potential was to identify energetically competitive hypothetical zeolite structures. Although zeolites were their primary focus, the database also included denser silica polymorphs, surface models, and amorphous silica. They iteratively refined their database through active learning to allow for the potential to describe melting processes and amorphization of zeolites. Another important difference between this study and others is that they used strongly constrained and appropriately normed (SCAN) exchange-correlation data as training data rather than computational less demanding generalized gradient approximation (GGA) data. The potential was tested on a number of properties, e.g. energetic stability of zeolites and vibrational properties of amorphous silica and α-cristobalite, showing good agreement with experiment and the *ab initio* reference. Moreover, the potential was used to calculate defect formation energies and to simulate the amorphization behavior of compressed zeolites. Finally, the potential was used to re-optimize an existing zeolite database to find energetically competitive silica polymorphs.

While previous studies focused on ambient pressure phases, Qi *et al.*[133] and Kobayashi *et al.*[140] were interested in the properties of densified glasses up to pressures around 10 GPa. Both studies fitted machine-learning interatomic potentials, the first using the `DeePMD` package, the second using the `n2p2` code.[161,162] Both papers trained their potentials on data from *ab initio* MD simulations. Moreover, both have investigated the density as a function of pressure. However, while Qi *et al.* focused on the vibrational properties, Kobayashi *et al.* investigated structural features such as the structure factor and ring distributions.

More recently, another MLIP has been published with a focus on the amorphous and liquid phases.[125] Their training data was also generated from *ab initio* MD simulations. They also added additional data for highly compressed amorphous cells to allow the

potential to learn the repulsion between atoms correctly. They used the `n2p2` code for fitting.[161,162] They systematically investigated vibrational properties such as vibrational density of states and structural properties like ring statistics, radial distribution functions and structure factors. In particular, they compressed silica glass up to pressures of 14 GPa. Notably, they also tested the transferability of the potential to crystalline polymorphs of silica. Although the training database did not contain explicit data for these structures, the potential still achieved reasonable results.

While the MLIPs mentioned so far have focused on stoichiometric silica, two recent preprints have worked on more general systems.[129,136] Zongo *et al.*[129] fitted a MTP for silica, silicon and oxygen. They included data for vacancies, interstitials, stacking faults, deformed crystals, amorphous and liquid structures and also included oxygen molecules in the training data. Finally, they applied the potential to a number of benchmark cases, structural properties of amorphous silicon and amorphous silica, vacancy diffusion paths in silicon, and heat capacity calculations. However, although the potential seems to work well for cases of pure SiO_2, Si, or O, the authors do not show whether other off-stoichiometric mixtures can also be described. Since off-stoichiometric mixtures are not included in the database, interfaces between silicon and silica may not be well described. In contrast, Cvitkovich *et al.*[136] followed a different approach, fitting a GAP to model the oxidation of silicon. Their training database includes Si dimers, O dimers, but also bulk phases of silicon and silica and oxidized surfaces of silicon. Using their potential, they are able to simulate the oxidation process of silicon in simulations with nearly 1 ns simulation time.

1.4 Research questions

Based on this literature review of the Si-O system as well as the available methods, we want to raise the following research questions:

How can we construct a training database for the Si-O system? Several options exist for the construction of training databases. These include for example manual construction of input data and active learning. An additional challenge in the system is the inclusion of Si-SiO_2 interfaces and the wide range of the configurational space, which is of interest for potential users.

Is it possible to train a machine-learning interatomic potential capable of describing the full Si-O system? Incorporating the wide range of silica polymorphs, silicon and interfaces between both, might be a challenge for the transferability of MLIPs. It is not clear, whether these potentials are flexible enough to describe all parts of configurational space with the same accuracy.

Can the thermodynamic behavior of silica be sufficiently described by such a potential? For thermodynamic descriptions of the system highly accurate energies and forces are necessary. Moreover, also the underlying DFT data needs to be in very close agreement with experiment. The high-pressure as well as the high-temperature phase diagram is extremely complex, and it might be that its reproduction is not possible.

How does the structure of silicon monoxide look like on the atomic scale? Atomic structure models of silicon monoxide are not available in literature. Even if an interatomic potential is available for the system, it might not be clear what is a good simulation protocol to generate silicon monoxide structures.

How does quartz and amorphous silica transform under shock, and why have different phases been observed in experiment? In shock and compression experiments of quartz and amorphous silica, various phase transformations have been observed. However, it is still unclear under which conditions, which phases might appear. A machine-learning interatomic potential could give new insights into these phase transitions and provide therefore a better understanding of the different experimental conditions.

Methods 2

In this chapter, we will give a brief overview of the methods used in this work. We will start with the basics of molecular dynamics (MD) and possible applications to shock simulations. Then, we will introduce possible ways to calculate free energies from the finite displacement method and thermodynamic integration. This is followed by an introduction of the solid-state nudge elastic band (SS-NEB) method, and possible structural analysis methods for MD simulations. Finally, we are ending with methods to calculate energies and forces in atomistic simulations, in particular, classical interatomic potentials (CIP), machine learning interatomic potentials (MLIP) and density functional theory (DFT). Generally, detailed information about DFT calculations and MD simulations can be found in several textbooks.[141,142,163,164]

2.1 Molecular dynamics

MD simulations are widely used in this work. They are useful for analyzing phase transitions (see Chapter 5 and 6) and to generate structural models of amorphous materials (see Chapter 4 and 6). In MD simulations, atoms are treated as mathematical mass points obeying the classical equations of motions. These equations of motions are given in a NVE ensemble by,[141]

$$m_i \ddot{\vec{r}}_i = \vec{f}_i, \qquad \text{for} \qquad i = 1,...,N, \tag{2.1}$$

where m_i is the mass of atom i, N is the number of atoms, f_i is the force acting on atom i, while $\ddot{\vec{r}}_i$ is the second derivative of the position or the acceleration of that atom. Since this equation can only be solved for two particle systems analytically, numerical integration is necessary in practice. For a practical meaning of the equation accurate forces are necessary. In principle these forces can be obtained from DFT calculations (see Section 2.9), however, these calculations are extremely expensive. A more efficient way to calculate forces are classical interatomic potentials, which scale with $\mathcal{O}(N)$ in case of short-range potentials and will be described for silica in detail in Subsection 2.8.1. However, as mentioned in Section 1.3 these often lack the required accuracy. A more accurate way promising DFT accuracy with $\mathcal{O}(N)$ scaling are MLIPs, which we will describe in detail in Subsection 2.8.2.

In cases of other ensembles like the NVT or NPT ensemble, Equation 2.1 is modified, and additional terms are added to modify the temperature and change the box size to

achieve appropriated pressures. This is done using frictional terms. In the Nosé-Hoover thermostat method [165,166] the equations of motion are given by,[141]

$$m_i \ddot{\vec{r}}_i = \vec{f}_i - \gamma m_i \dot{\vec{r}}_i, \qquad \text{for} \qquad i = 1,...,N, \tag{2.2}$$

with [141]

$$\dot{\gamma} = \frac{1}{\tilde{M}}\left(T - T_{\text{target}}\right), \qquad \text{where} \qquad \tilde{M} = \frac{3k_B}{N}M, \tag{2.3}$$

where γ can be interpreted as friction constant, which is accelerating and decelerating particles systematically to heat and cool the system from the current temperature T to the target temperature T_{target}. M is in this case the mass of a fictitious particle added to the system and k_B is the Boltzmann constant.

An example for equations of motion, which also consider the change of the box size can be found in Section 2.3. `LAMMPS` uses equations of motion from Ref. 167 and corresponding integration schemes from Ref. 168. Due to their complexity it would be beyond the scope of this work to examine them in detail. In our `LAMMPS` simulations we used a numeric time integration step of 1 fs, a temperature damping constant of 0.1 ps for NVT and NPT simulations and a pressure damping constant of 1 ps for NPT simulations.

2.2 Melt-quench simulations

Melt-quench simulations are commonly used in this thesis. In general, the idea of melt-quench simulations is to anneal a solid enough that it melts, and a liquid is obtained within the MD simulation. This liquid is then cooled to room temperature to generate an amorphous structure model. The general protocol used in this thesis unless otherwise noted, is as follows:

- NVT simulation for 10 ps at 6000 K (Randomization)
- NPT simulation for 100 ps at 4000 K and 0 GPa (Equilibration of the liquid)
- Cooling from 4000 K to 300 K at constant pressure of 0 GPa with a given quench rate (Quench to room temperature)
- NPT simulation for 10 ps at 300 K and 0 GPa (Equilibration at room temperature)

2.3 Shock simulations

Shock simulations give insights into the behavior of materials under extreme conditions. We use shock simulations in Chapter 5 to find additional details of the phase transformation behavior of amorphous silica and quartz under extreme pressure. In this work, we use the constant-stress Hugoniostat method to perform shock simulations.[169] The basis of this method are the Hugoniot relations, which describe the conservation of mass,

momentum and energy under shock. In the one dimensional case of shock along the z-direction, these are given by[169]

$$\text{mass conservation,} \qquad \rho_0 u_s = \rho(u_s - u_p), \tag{2.4a}$$

$$\text{momentum conservation,} \qquad P_{zz} = P_0 + \rho_0 u_s u_p, \tag{2.4b}$$

$$\text{energy conservation,} \qquad E_H = E_0 + 0.5(P_{zz} + P_0)(V_0 - V). \tag{2.4c}$$

Here, $\rho = 1/V$ is the density of the shocked state, u_s is the velocity of the shock wave, u_p is the velocity of the particles, P is the shock pressure, E is the specific internal energy and V is the specific volume of the shocked state. Correspondingly, P_0, ρ_0, E_0 and V_0 are the same properties, but in the unshocked state.[169] These Hugoniot equations can be easily derived according to Figure 2.1. The first equation of mass conservation is based on the assumption that the mass at the time t_0 and t_1 needs to be equal, which results in the equation,[170]

$$\rho l_s(t_0)A + \rho_0 l_u(t_0)A = \rho l_s(t_1)A + \rho_0 l_u(t_1)A, \tag{2.5}$$

where A is the cross-section of the material and l_s and l_u are the lengths of the shocked and the unshocked state. This equation can be easily transformed to Equation 2.4a. In case of momentum conservation different pressures in the shocked and unshocked state induce a force on the material. This results in the following momentum conservation equation,[170]

$$\rho l_s(t_1)u_p A - \rho l_s(t)u_p A = (P - P_0)A \cdot (t_1 - t_0). \tag{2.6}$$

Similarly, this equation can be transformed to Equation 2.4b while making use of Equation 2.4a. Finally, energy conservation can be expressed by considering the internal and the kinetic energy and the work applied to the material,[170]

$$E_{\text{tot}}(t_0) = \rho_0 l_u(t_0)E_0 A + \rho l_s(t_0)EA + 0.5\rho l_s(t_0)u_p^2 A \tag{2.7a}$$

$$E_{\text{tot}}(t_1) = \rho_0 l_u(t_1)E_0 A + \rho l_s(t_1)EA + 0.5\rho l_s(t_1)u_p^2 A \tag{2.7b}$$

$$E_{\text{tot}}(t_1) - E_{\text{tot}}(t_0) = PAu_p(t_1 - t_0), \tag{2.7c}$$

where $E_{tot}(t)$ is the total energy of the material at time t. As before, based on these equations and taking into account Equation 2.4a and 2.4b, 2.4c can be derived. More details about the derivation can be found in Ref. 170. More information about shocks can be found also in a number of textbooks, for example in Ref. 171.

Ravelo *et al.*[169] introduced equations of motions that constrain the system to fulfill the energy condition (see Equation 2.4c) of the Hugoniot relations. For this they are using modified isobaric-isothermal equations of motions by Melchionna *et al.*,[172] which are based on those by Hoover.[173] Based on earlier works,[174] they introduce two additional variables, the heat flow variable ζ and the strain rate variable η_α.[169] Here, and in the following α indicates the vector component. The equations of motion read as follows,[169]

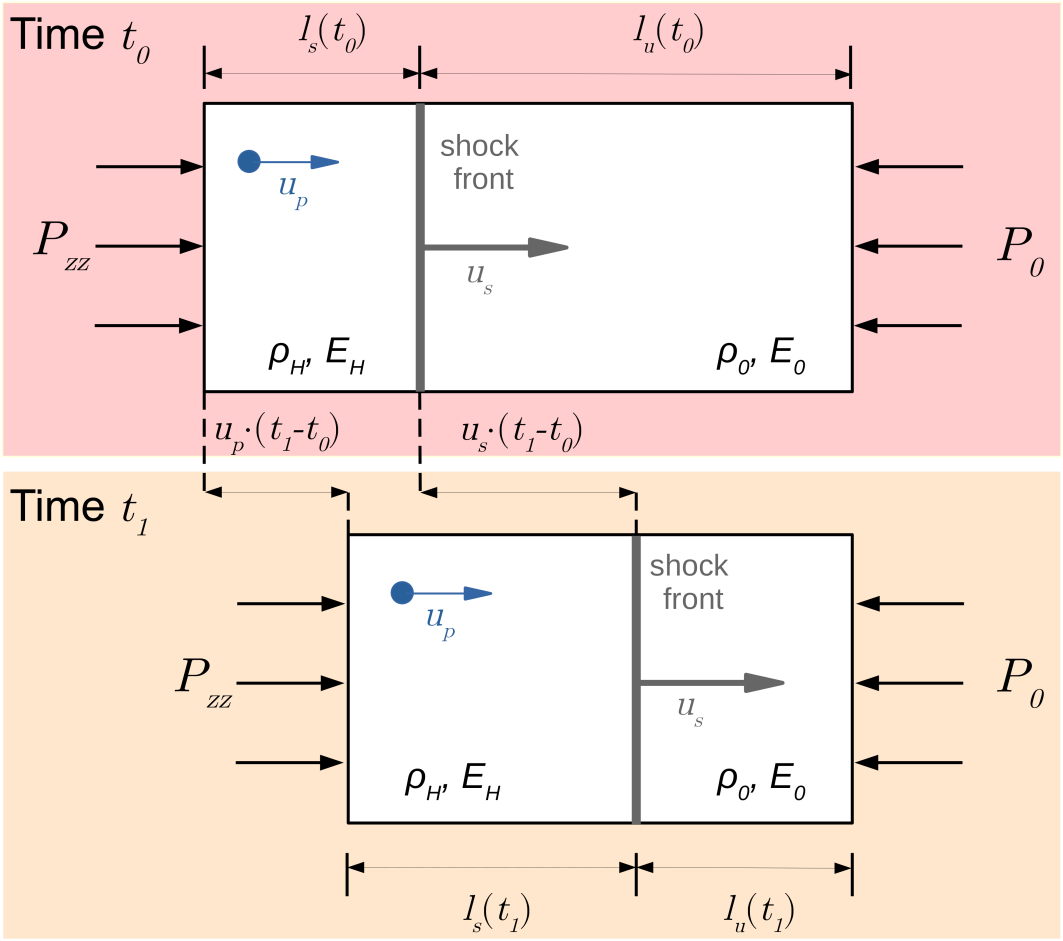

Figure 2.1: **Shock process within a material.** A material block under shock at two different times t_0 and t_1. P is the shock pressure, while P_0 is the pressure of the unshocked part of the material. l_s is the length of the shocked part and l_u is the length of the unshocked part. Both parameters are time-dependent due to the propagation of the shock. u_s is the velocity of the shock wave and u_p is the velocity of the particles in the shocked part of the material. ρ, ρ_0 and E and E_0 are the specific volumes and internal energies in the shocked and unshocked part of the material. The illustration is based on Fig. A1.1 from Ref. 170.

$$\dot{r}_{\alpha i} = \frac{p_{\alpha i}}{m_i} + \nu_p \eta_\alpha r_{\alpha i}, \tag{2.8a}$$

$$\dot{p}_{\alpha i} = F_{\alpha i} - (\nu_p \eta_\alpha + \nu_H \zeta) p_{\alpha i}, \tag{2.8b}$$

$$\dot{L}_\alpha = \nu_p \eta_\alpha L_\alpha, \tag{2.8c}$$

$$\dot{\zeta} = \frac{\nu_H}{B_0 V_0}[E - E_H(t)] - \beta_H \zeta, \tag{2.8d}$$

$$\dot{\eta}_\alpha = \frac{\nu_p}{B_0}[\sigma_{\alpha\alpha} - P_{\alpha\alpha}] - \beta_p \eta_\alpha. \tag{2.8e}$$

As in Section 2.1, $r_{\alpha i}$ gives the coordinate, $p_{\alpha i}$ is the momentum and $F_{\alpha i}$ is the force acting on atom i. ν_p and ν_H are coupling parameters and β_H and β_p are damping parameters. L_α is the length of the box in α direction, B_0 is the bulk modulus, V_0 is the volume in the unshocked state and $P_{\alpha\alpha}$ is the unshocked stress state. $\sigma_{\alpha\alpha}$ is the internal stress tensor during the simulation. In the one dimensional case the Hugoniot energy is given by Equation 2.4c with,[169]

$$E_H(t) = E_0 + \frac{1}{2}[\sigma_{zz}(t) + P_0][V_0 - V(t)], \tag{2.9}$$

where both the pressure $\sigma_{zz}(t)$ and the volume $V(t)$ are time-dependent.

Within LAMMPS the Hugoniostat method is implemented as `fix nphug`, which implements the algorithm within a derivation of their standard NPT class. In our simulations we specified temperature and pressure damping constants of 20 ps as in earlier shock simulations of silica.[175]

2.4 Free energy calculations

Determining the stability of certain phases under given conditions is a typical task in atomistic modelling. For these calculations there are different methods available with various advantages and shortcomings. We used the following methods, to determine several phase diagrams of silica in Chapter 4. The thermodynamic stability of a phase at a certain pressure p and temperature T is determined by its Gibbs free energy,

$$G(p,T) = U + pV - TS, \tag{2.10}$$

with the inner energy U, the volume V and the entropy S. To determine the stability of phases using an interatomic potential the Gibbs energy of a phase needs to be calculated. For simplicity often the case at 0 K is considered in which the Gibbs energy reduces to the enthalpy H,

$$H = U + pV, \tag{2.11}$$

which can be easily extracted from energy-volume curves, e.g. by a Birch-Murnaghan fit. The Birch-Murnaghan equation of state gives a relation for the inner energy U at 0 K by,[176,177]

$$U(V, T=0) = E(V) = E_0 + \frac{9V_0B_0}{16}\left[\left[\left(\frac{V_0}{V}\right)^{\frac{2}{3}} - 1\right]^3 B_0' + \left[\left(\frac{V_0}{V}\right)^{\frac{2}{3}} - 1\right]^2 \left[6 - 4\left(\frac{V_0}{V}\right)^{\frac{2}{3}}\right]\right], \tag{2.12}$$

where E is the potential energy. Additionally, a relation between the pressure as function of the volume is given by,[176,177]

$$p(V) = \frac{3B_0}{2}\left[\left(\frac{V_0}{V}\right)^{\frac{7}{3}} - \left(\frac{V_0}{V}\right)^{\frac{5}{3}}\right]\left[1 + \frac{3}{4}(B_0' - 4)\left[\left(\frac{V_0}{V}\right)^{\frac{2}{3}} - 1\right]\right], \tag{2.13}$$

with the equilibrium volume V_0, the bulk modulus B_0 and the derivative of the bulk modulus B_0'. This first energy equation is fitted to energy-volume curves, and then both equations are inserted into Equation 2.11. This gives an enthalpy H as a function of volume, which can then be rearranged to an enthalpy as a function of pressure using the pressure-volume relation from Equation 2.13. For energy-volume curve calculations, we performed hydrostatic energy minimization at multiple pressures (interatomic potentials) or at fixed volumes (DFT). This approach works well to approximate the stability of a given phase over a wide range of pressures. However, to include temperature effects it is essential to calculate the vibrational entropy. To obtain this entropy term, we have used two methods in this work, which we will assess below.

2.4.1 Finite displacement phonon calculations

The finite displacement or frozen phonon approach is used in Chapter 4 to calculate phonon dispersion curves and low temperature phase diagrams. In the harmonic approximation, the potential energy of a crystal is expanded by,[178]

$$V = \Phi_0 + \frac{1}{2} \sum_{l\kappa\alpha,l'k'\alpha'} \Phi_{l\kappa\alpha,l'k'\alpha'} u_{lka} u_{l'k'\alpha'}, \tag{2.14}$$

where $\Phi_{l\kappa\alpha,l'k'\alpha'}$ are the second-order forces constants and u_{lka} is the displacement of atom k in unit cell l in the Cartesian direction α from its equilibrium position. These forces constants can be used to define the dynamical matrix $D_{k\alpha,k'\alpha'}(\vec{q})$ at the wave vector $\vec{q}$ by,[178]

$$D_{k\alpha,k'\alpha'}(\vec{q}) = \frac{1}{N\sqrt{m_k m_{k'}}} \sum_{ll'} \Phi_{l\kappa\alpha,l'k'\alpha'} e^{i\vec{q}(R^{\vec{0}}_{l'k'} - R^{\vec{0}}_{lk})}, \tag{2.15}$$

where m_k is the atomic mass of atom k, N is a normalization factor and $R^{\vec{0}}_{lk}$ is the equilibrium position of atom k in unit cell l. This dynamical matrix is used to solve the eigenvalue problem,[178]

$$D(\vec{q}) = T(\vec{q})\Omega^2(\vec{q})T^{\dagger}(\vec{q}), \tag{2.16}$$

where $T(\vec{q})$ is a matrix containing the eigenvectors of $D(\vec{q})$ and $\Omega^2(\vec{q})$ is a diagonal matrix containing the squared phonon eigenfrequencies $\omega^2_{\vec{q}\nu}$ with band index ν. To perform a phonon calculation, first the force constant matrix is calculated, and then the dynamical matrix can be determined from it. The force constant matrix is usually determined using the supercell approach. A supercell of the crystal structure is created and in this supercell atoms are systematically displaced. The displacement of atoms induces forces, which are calculated using DFT or interatomic potentials. The following system of linear equations can be solved to determine the force constant matrix,[178]

$$-f_{lk\alpha} = \sum_{l'k'\alpha'} \Phi_{l\kappa\alpha,l'k'\alpha'} u_{l'k'\alpha'}, \tag{2.17}$$

where $f_{lk\alpha}$ is the force acting on atom k in the unit cell l in the direction α. After calculating the eigenvalues of the dynamical matrix, the phonon eigenfrequencies can be used to determine the vibrational entropy of the system. The vibrational entropy in the harmonic approximation is given by,[178]

$$S_{ha} = \frac{1}{2T}\sum_{\vec{q}v}\hbar\omega_{\vec{q}v}\coth(\hbar\omega_{\vec{q}v}/2k_BT) - k_B\sum_{\vec{q}v}\ln(2\sinh(\hbar\omega_{\vec{q}v}/2k_BT)). \tag{2.18}$$

One simple way to include at least the contribution of anharmonic lattice expansion is the quasi-harmonic approximation. In this approximation, the energy and the harmonic vibrational entropy is calculated over a range of volumes. Then, the Gibbs free-energy can be calculated by the following equation,[178]

$$G(T,p) = \min_V[E(V) - TS_{ha}(V,T) + pV], \tag{2.19}$$

where V_c is the volume of the unit cell. To minimize this function, equations of state such as the Birch-Murnaghan equation (see Equation 2.12 and 2.13) are fitted to multiple points from harmonic calculations. These fits allow the equilibrium volume and energy to be calculated at different temperatures and pressures. In addition, the stability of different phases at given pressures and temperatures can be determined. This allows the prediction of temperature-pressure phase diagrams. All these calculations are implemented in the `phonopy` code[178,179] used in this work. However, although the quasi-harmonic approximation gives a Gibbs free energy, which allows the calculation of phase diagrams, it still does not take into account the real anharmonic behavior of the interaction of atoms. This becomes a problem at high temperatures, when the anharmonic part of the atomic interactions cannot be neglected. Another case where the harmonic approximation fails are temperature-stabilized structures, such as β-quartz or β-cristobalite. In these structures the atoms are on average in high symmetry positions due to oscillations at high temperatures. However, these average positions are not stable at 0 K. Although the forces of the atoms at these positions are zero, they are not positioned at a minimum but at a saddle point. This leads to the appearance of imaginary phonon frequencies in the eigenvalue problem and makes an accurate determination of the free energies impossible. An alternative method to overcome this problem is described below.

2.4.2 Thermodynamic integration

Thermodynamic integration allows the accurate determination of the Gibbs free energy of complex crystals with anharmonic contributions. However, it is much more expensive than the finite displacement method. Large MD simulations with more than 1000 atoms on time scales of more than 10 ps seconds are required, which makes the method not well suited for calculations with DFT. We used the Frenkel-Ladd method[180] in Chapter 4 to calculate a comprehensive phase diagram of silica. For our calculations, we used the code `calphy`.[181] The thermodynamic integration method consists of two parts. First, a reference free energy must be calculated. Second, from this reference calculation,

an integration is performed to obtain the temperature or pressure dependence of the simulation.

To obtain the reference energy we define two Hamiltonians H_i and H_f. The Hamiltonian H_i is the initial Hamiltonian of a system where the free energy can be calculated analytically. In contrast, H_f is the final Hamiltonian with an unknown free energy. To determine the difference in free energy between the two states the Hamiltonian's are combined, and a time integration is performed switching from one Hamiltonian to the other. The combined Hamiltonian is given by,[181]

$$H(\lambda(t)) = [1-\lambda(t)]H_i + \lambda(t)H_f, \tag{2.20}$$

with $\lambda(t_i) = 0$ and $\lambda(t_f)$=1. To calculate the difference in the Gibbs free energy, the work done during the switching process needs to be calculated by,[181]

$$W^s = \int_{t_i}^{t_f} \frac{d\lambda}{dt}\left[\frac{\partial H(\lambda)}{\partial \lambda} + \frac{\partial P(\lambda)V}{\partial \lambda}\right] dt. \tag{2.21}$$

The difference in the Gibbs energy between the initial system and final system is given by,

$$\Delta G_{\text{ref}} = \frac{1}{2}(W^s_{i\to f} - W^s_{f\to i}). \tag{2.22}$$

The reason for averaging forward and backward integration is that dissipation energy is lost during the process of switching the Hamiltonian. However, if the switching time is long enough, it has been shown that the dissipation energy is the same in forward and backward switching and can cancel out.[182] An important part of this algorithm is the reference Hamiltonian. It should be somehow related to the system of interest and an analytical expression for the free energy should be available. In `calphy` two models are available. For solids, a system of N non-interacting harmonic oscillators is used, which has the following Hamiltonian,[181]

$$H_{HO} = \sum_{i=1}^{N}\left[\frac{\vec{p_i^2}}{2m_i} + \frac{1}{2}m_i\omega_i^2(\Delta\vec{r_i})^2\right], \tag{2.23}$$

with the momentum $\vec{p}_i$, the mass m_i, the frequency $\omega_i = \sqrt{\frac{k_i}{m_i}}$ with spring constant k_i and the displacement from the equilibrium position Δr_i of atom i. In the one-elemental case this is equivalent to an Einstein crystal, since all oscillators have the same frequency. From this the free energy can be derived to be,[181,183]

$$F_{HO}(N,V,T) = \frac{1}{2}\sum_i \hbar\omega_i + 3k_bT\sum_i \ln(1-\exp(-\hbar\omega_k/k_bT)) \approx 3k_BT\sum_i \ln\left(\frac{\hbar\omega_i}{k_BT}\right). \tag{2.24}$$

The latter part is the high temperature approximation, which has been used in `calphy`. For the liquid reference, `calphy` uses the Uhlenbeck-Ford model[184,185], which

is an extension of the ideal gas model. Within the Uhlenbeck-Ford model the interaction is described by a purely repulsive pair potential. The Hamiltonian of this model is given by,[181,185]

$$H_{UF} = \sum_{i=1}^{N} \frac{\vec{p_i^2}}{2m_i} - \sum_{i<j}^{N} p k_B T \ln\left[1 - \exp\left(-\left(\frac{r_{ij}}{\sigma}\right)\right)\right], \tag{2.25}$$

with the length scale σ and the distance between two particles r_{ij}. $p \leq 0$ is a scaling factor controlling the amplitude of the interaction. From this the free energy of the Uhlenbeck-Ford model can be determined,[181,185]

$$F_{UF} = F_{ig} + F_{UF}^{(ex)}, \tag{2.26a}$$

$$F_{UF}^{(ex)}(x,T) = k_B T \sum_{n=1}^{\infty} \frac{\tilde{B}_{n+1}(p)}{n} x^n, \tag{2.26b}$$

where F_{ig} is the free energy of the ideal gas and $F_{UF}^{(ex)}$ is Uhlenbeck-Ford excess free energy with $x = (\pi\sigma^2)^{3/2}\rho$. Here, ρ is the number density and $\tilde{B}_{n+1}(p)$ is a reduced virial coefficient. Based on these models, a reference energy can be calculated for liquids and solids. From these reference energies the dependence of the free energy on temperature and pressure needs to be determined. This can be done by standard thermodynamic integration, but for efficiency reasons this is done by an approach called reversible scaling. It has been shown that to determine the free energy dependence on temperature, the potential energy can instead be scaled by a factor λ while keeping the temperature fixed.[186] Based on this, the Gibbs free energy at a pressure P and temperature T_f can be calculated from,[181,185]

$$G(N,P,T_f) = G(N,P,T_i) - \frac{3}{2} k_B T_f N \ln\frac{T_f}{T_i} + \frac{T_f}{T_i}\int_1^{\lambda_f} \langle U\rangle + \frac{dP(\lambda)}{d\lambda}\langle V\rangle d\lambda, \tag{2.27}$$

where T_i is the temperature of the initial reference free energy state and $\langle U\rangle$ is the average inner energy. λ_f is the maximum scaling factor of the potential energy.

2.4.3 Phase diagram calculations

In this work we calculated phase diagrams in two different ways. First, using the finite displacement method for α-quartz, coesite, and stishovite within the quasi-harmonic approximation. Here we determined the pressure-low temperature phase diagram up to a pressure of 9 GPa. Within `phonopy` we used the default settings for these calculations. Secondly, we used the thermodynamic integration method to determine the high temperature phase diagram of silica up to a pressure of 4 GPa. Since the calculation of this phase diagram is more challenging compared to the other variant, we give some more details here.

In our phase diagram calculations with `calphy` we used 50,000 equilibration time steps before switching from one Hamiltonian to the other. This was followed by 800,000

switching steps to switch from the Hamiltonian to the Einstein crystal Hamiltonian. For the thermodynamic integration with reversible scaling we used 300 time steps/K. Instead of automatic determination of the spring constants in the Einstein model, we fixed these to 2 eV $Å^{-2}$ for oxygen and 4 eV/$Å^{-2}$ for silicon. To achieve convergence with system size, we used cell sizes of about 15,000 atoms.

Integration was typically performed between 600 K and 2600-3,000 K, depending on the stability of the polymorph. This is illustrated in Figure 2.2. Since cristobalite is only stable at high temperatures, we performed the integration only for temperatures above 1500 K to slightly above the melting point. Similarly, for higher accuracy, we split the integration interval of tridymite into a part above 1500 K and a part below 1500 K. As an example, the Gibbs free energies of these structures at a pressure of 0 GPa are shown in Figure 2.2a. We also show the free energies for α- and β-quartz, which present an additional challenge. Both structures dynamically transform into each other at a certain temperature. This happens even on MD timescales. Therefore, the transition between the two phases cannot be determined by thermodynamic integration, but was instead determined from simple MD simulations. The exemplary approach is shown in Figure 2.3. We performed MD simulations under NPT conditions for 100 ps at the same pressure but at different temperatures, with both α-quartz and β-quartz as input. The densities of these simulations for a pressure of 0 GPa are shown in Figure 2.3a-b. It is evident that there is a transition at a temperature of 850 K. To determine the transition temperature we fitted this curves by the following function,

$$\rho(T) \approx \begin{cases} a \cdot x^2 + b \cdot x + c & x < T_1 \\ 0.5 \cdot \cos\left(\dfrac{x - T_1}{T_2 - T_1}\pi\right) + 0.5 & T_1 < x < T_2 \\ d \cdot x + e & x > T_2 \end{cases}, \tag{2.28}$$

with fitting parameters a, b, c, d, e, T_1 and T_2. To determine the pressure dependence of the transition temperature, the whole procedure was repeated for several pressures. From this Figure 2.3c was obtained. This shows the transition line between α- and β-quartz, which is also the corresponding line used in the phase diagram.

Since inaccuracies occur, when performing thermodynamic integration across a phase boundary, we have integrated the energy for α-quartz only to 50 K below the transition line and for β-quartz only from a temperature of 50 K above the transition line. To obtain a phase diagram from the free energies calculated by thermodynamic integration, we performed integration over a wide pressure range. This is shown in Figure 2.2b for α-quartz. From these curves we performed Gibbs free energy fits as a function of pressure at 1 K intervals (See Figure 2.2c). We used third-order polynomials for these fits. [138]

2.5 Solid-state nudge elastic band method

Possible transition paths and transition barriers are essential to understand many phase transitions. In the following, we present the SS-NEB method, which can be used

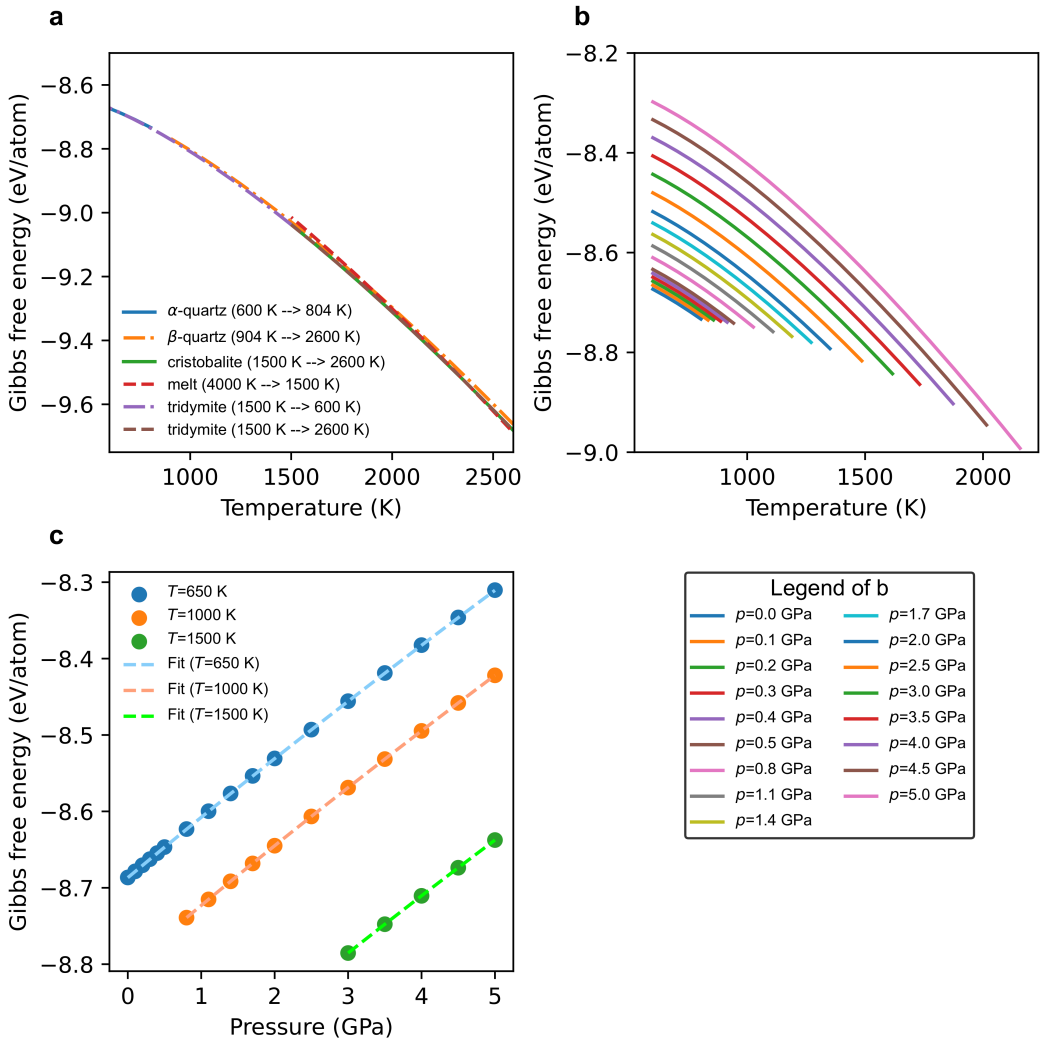

Figure 2.2: **Free energy calculations for a phase diagram.** (a) We show the Gibbs free energy at different temperatures for several polymorphs. For each polymorph, the temperature was determined over different intervals. Details are given in the text. (b) For α-quartz, thermodynamic integration was performed over temperature, repetitively at different pressures. The results for the Gibbs-free energy are shown in this plot. (c) Approximation of the free energy by polynomial fits to data points of α-quartz at the same temperature but different pressures. These fits are finally used to determine the phase diagram. Reproduced from Ref. 138. Original figure published under the CC-BY 4.0 license (https://creativecommons.org/licenses/by/4.0/).

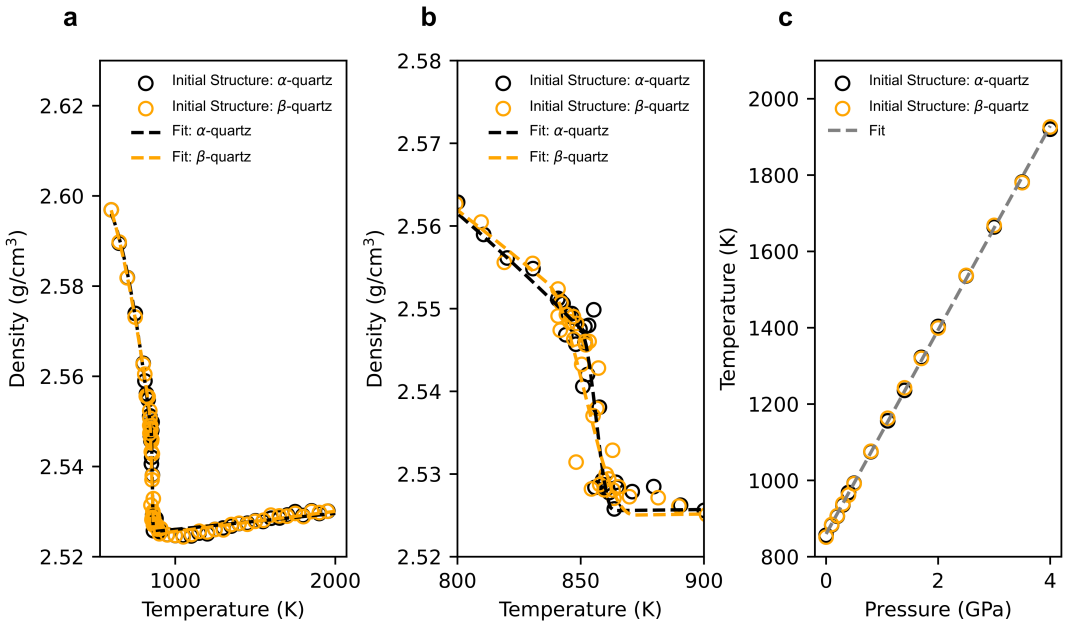

Figure 2.3: **α/β-quartz transition from MD simulations.** (a-b) Results of a series of MD simulations performed under NPT conditions at a pressure of 0 GPa and different temperatures. Shown are the densities after equilibration based on the α-quartz or β-quartz input structure and corresponding fit curves. Both figures show the same data, but in a different x-range. (c) From the plot in (a) and (b) different pressure transition temperatures have been determined, shown here as points. The phase transition line is obtained by fitting to these points. Reproduced from Ref. 138. Original figure published under the CC-BY 4.0 license (https://creativecommons.org/licenses/by/4.0/).

to investigate phase transformations under pressure and is used in this work in Chapter 5. The SS-NEB method[187] is a method for determining transition barriers between two phases with different cell sizes. Unlike the standard nudged elastic band (NEB) method,[188] it is not limited to transitions with constant cell sizes. The idea of the NEB method is that a certain number of images are connected by springs. The first image is the initial state and the last image is the final state. Initially, the intermediate images can be linearly interpolated between the two states. However, the transition states and the transition barrier are then determined by minimizing the forces of the images using the following forces,[187]

$$\mathbf{F}_i^{\mathrm{NEB}} = \mathbf{F}_i^{S_\parallel} + F_i^{\nabla_\perp}. \tag{2.29}$$

Here F_i^{∇} is the gradient of the interatomic potential, i.e. the actual force acting on the atom. The symbol $\perp$ indicates, that only the gradient of the interatomic potential perpendicular to the transition path is considered. $\mathbf{F}_i^S$ is the spring force based on the difference in coordinates between the image and the two neighboring images. In contrast to the force induced by the potential, here only the contribution parallel to the transition path plays a role, which is indicated by the symbol $\parallel$. In case of the standard

NEB, the force vector contains only the forces acting on the atoms, but not the stress contribution. However, SS-NEB extends the force vector by stress components to allow box changes within the calculation. The enthalpy in these states cannot be calculated by Equation 2.11 because the deformation is not necessarily hydrostatic. In contrast, the general enthalpy for the non-hydrostatic case is calculated by,[189,190]

$$\Delta H = \Delta E + \Omega \sigma^{\text{ext}} \cdot \epsilon, \tag{2.30}$$

where ΔE is the energy difference between the image and the reference state, ϵ is the strain tensor of the image relative to the reference state, and the volume of the reference supercell is given by Ω. σ^{ext} is the external pressure applied to the system.

We used the `FD-NEB` code[190,191] to perform the SS-NEB calculations, which is largely identical to the `tsase` code.[187,189,192] For our calculations, we used Cauchy stresses and a weight factor of 100 to reduce the influence of the stresses on the force vector. We also constrained the initial and final cells to have the same a-b vectors, so that only c direction box changes were allowed.

2.6 X-ray diffraction patterns and structure factors

In experiments, it is difficult to obtain bulk structural data directly. Instead, diffraction techniques are commonly used to gain insights into the atomic structure in an indirect way. While this is usually straight forward for crystalline materials, it is more difficult for amorphous materials. Extracting corresponding spectra from MD simulations is a useful tool to support the validity of simulations and to gain a better understanding of experimental observations.

2.6.1 X-ray diffraction patterns

X-ray diffraction (XRD) intensities in Chapter 5 are calculated using the Debye formula,[193]

$$I(q) = \sum_{i,j} f_i(q) \cdot f_j(q) \cdot \frac{\sin(q \cdot r_{ij})}{q \cdot r_{ij}}, \tag{2.31}$$

with the scattering vector q, the atomic scattering factor $f_a(q)$ and the distance r_{ij} between atom i and j. q can be calculated by,

$$q = 4\pi \sin(\Theta/\lambda), \tag{2.32}$$

where λ is the wavelength and Θ is the diffraction angle. The calculation of Equation 2.31 is in practice a computationally expensive task, especially for large systems in which all interatomic distances must be calculated. One method to reduce the computational and memory requirements is binning, where essentially the radial distribution function is computed and inserted into Equation 2.31 with corresponding weights for each distance. We used the fast and parallelized implementation of `ovito` to calculate

radial distribution functions.[194] A problem with the binning could be the creation of false Bragg peaks,[195] but due to the dense binning this was not an issue in our case. In all distance calculations we did not consider periodic boundaries.

2.6.2 Structure factors

The total scattering method can be used to experimentally determine the structure factor of a sample. As explained below, the Fourier transform of the structure factor corresponds to the pair distribution function (PDF). However, to obtain reliable PDFs, measurements up to high scattering vectors q are required.[196] Even then, in case of multicomponent systems, obtaining partial PDFs is quite difficult requiring for example isotopic substitution,[196] but it has been done for silica.[197]. In MD simulations, on the other hand, partial PDFs are readily available. From these, the structure factors can be calculated easily, as it was done in Section 4.3 and Section 6.2, using the following equations. In a multi-component system, the structure factors can be expressed by,[196]

$$S(q) = \sum_i \sum_j S'_{ij}(q), \tag{2.33}$$

where S'_{ij} is the partial structure factor origin from the distribution of i and j atom pairs. In case of Faber-Ziman structure factors the partial structure factors are given by,[196,198]

$$S'_{ij}(q) = \frac{c_i c_j f_i(q) f_j(q)}{(\sum_i c_i f_i(q))} S_{\alpha\beta}(q), \tag{2.34}$$

where f_i depends on q and is again the atomic form factor, while c_i is the concentration of species i. S_{ij} is given by,[196]

$$S_{ij}(q) = 1 + \frac{1}{q} \int_0^\infty G_{ij}(r) \sin(qr) dr, \tag{2.35}$$

with the distance r and the reduced partial PDF $G_{ij}(r)$, which is given by,[196]

$$G_{ij}(r) = 4\pi r \rho_0 (g_{ij}(r) - 1), \tag{2.36}$$

where ρ_0 is the number density and $g_{ij}(r)$ is the partial PDF. The integral in Equation 2.35 cannot be integrated up to infinity since it is limited by the box size. This leads to certain finite size errors. For X-ray structure factor calculations we used different atomic form factors over the time of the work. The q dependence of the atomic form factors have been approximated by data taken from Ref. 199 (Table 6.1.1.4). PDFs have been calculated using `ovito`.[194]

2.7 Structure identification

The structure identification algorithm is described in detail in Ref. 200. This was a joint work with Daniel Utt, who took care of the implementation of the code and the

development of the idea. The generation of training data for silica as well as the training and testing of the specific model was done by myself.

In the following we will present a structure identification algorithm, which can be used to differentiate between a wide range of silica structures. This algorithm was used in Chapter 5 to identify various high-pressure phases. Structure identification algorithms for simple crystal structures such as hexagonal close-packed (HCP), face-centered cubic (FCC), or body-centered cubic (BCC) have been available for some time. For example, polyhedral template matching (PTM)[201] and common neighbor analysis (CNA)[202] are widely used. However, for more complex structures, the availability of structure identification algorithms is very limited. To overcome this problem, we introduce an machine learning (ML)-based classification approach in the spirit of earlier ML-based structure identification methods.[203–206] The concept of the ML classifier is illustrated in Figure 2.4. As input to the classifier, we use point clouds of atoms centered around the atom of interest. In this particular case, we used the 64 nearest neighbors. The coordinates of these atoms are fed into a Dynamic Graph-Convolutional Neural Network (DG-CNN).[207] This DG-CNN then returns a score for each structure type, which was part of the training set. Based on these scores, the structure with the maximum score is selected as the prediction.[200]

Here, we will give some brief details about the training process. More details can be found in the corresponding publication.[200] We have selected 25 different structure types for the training. These include 23 crystal structures as well as the amorphous phase and the liquid phase. The 23 crystal structures include the following low pressure phases: α-quartz,[208] β-quartz, α-cristobalite,[209] β-cristobalite, α-moganite,[210] β-moganite, monoclinic tridymite[211] and higher temperature tridymite. The higher temperature polymorphs automatically appear from the lower temperature polymorphs in the MD simulation. We also used the following high pressure phases for training: $P3_221$,[82] $C2$,[68] d-NiAs-type,[75] $I2/a$,[212] $NaTiF_4$-type,[72] $P2_1/c$,[72] $P3_2$,[83] $Pnc2$,[213] SnO2-type,[72] rosiaite-type,[60] coesite,[214] stishovite,[215] seifertite[216] and pyrite-type.[36] The $CaCl_2$-structured silica automatically appears at high pressures, when stishovite is compressed. The general procedure for generating training data for the DG-CNN was to perform MD simulations from low temperatures to above the melting point. All structures below the melting point are then assigned to a particular crystal structure. In the case of solid-solid phase transitions, the phase transition point is identified to correctly label the training data. Structures above the melting point are labeled as melt. Additional amorphous structures are generated by melt-quench simulations. The whole procedure is repeated depending on the stability range of the polymorph at different pressures.[200]

A drawback of this algorithm is that it can only identify structures that are in the training database. Structures not covered in the training database obtain a random score and are identified as any of the structure types in the database. Currently, there is no easy way to get the uncertainty of the prediction. Therefore, we decided to use

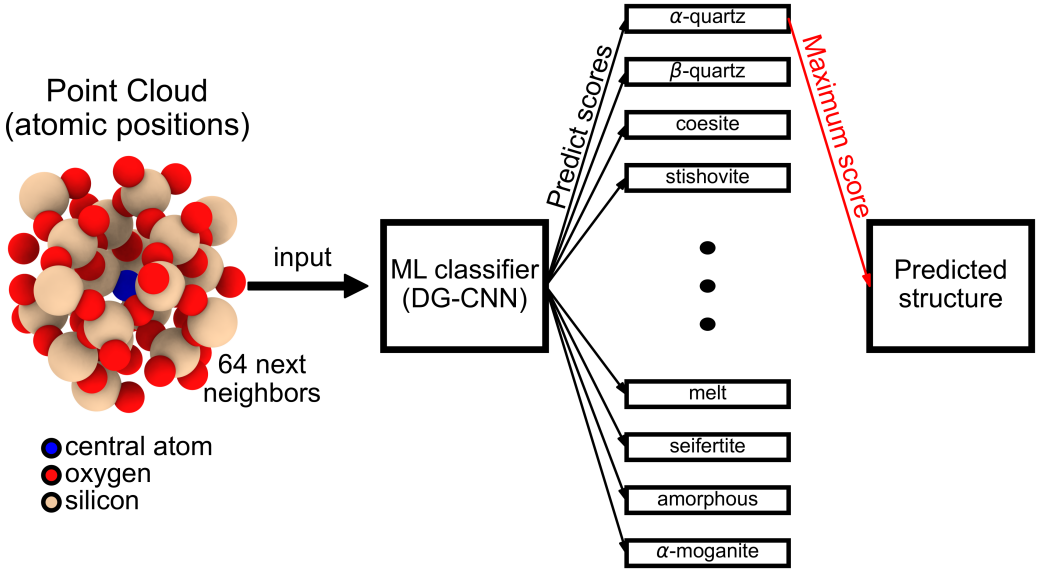

Figure 2.4: **Machine-learning based structure identification for silica.** For the structure identification first the environment of a central atom (blue) is extracted. We always consider a constant number of 64 next neighbors. Although we show the information about the chemical species in this figure, we do not consider the chemical species as input for the ML algorithm at the moment. Only the coordinates are fed into a ML based classification algorithm. In our case we use the DG-CNN algorithm.[207] This gives for each structure type, which was in the training dataset a score. The structure with the maximum score is then chosen to be the predicted structure.

a large number of structures in the hope that all structures that might appear in our simulations would be covered by this training procedure.

2.8 Interatomic potentials

As mentioned in Section 2.1 and 2.3 forces are essential for MD simulations. These forces can be derived from the derivative of the interatomic potentials with respect to the positions:

$$\vec{f}_i = -\frac{\partial V}{\partial \vec{r}_i}. \tag{2.37}$$

As indicate in Section 1.3 many classical interatomic potentials have been proposed for silica in the past. The interatomic potentials, which have been used, in this work, are introduced in detail in Subsection 2.8.1. The theoretical background of MLIPs types used in this work are then presented in Subsection 2.8.2.

2.8.1 Classical interatomic potentials

BKS and CHIK potentials

As mentioned in Section 1.3 the van Beest, Kramer, van Santen (BKS)[80] model is one of the most successful interatomic potentials for silica. A modified version of this potential is the Carré, Horbach, Ispas, Kob (CHIK) potential.[108] This potential is given by,

$$V_{ij} = \frac{q_i q_j}{4\pi\epsilon_0 r_{ij}} + A_{ij}\exp\left(-B_{ij}r_{ij}\right) - \frac{C_{ij}}{r_{ij}^6} + \frac{D_{ij}}{r_{ij}^{24}}, \tag{2.38}$$

where A_{ij}, B_{ij}, C_{ij} and D_{ij} are fitting parameters, r_{ij} is the distance between atom i and atom j and q_i is the corresponding atomic charge. In contrast to the BKS the CHIK potential contains the additional D_{ij}/r_{ij}^{24} term, which prevents the potential to become attractive at very short distances.

Since at high temperatures the attractive behaviour of the BKS potential is indeed an issue, we used for high-temperature simulations a modified BKS model, which goes over in a harmonic term at short distances.[217,218] In case of the BKS potential, we used a cutoff of 15 Å and in case of the CHIK potential a cutoff of 10 Å for the crystalline phase and 6.5 Å and for liquid and amorphous phases. Both potentials have been used in Chapter 4.

Vashishta-type potentials

Both, the Vashishta potential from 1990[43] and the Broughton potential from 1997,[109] have a very similar form. We used both potentials in Chapter 4. In these models, the total potential energy of the system is given by,[43]

$$V_{total} = \sum_{1\le i<j\le N} V_2(r_{ij}) + \sum_{1\le i\le j\le k\le N} V_3(r_{ij}, r_{jk}, r_{ik}), \tag{2.39}$$

where $V_2(r_i j)$ are the two-body interactions and $V_3(r_{ij}, r_{jk}, r_{ik})$ are three-body interactions. Two-body interactions are composed of,[43]

$$V_2(r_{ij}) = \underbrace{\frac{H_{ij}}{r_{ij}^{\eta_{ij}}}}_{\text{repulsion}} + \underbrace{\frac{q_i q_j}{r_{ij}}}_{\text{Coulomb}} \underbrace{- \frac{1/2\left(\alpha_i q_j^2 + \alpha_j q_i^2\right)}{r_{ij}^4}\exp -r_{ij}/r_{4s}}_{\text{charge-dipole}}, \tag{2.40}$$

where H_{ij}, and η_{ij} are parameters, which determine the repulsion of two atoms, and α_i is the polarizability of atom i. r_{4s} is a parameter determining the decay of the dipole-ion interactions. The three-body interactions are given by,[43]

$$V_3(r_{ij}, r_{jk}, r_{ik}) = B_{jik} f(r_{ij}, r_{ik}) p(\Theta_{jik}, \overline{\Theta}_{jik}), \tag{2.41}$$

where B_{jik} is a parameter, $f(r_{ij}, r_{ik})$ is a function, which includes energy terms from bond stretching, and $p(\Theta_{jik}, \overline{\Theta}_{jik})$ is a function, which includes energy terms from bond bending. $\overline{\Theta}_{jik}$ is a parameter and Θ_{jik} is the angle between the bonds between atom i

and j and i and k. Parameters for these functions can be found in the corresponding publications.[43]

Munetoh potential

The Munetoh potential[117] is an interatomic potential characterizing the Si-O interaction in form of a Tersoff interaction model.[219,220] The pair interaction energy between two atoms i and j in this model is given by,[117]

$$V_{ij} = f_c(r_{ij})\big(f_R(r_{ij}) + b_{ij} f_A(r_{ij})\big), \tag{2.42}$$

where $f_c(r_{ij})$ is a cutoff function,$f_R(r_{ij})$ is a repulsive pair function and $f_A(r_{ij})$ is an attractive pair function. These functions are given by,[117]

$$f_R(r_{ij}) = A_{ij}\exp(-\lambda_{ij} r_{ij}) \tag{2.43a}$$
$$f_A(r_{ij}) = B_{ij}\exp(-\mu_{ij} r_{ij}), \tag{2.43b}$$

with parameters A_{ij}, B_{ij}, λ_{ij} and μ_{ij}. b_{ij} is the bond order parameter given by,[117]

$$b_{ij} = \chi_{ij}(1 + \beta_i^{n_i}\zeta_{ij}^{n_i})^{-1/2n_i} \tag{2.44a}$$
$$\zeta_{ij} = \sum_{k\neq i,j} f_c(r_{ik})\omega_{ik} g(\theta_{ijk}) \tag{2.44b}$$
$$g(\Theta_{ijk}) = 1 + c_i^2/d_i^2 - c_i^2/(d_i^2 + (h_i - cos(\Theta_{ijk})^2)), \tag{2.44c}$$

with parameters β_i, ω_{ik}, χ_{ij}, n_i, c_i, d_i and h_i. This interaction model does not contain charges, unlike the BKS and Vashishta style potential in the earlier sections. The exact parameterizations can be found in Ref. 117. Since the Munetoh potential can be used for SiO_2 as well as for mixed Si–O systems, we used it in Chapter 4 and 6.

Charged-optimized many-body potentials

To model mixed system of silicon and silica, we used a second generation Charge-optimized many-body (COMB) potential for Si-SiO_2 in Chapter 6.[114] This potential is based on a number of earlier developed potentials,[115,116] combining a charge-equilibration procedure with a Tersoff potential. The total energy in the COMB formalism is given by,[114]

$$V = \sum_i \left[V_i^S + \frac{1}{2}\sum_{j\neq i} V_{ij}(r_{ij}, q_i, q_j) + V_i^{BB} \right], \tag{2.45}$$

where V_i^S and V_i^{BB} are self-interaction and bond-bending energies of atom i. V_{ij} is the interaction potential between two atoms and is given by,

$$V_{ij}(r_{ij}, q_i, q_j) = V_{ij}^R(r_{ij}) + V_{ij}^A(r_{ij}, q_i, q_j) + V_{ij}^I(r_{ij}, q_i, q_j), \tag{2.46}$$

where $V_{ij}^{R}(r_{ij})$ is the repulsive term, $V_{ij}^{A}(r_{ij},q_i,q_j)$ is the attractive term and $V_{ij}^{L}(r_{ij},q_i,q_j)$ is the long-range Coulomb term. These terms are given by the following equations,[146]

$$V_{ij}^{R}(r_{ij}) = f_{S_{ij}} A_{ij} \exp(-\lambda_{ij} r_{ij}), \tag{2.47a}$$

$$V_{ij}^{A}(r_{ij},q_i,q_j) = -f_{S_{ij}} b_{ij} B_{ij} \exp(-\alpha_{ij} r_{ij}), \tag{2.47b}$$

$$V_{ij}^{I}(r_{ij},q_i,q_j) = J_{ij}(r_{ij}) q_i q_j, \tag{2.47c}$$

where the repulsive term $V_{ij}^{R}(r_{ij})$ and the bond order term b_{ij} are in principle identical to the terms in the pure Tersoff formulation (See Equation 2.43a and 2.44a). In contrast, to the Tersoff formulation the parameter B_{ij} depends on the atomic charges and is given by,[146]

$$B_{ij} = \sqrt{B_{S_i} B_{S_j}} \quad \text{with} \quad B_{S_i} = B_i \exp(\alpha_i D_i)\left[a_{B_i} - \left|b_{B_i}(q_i - Q_{O_i})\right|^{n_{B_i}}\right], \tag{2.48}$$

where the latter part is describing, whether the charge of atom i is in a meaningful range. b_{B_i} is normalizing the charge differences to the mean charge Q_{O_o}. This mean charge is given by,[146]

$$Q_{0_i} = \left(Q_{U_i} + Q_{L_i}\right)/2, \tag{2.49}$$

where Q_{U_i} and Q_{L_i} are the upper and lower charge bounds. Also, a_{B_i} depends on these two values. In contrast, to the earlier models based on charges like the BKS and the CHIK model, the COMB from 2010 model does not assume to have point charges, but instead replace them with Coulomb integrals over the Slater 1s orbitals given by the charge coupling factor,[114]

$$J_{ij}(r_{ij}) = \int d^3 r_i \int d^3 r_j \frac{\rho_i(r_i,q_i)\rho_j(r_j,q_j)}{r_{ij}} \tag{2.50a}$$

$$\rho_i(r_i,q_i) = q_i \frac{\xi_i^3}{\pi} \exp(-2\xi_i |r_{ij} - r_i|), \tag{2.50b}$$

with ξ_i determines, how fast the electron density is decaying. The self energy V_i^S describes how likely charges are located at a certain atom,[114]

$$V_i^S(q_i) = \chi_i q_i + J_i q_i^2 + K_q q_i^3 + L_i q_i^4 + V_i^{\text{lattice}}, \tag{2.51}$$

with fitting coefficients χ_i, J_i, K_i and L_i and a penalty term V_i^{lattice}, which includes the ionic contributions of the lattice. Finally, the bond bending term V_i^{BB} has a very similar form to the bond bending term in the Vashishta potential. The charges in the system are determined using a charge-equilibration[145] approach based on an effective Lagrangian.[116,221]

2.8.2 Machine learning interatomic potentials

Literature review

In the following we will first give a literature review of MLIPs in general, and then we will describe several approaches in detail. MLIPs are a new class of interatomic potentials, which were introduced by Behler and Parrinello in 2007.[155] MLIPs are based on three essential components:[154]

1. **The training database.** This database contains structural files of atomic configurations. Each structure is labelled with one energy and forces for each atom, normally calculated by DFT.

2. **The atomic descriptor.** The descriptor is a fingerprint for the individual atomic environments and makes it possible to feed structural information into the machine learning algorithm. In general, the descriptor needs to be permutational, rotational and translational invariant.

3. **The regression algorithm.** This part is the machine-learning part, in which the machine-learning regression algorithm is trained to the energies and forces in the database with the fingerprints as input.

Finally, after training the MLIP can be used for fast energy and forces evaluations by calculating the atomic descriptors and feeding them into the machine-learning algorithm.

Training databases have been generated in the past by various approaches. These are an essential part of each MLIP since they contain all information that the algorithm is trained on. In reverse, this means that the potential cannot be better than the data it was trained on. The quality of the training data is made up of two decisions:

1. How to calculate energies and forces?

2. Which structures are fed into my training set?

As already mentioned, for the evaluations of energies and forces DFT is commonly employed.[154] Most DFT calculations for machine-learning use standard generalized gradient approximation (GGA) exchange-correlation functionals like the Perdew-Burke-Ernzerhof (PBE) exchange-correlation functional[222–224] or the local density approximation (LDA).[225,226] In case of molecules, higher order methods like coupled-cluster methods have also been employed.[227] However, these methods are mostly too expensive to be used for solids.[228] In the case of silica, an issue arises from the fact that the standard exchange-correlation functionals are known to fail to describe the energetic order of the polymorphs in silica, correctly.[229] Therefore, for this system, additional care must be taken to select a proper exchange-correlation functional.

After the decision has been made on how to calculate energies and forces, the structural data for the training database needs to be generated. There are several options for this. The first and simplest approach is the manual construction of structures.

This can start with databases such as the Materials Project database or the Inorganic Crystal Structure Database,[13,230] where a wealth of crystal structures are available. After extracting the crystal structure, a large amount of possible distortions of the lattice parameters and the atomic positions are generated randomly.[158] Additionally, defects like dislocations and surfaces can be constructed manually and added to the database.[223] Other ways to generate training data include the use of random structure search or *ab initio* MD snapshots.[225,231] For liquid and amorphous structures, the generation of training data is more complicated compared to crystalline structures. Exemplary structures cannot be downloaded directly from a database. Instead, the structures are often generated iteratively. Initially, amorphous and liquid structures are generated by *ab initio* MD. This data is then used to fit a first potential. Subsequently, the potential is used to perform much cheaper MD simulations, from which snapshots are extracted to perform DFT calculations again and add the corresponding structures to the database. Afterwards, the potential is refitted, and the whole process is repeated.[155,232,233] The issue, which comes with this procedure, is that also structures, which are similar to those already in the database, are calculated in an expensive DFT calculation.

To overcome this issue, uncertainty estimates or indicators are essential. These approaches enable the calculation of the degree of uncertainty of a machine-learning interatomic potential for a specific structure or environment. When this degree of uncertainty exceeds a certain threshold, the structure is calculated within DFT, added to the database, and the potential is refitted. This process is called active learning and the key element of this approach is the uncertainty estimate. The first work performing simulations like this with MLIPs was performed by Artrith and Behler, which used the query-by-committee approach.[234] In this approach several neural network potentials (NNP) are trained on the same training data, but are, for example, initialized with different random seeds. When several fits give a close result for the same structure, it can be assumed that this structure is sufficiently covered in the training database. However, in the case of deviating results, this structural space is not covered well enough, and therefore the structure needs to be added to the database. Other machine-learning algorithms, such as, Gaussian process regression, can make use of Bayesian error estimates to approximate the uncertainty without the need to fit several models.[235,236] Linear machine-learning methods, which are used, for example, in moment tensor potentials (MTP) or atomic cluster expansion (ACE) potentials, frequently use the D-optimality criterion.[237–240] This is a geometric criterion based on the vectors formed by the basis functions. N basis function vectors with the length N are arranged in a symmetric matrix in such a way that the determinant of the matrix is maximized. Depending on the implementation, these basis function vectors are atom specific[237,240] or structure specific.[238,239] Therefore, the N basis function vectors correspond to N atoms or structures. The extrapolation behavior of another structure can then be calculated by evaluating whether the determinant of the $N \times N$ matrix is increasing by replacing one vector with the basis function vector of the new cell. More details can be found later in this section. To further increase the speed of active learning simulations, approaches like 'hyperactive learning' have been introduced, which drive the MD simulations into direction of higher uncertainty.[241]

All the mentioned active learning methods have one restriction. They can only be used for cells that are small enough to be calculated within DFT calculations. However, sometimes a potential works well within a small-scale simulation but may fail in simulations with millions of atoms. In these cases, it would be extremely beneficial if one could obtain *ab initio* forces of the atoms, which have environments unknown to the potential. One very simple approach would be to just cut out the atoms with their surrounding regions and put them into a smaller DFT-feasible box. However, this produces highly unreasonable interfaces at the boundaries of the box or surfaces if an additional vacuum layer is added. One approach to circumvent this issue was proposed by Hodapp and Shapeev.[242] They constructed symmetrized periodic cells from extracted dislocation structures. However, this approach works only for crystalline systems. Other approaches also extract structures from large-scale simulations and feed them into small-sized boxes. While the atoms around the atom of interest are kept fixed, the atoms at the boundary are minimized with respect to their uncertainty.[237,243]

Besides the database, the choice of the machine-learning algorithm and the descriptor is essential for a good MLIP. We already mentioned some approaches but will have a more extensive look at these approaches now. The first type of MLIP called NNPs was already proposed by Behler and Parrinello in 2007.[155] These potentials take different types of 2- and 3-body descriptors, commonly named as Behler-Parrinello symmetry functions, as input for a neural network.[155,244] Based on these symmetry functions and similar ones, several frameworks for NNPs have been developed.[159,162,245] In 2010 Bartók *et al.* introduced the Gaussian approximation potential (GAP), which is not based on neural network techniques but instead on Gaussian process regression.[158,246] These potentials mainly use the smooth overlap of atomic positions (SOAP) descriptor.[14] In the following years, several other potentials have been developed. This starts from the spectral neighbor analysis potential,[247] goes over to MTPs[157] and the ACE potentials.[156] In contrast to GAP and NNP, which use highly non-linear machine-learning techniques, these techniques use a diverse descriptor in combination with a not so flexible linear or slightly non-linear machine-learning approach.[248–252] Specifically, these linear approaches demonstrate high accuracy in benchmark studies coupled with high computational efficiency.[249,253]

The mentioned approaches are up to this point all short range and do not include long-range contributions. However, for electrostatics and van-der-Waals interactions incorporating long-range interaction might be necessary to allow a full description of the system. Van-der-Waals interactions have been included by defining an overlay potential of a long-range $V \sim 1/r^6$ term in combination with a standard machine-learning potential.[16,254] For charges, different models have been developed in the past. One simple approach is to use fixed charge models, similar to the van-der-Waals interactions.[255] However, as mentioned earlier, this limits the applicability to stoichiometric mixtures. Artrith *et al.* overcame this issue by using a machine-learning model to predict the atomic charges based on the local environment.[256] Even more advanced approaches predict the electronic affinity based on the local environment instead of the atomic charges and subsequently perform a global-charge equilibration.[257]

Machine-learning potentials in this work

In the following, we will present several MLIP approaches, which have been used in this work. We used three different types of MLIPs. We started using GAP, which use Kernel regression as ML method[158] and mainly the SOAP[14] vector as descriptor. The second MLIP type, which we used are the MTPs. These potentials use Moment tensors as descriptor and a linear regression method in case of one-component systems[157] and non-linear regression in case of multi-component systems.[252] Similarly, the last type of potentials, the ACE potentials use the ACE as descriptor combined with linear or non-linear regression.[156] In the next section, we will discuss these potential types more in detail. In general and as already mentioned in Section 1.3, all these potential types we discuss here are based on the assumption that the total energy V_{tot} is composed of atomic energies V_i,

$$V_{tot} = \sum_{i}^{N} V_i, \tag{2.52}$$

with N atoms. Also, all models discussed here are purely short-ranged. That means, that the descriptor of each atom is only considering the atoms within a given cutoff.

Gaussian approximation potentials

GAPs were introduced in 2010 and are one of the most common MLIP type nowadays.[158] One reason for the widespread use of this potential type is the LAMMPS interface combined with the QUantum mechanics and Interatomic Potentials (QUIP) code (https://github.com/libAtoms/QUIP).[258,259] This code was also used in this work to fit GAPs. In GAP the atomic energy of an atom i is calculated by,[14]

$$V_i(\vec{x}) = \sum_{m=1}^{M} \alpha_m K(\vec{x}, \vec{x}_m), \tag{2.53}$$

where M is the number of sparse points in the Gaussian process regression approach, α_k are the fitting coefficients and the vector $\vec{x}$ contains the coordinates of the atoms around the central atom, while $\vec{x}_m$ contains the coordinates of the atoms around the reference atom. $K(\vec{x}, \vec{x}_m)$ is the kernel function, which gives a similarity between both environments. This value lays between 0 for no similarity and 1 for complete agreement. Following from this, GAP can be explained as approach that takes the atomic environment of your atom of interest ($\vec{x}$) and compares it to all the environments in the training set ($\vec{x}_m$). To reduces computational cost, not all environments in the training dataset are used. Otherwise, the cost of GAP would increase with the size of the training dataset. Instead, only the M most representative points are used.

The most important part of GAP are the kernels. Different kernels have been used in the past, most relevant the SOAP and the 2-body kernel. The 2-body kernel is given by,[246]

$$K(r_{ij}, r_m) = \exp\left(-\frac{|r_{ij} - r_m|^2}{2\Theta^2}\right), \tag{2.54}$$

where Θ is a hyperparameter and r_m are commonly M equally distributed distances on a grid. In the cases of the two-body kernel, the sum over each bond needs to be considered additionally to the sum over each atom.[246] The issue with the pure two-body descriptor is that it is obviously only a rough approximation. For a proper description of the system incorporating many-body descriptions is necessary. One example for this, is the SOAP kernel. The idea of SOAP is to start from a similarity between two atomic environments given by,[14]

$$S(\rho, \rho') = \int \rho(\vec{r})\rho'(\vec{r})d\vec{r}, \tag{2.55}$$

which is the overlap integral over two atomic densities,

$$\rho(\vec{r}) = \sum_i \exp(-\alpha|\vec{r} - \vec{r}_i|^2), \tag{2.56}$$

where each atom has a density distribution of a Gaussian with a width given by α, which is another hyperparameter. This similarity is not rotationally invariant, yet, and cannot be used as a kernel therefore. To make a rotationally invariant kernel from it, we define,[14]

$$k(\rho, \rho') = \int |S(\rho, \hat{R}\rho')|^n d\hat{R}, \tag{2.57}$$

which is an integral over all possible rotations. By normalization, we receive the SOAP kernel,[14]

$$K_{\mathrm{SOAP}}(\rho, \rho') = \left(\frac{k(\rho, \rho')}{\sqrt{k(\rho, \rho)k(\rho', \rho')}}\right)^{\zeta}, \tag{2.58}$$

with another hyperparameter ζ, which can be used to increase the sensitivity of the SOAP kernel. This integral seems to be computational quite expensive. However, by expressing the Gaussians as spherical harmonics it can be expressed in a computationally very efficient way, which results in the dot product of two so called SOAP vectors, where each of the vectors describes one atomic environment. Although GAPs are well established in the field, they come with some shortcomings. The first shortcoming of GAP is the speed. Over the years after the development of SOAP several other approaches have been developed, which provide a better trade-off between speed and accuracy.[249,253] Therefore, switching to other approaches can allow larger simulations over longer time-scales. The second issue is the issue of *completeness*. Naively, one would expect from the derivation of the SOAP vector, that this vector is *complete* in the sense that two different environments cannot have the same SOAP vector. However, it has been shown that SOAP is like several other descriptors not complete.[260] However, there exist complete descriptors, e.g. the ACE[261] and the moment tensors,[157] which are described in the next sections.

Moment tensor potentials

MTPs have been introduced several years after GAP. A good review of MTPs can be found in Ref. 262, which was also the basis for this summary. In contrast to GAP they do not use kernels, but instead a linear regression method to approximate the energy,[157]

$$V_i(\vec{n}_i) = \sum_\alpha \xi_\alpha B_\alpha(\vec{n}_i), \tag{2.59}$$

where ξ are the linear fitting coefficients and B_α are basis functions depending on the local environment $\vec{n}_i$ of atom i. In case of multicomponent systems current MTP approaches include additional non-linear components.[238,252] The basis functions of MTP are based on moment tensors given by,[262]

$$M_{\mu,\nu}(\vec{n}_i) = \sum_j \overbrace{f_\mu(|r_{ij}, z_i, z_j)}^{\text{radial basis}} \overbrace{\underbrace{\vec{r}_{ij} \otimes \ldots \otimes \vec{r}_{ij}}_{\nu \text{ times}}}^{\text{angular basis}}, \tag{2.60}$$

where $\otimes$ is the outer tensor product and the radial basis is expanded in the following form,[262]

$$f_\mu(|r_{ij}|, z_i, z_j) = \sum_\beta^{N_Q} c^{(\beta)}_{\mu,z_i,z_j} Q^{(\beta)}(|r_{ij}|), \tag{2.61}$$

with $Q^{(\beta)}(|r_{ij}|)$ given by,[262]

$$Q^{(\beta)}(|r_{ij}|) = \begin{cases} \phi^{(\beta)}(|r_{ij}|)(R_{\text{cut}} - |r_{ij}|)^2 & \text{if} \quad |r_{ij}| < R_{\text{cut}} \\ 0 & \text{if} \quad |r_{ij}| \geq R_{\text{cut}}, \end{cases} \tag{2.62}$$

and $\phi^{(\beta)}(|r_{ij}|)$ commonly being Chebyshev polynomials and R_{cut} being the cutoff radius. N_Q is the number of radial basis functions and is a hyperparameter, which should be tuned for each system. Depending on the value of μ the moment tensors are scalars, vectors, matrices or even higher order tensors. Thus, they cannot be used directly as basis functions B_α. Instead, the basis functions are defined as contractions of these tensors. To define how many moment tensors are incorporated in a MTP a level of tensor is defined by,[262]

$$\text{lev} M_{\mu,\nu} = 2 + 4\mu + \nu. \tag{2.63}$$

When two or more moment tensors are combined by contraction to a basis function, the level of all tensors add up. Finally, a MTP with level lev_{max} includes all possible basis functions under the conditions of $\text{lev} B_\alpha \leq \text{lev}_{\text{max}}$. lev_{max} is next to N_Q the second hyperparameter, which determines the accuracy of a MTP. A higher lev_{max} comes along with higher flexibility and normally a higher accuracy, however, at the same time also higher computational costs.

Next to the efficient evaluation of energies and forces,[253] MTPs have another big advantage. They have an easy-to-use active learning approach implemented based on

the D-optimality criterion.[239] This active learning allows to calculate an extrapolation grade γ during MD simulations. If this extrapolation value exceeds 1 the potential is extrapolating, which means that the current configurations are not covered within the training dataset. There is a certain range, where the extrapolation is still reliable until the potential becomes unstable at some point. This allows an easy estimation during MD simulations, whether the potential needs to be retrained with more data or whether it is reliable. Moreover, it is an efficient technique to sample more training data. To define the extrapolation grade, first per structure basis functions $b_\alpha(\mathrm{cfg})$ are defined,[157]

$$V_{tot} = \sum_i V_i(\vec{n}_i) = \sum_i \sum_\alpha^M \xi_\alpha B_\alpha(\vec{n}_i) = \sum_\alpha^M \xi_\alpha \underbrace{\sum_i B_\alpha(\vec{n}_i)}_{b_\alpha(\mathrm{cfg})}. \tag{2.64}$$

Based on these basis functions a $M \times K$ matrix can be constructed with the number of basis functions M and the number of structures in the training database K,[262]

$$B = \begin{pmatrix} b_1(\mathrm{cfg}_1) & \cdots & b_m(\mathrm{cfg}_1) \\ \vdots & \ddots & \vdots \\ b_1(\mathrm{cfg}_K) & \cdots & b_m(\mathrm{cfg}_K). \end{pmatrix} \tag{2.65}$$

This matrix B is modified to be quadratic by retaining only the M configurations from the training set that yield the highest determinant of the corresponding quadratic $M \times M$ matrix A. The inverse of A, A^{-1} can be used to evaluate, whether some other configuration for example from a MD simulation is extrapolating. In the case of extrapolation, inserting the vector of basis functions of this structure into the matrix A would increase the determinant. Correspondingly, the extrapolation value γ can be computed by,[262]

$$\gamma(\mathrm{cfg}_{\mathrm{new}}) = \max_{1 \le j \le M} |c_j| \tag{2.66}$$

with the components c_j given by,[262]

$$(c_1 \dots c_M) = (b_1 \dots b_M) A^{-1}. \tag{2.67}$$

While this active learning scheme uses efficient basis functions per structure, recently, also the option of defining an extrapolation grade per atom has been implemented.[240] However, this approach was not used in this work. For fitting of MTPs we used the `MLIP` code (https://gitlab.com/ashapeev/mlip-2).[262]

Atomic cluster expansion

In 2019 Drautz introduced the ACE.[156] ACE origins from the spin cluster expansion[263] and the lattice cluster expansion.[264] The approach of the ACE is similar to MTPs, however, instead of moment tensors, ACE uses spherical harmonics as angular basis functions. Again the energy is expanded linearly by,[156,248]

$$V_i = \sum_{\mathbf{v}} c_{\mathbf{v}} B_{i\mathbf{v}}, \tag{2.68}$$

where $B_{i\mathbf{v}}$ are the basis functions and $c_{\mathbf{v}}$ are fitting coefficients. To define the basis functions similar to SOAP a neighborhood density,[156]

$$\rho_i(\vec{r}) = \sum_j \delta(\vec{r} - \vec{r_{ji}}), \tag{2.69}$$

is defined. In contrast to SOAP not Gaussian's but δ-functions are used. From this density and an one-particle basis ϕ_v the atomic base can be defined by,[156]

$$A_{iv} = \langle \rho_i | \phi_v \rangle = \sum_j \phi_v(\vec{r_{ij}}) \quad \text{with} \tag{2.70a}$$

$$\phi_v(\vec{r}) = \sqrt{4\pi} R_{nl}(|\vec{r}|) Y_l^m\left(\frac{\vec{r}}{|\vec{r}|}\right), \tag{2.70b}$$

where $v = (nlm)$, R_{nl} are radial basis functions, which can be for example Chebyshev polynomials or Bessel functions and Y_l^m are spherical harmonics.[156] To receive permutational invariance and the so called 'A-basis', products of these atomic basis functions are required,[248]

$$A_{\mathbf{v}} = \prod_{t=1}^{K} A_{v_t}, \qquad \mathbf{v} = (v_1, \ldots, v_K), \tag{2.71}$$

where $(K+1)$ is the body order of the basis function. This basis is still not rotational invariant. Similarly, as for GAP (see Equation 2.57) an integral over all possible rotation is used to obtain the final basis functions,[248]

$$B_{\mathbf{v}} = \int \prod_{t=1}^{K} A_{v_t}(\hat{R}\vec{r_{ij}}) d\hat{R} = \sum_{\mathbf{v}'} C_{\mathbf{v}\mathbf{v}'} A_{\mathbf{v}'}, \tag{2.72}$$

where $C_{\mathbf{v}\mathbf{v}'}$ are the Clebsch-Gordan coupling coefficients.[248] One issue of this linear ACE expansion from Equation 2.68 is that is very slowly converging with the number of basis functions. Drautz suggested therefore the use of a non-linear version of ACE.[156] The most common version of non-linear ACE is inspired by the Finnis-Sinclair formalism,[237,265]

$$V_i = \varphi_i^{(1)} + \sqrt{\varphi_i^2}, \tag{2.73}$$

where $\varphi_i^{(k)}$ is defined as linear expansion as in Equation 2.68,[237]

$$\varphi_i^{(k)} = \sum_{\mathbf{v}} c_{\mathbf{v}}^{(k)} B_{i\mathbf{v}}. \tag{2.74}$$

In general, non-linear ACE can have arbitrary forms,

$$V_i = F(\phi_i^{(1)}, \phi_i^{(2)}, \ldots, \phi_i^{(P)}). \tag{2.75}$$

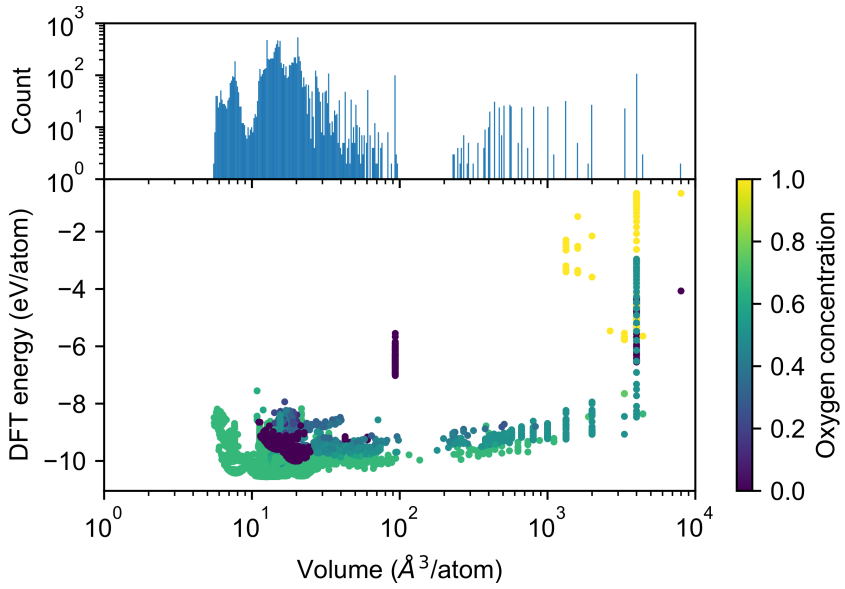

Figure 2.5: **Structures in the database with their corresponding energies and volumes.** Overview of the energy of all structures in the final SiO database from Chapter 3.

In this work we fitted ACE potentials using the `pacemaker` code (`https://pacemaker.readthedocs.io`).[237,249,266]

2.9 Density functional theory

Energies and forces for training the MLIPs are provided by DFT data. In the following we will give a brief overview on how DFT works and give details about our DFT calculations. The construction of the database is explained in Chapter 3. Nevertheless, we show an overview of the DFT energies provided for the database in Figure 2.5. The database is built from more than 10,000 DFT calculations. How these DFT calculations work and what are possible limitations of the resulting energies and forces is explained in the following.

The general time-independent Schrödinger equation is given by,[164]

$$\hat{H}\psi = E\psi, \tag{2.76}$$

where ψ is the many-electron wave function and E are the eigenvalues of this wave function. In case of the Born-Oppenheimer approximation[267] the electrons and the nuclei can be treated separately. This leads to a Hamiltonian given by,[164]

$$\hat{H} = \underbrace{\frac{\hbar^2}{2m_e}\sum_{i=1}^{N}\nabla_i^2}_{\text{kinetic energy}} \underbrace{-e^2\sum_{I=1}^{P}\sum_{i=1}^{N}\frac{Z_I}{|R_I - r_i|}}_{\text{electron-core interaction}} \underbrace{+\frac{e^2}{2}\sum_{i=1}^{N}\sum_{j\neq i}^{N}\frac{1}{|r_i - r_j|}}_{\text{electron-electron interaction}}, \tag{2.77}$$

where $\hbar$ is the reduced Planck constant, m_e is the electron mass, e is the elementary charge, R_I are the coordinates of the nuclei and r_i are the electron coordinates. The basis of DFT are the two Hohenberg-Kohn-theorems:[268]

- First Theorem: "For any system of interacting particles in an external potential $V_{ext}(\mathbf{r})$, the potential $V_{ext}(\mathbf{r})$ is determined uniquely, except for a constant, by the ground state particle density $n_0(\mathbf{r})$." (p.122, Ref. 163)
- Second Theorem "A universal functional for the energy $E[n]$ in terms of the density $n(r)$ can be defined, valid for any external potential $V_{ext}(\mathbf{r})$. For any particular $V_{ext}(\mathbf{r})$, the exact ground state energy of the system is the global minimum value of this functional, and the density $n(r)$ that minimizes the functional is the exact ground state density $n_0(r)$." (p.122, Ref. 163)

Unfortunately, this universal functional of the electron density is unknown. To get a proper approximation of this functional the energy contributions from Equation 2.77 have been rewritten by Kohn-Sham in the form of this functional,[164,269]

$$E_{KS}[n] = T[n] + \int n(\vec{r}) V_{ext}(\vec{r}) d\vec{r} + \frac{1}{2} \int \int \frac{n(\vec{r}) n(\vec{r}')}{|\vec{r} - \vec{r}'|} d\vec{r} d\vec{r}' + E_{XC}[n], \tag{2.78}$$

where $T[n]$ is the kinetic energy of a system of non-interacting electrons and E_{XC} is the exchange-correlation energy. The kinetic energy of the non-interacting electron system is given by,[164]

$$T[n] = -\frac{\hbar^2}{m_e} \sum_{i=1}^{N/2} \langle \phi_i | \nabla^2 | \phi_i \rangle, \tag{2.79}$$

where ϕ_i are orbitals of non-interacting particles, which add up to the electron density by,[164]

$$n(\vec{r}) = 2 \sum_{i}^{N/2} |\phi_i(\vec{r})|^2. \tag{2.80}$$

Of course, this kinetic energy is only an approximation since the true kinetic energy would be one of interacting particles. However, the missing correlation terms should be caught by the exchange-correlation functional. There are different models for approximating the exchange-correlation energy. The simplest case is the LDA, which is based on a homogenous electron gas. In this approximation it is assumed that the exchange-correlation energy just depends on the local electron density. The exchange part of the functional can be calculated exactly. Moreover, for the correlation part accurate fits to quantum Monte Carlo results are available.[164,270,271] In addition to the LDA functional, there are also GGA functionals. These include next to the density, also gradient terms of the electron density. Most notably, the PBE functional is a GGA functional.[272] Modified version of this functional have been published, e.g. PBEsol, which provides an improved description of lattice parameters compare to PBE.[273] By employing higher order derivatives or using the kinetic energy density meta-GGAs include additional

semi-local information.[164] A very successfully and only recently published meta-GGA is the strongly constrained and appropriately normed (SCAN) exchange-correlation functional.[274] This functional satisfies the 17 known constraints that a meta-GGA can fulfill and has shown to be a significant improved in the description of formation energies compared to PBE.[275]

In our calculations, we used the Vienna Ab initio simulation package (VASP)[276,277] with the projector augmented-wave method,[278,279] an energy cutoff of 900 eV and a k-spacing of 0.23 $Å^{-1}$. Moreover, we used the SCAN exchange-correlation functional[274] for all calculations.

2.10 Workflows

In this work, we use a comprehensive amount of data analysis and data processing scripts, which have been partially mentioned already. The most common packages used in these workflows are the `ase`[280], `numpy`,[281] `scipy`[282] and `matplotlib` package.[283] Moreover, in several cases we used the `pymatgen`[284] package and also the `ovito`[194] python interface was extensively used. Visualization was in general performed using `ovito`.

2.11 Research data

Research data created during this work was published in the `zenodo`[285,286] and `tudatalib`[287] repositories.

Training data generation and potential fitting 3

This chapter is based on the following two publications:

Erhard, L.C., Rohrer, J., Albe, K., Deringer, V. *A machine-learned interatomic potential for silica and its relation to empirical models.* npj Computational Materials 8, 90 (2022). https://doi.org/10.1038/s41524-022-00768-w,[137]

and

Erhard, L.C., Rohrer, J., Albe, K., Deringer, V. *Modelling atomic and nanoscale structure in the silicon–oxygen system through active machine learning.* Nature Communications 15, 1927 (2024). https://doi.org/10.1038/s41467-024-45840-9.[138]

In both publications all calculations have been performed by myself. Parts of the work for Ref. 137 have been performed during the time of my master thesis.

The training database is the core element of all machine learning interatomic potentials (MLIP). Everything the MLIP can do is based on this training database. At the same time, the training database limits the capabilities of the MLIP. Any part of configurational space that is not covered by the training database may not be reliably reproduced by the MLIP. During the time of this dissertation, we published two MLIPs for silica. First, we presented a Gaussian approximation potential (GAP) that was made only for pure bulk SiO_2. Later, we switched to moment tensor potentials (MTP) and atomic cluster expansion (ACE) potentials for performance reasons. The second database we released was an extension of the first, including high-pressure silica structures, silica surfaces, and silicon-silica interfaces. In the following, we will describe the database generation and the potential fitting in detail for both cases.

3.1 Training database generation for bulk SiO_2

Figure 3.1 illustrates the process of generating the training database. We start with some initial structures, in particular crystalline structures, dimers, amorphous and liquid structures taken from melt–quench simulations using a classical interatomic

potential.[109] These structures are evaluated by density functional theory (DFT) single-point calculations and then used to fit an initial GAP. This GAP is used in melt-quench simulations to generate new amorphous and liquid structures which are added to the training database. For these structures again DFT forces and energies are evaluated and the GAP is refitted. This process is repeated iteratively and referred to as 'batch' learning since all these structures are added to the database without further filtering.

Constructing a database comes, however, with some challenges. One challenge is choosing an appropriate exchange-correlation functional. Initially, we used the PBEsol functional, but later we recalculated the whole database with the strongly constrained and appropriately normed (SCAN) exchange-correlation functional. The SCAN functional provides significantly better agreement with the experimental standard enthalpies of formation than the PBEsol and other functionals, such as the Perdew-Burke-Ernzerhof (PBE) functional and the local density approximation (LDA) functional. However, it is also computationally more demanding.

Another problem is the choice of structures to be added to the database. In general, unfavorable structures must be added to the training database. This prevents the potential from later entering this region of configurational space. However, if there are structures with very high energies and forces they can also make the fit of the low-energy parts much worse. In the fitting process the algorithm tries to accurately reproduce the forces and energies of these high energy structures. Since the algorithm has limited flexibility, fitting high forces/energies will degrade the description of the much more important low energy state. Of course, in some limits these cases can be handled by proper weighting and regularization during the fitting process. These weight factors are later given for ACE and GAP. Nevertheless, we have excluded all structures with force components above 40 eV/Å during our training process.

3.1.1 Crystalline structures

The crystalline structures added to the training database are: α-quartz,[208] coesite,[214] stishovite,[215] chabazite,[288] moganite,[210] α-cristobalite,[209] low temperature tridymite,[289] β-cristobalite,[290] β-quartz,[291] β-tridymite,[21] tridymite in the $C222_1$[292] and in the $P2_12_12_1$[293] modification. Each of these structures has been isotropically deformed 30 times with uniformly distributed strains between ±5 % and 70 times with randomly distributed strains of ±2.5% on the diagonal components and ±5% on the angular components. For the low-temperature stable structures, the latter random strain procedure was used to generate another 100 structures per structure type. In all these structures, the atoms were randomly displaced using the `ase.rattle()`[280] function, which displaces the atoms from their original positions. We also created training structures for silicon in the diamond structure using the same procedure. The main inspiration here was not to be able to describe silicon accurately, but to improve the description of silicon-silicon repulsion and many-body interactions.

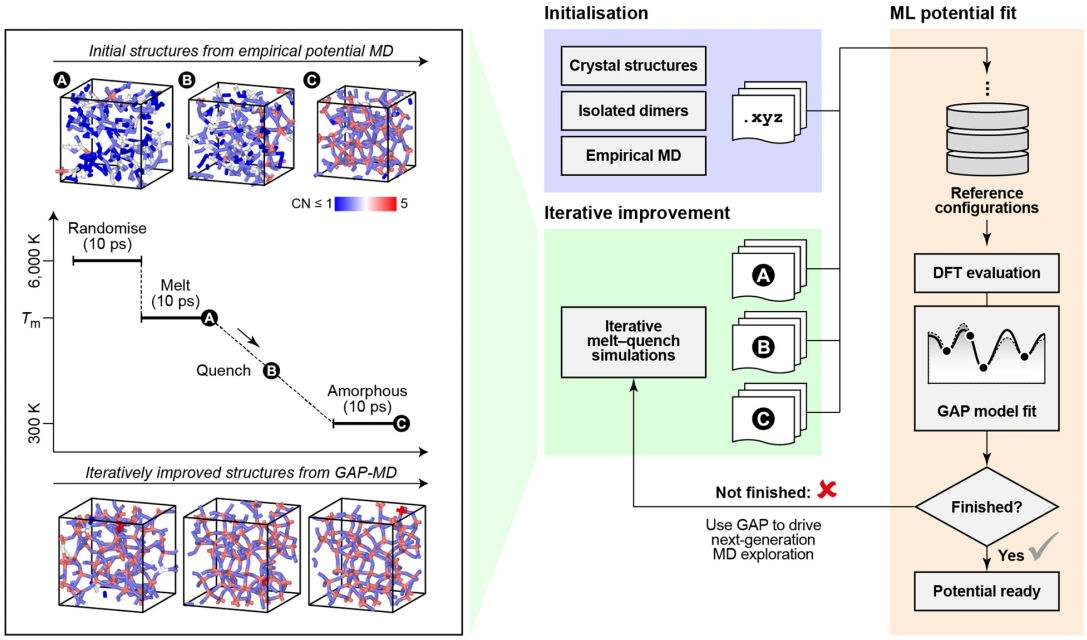

Figure 3.1: **Iterative training database extension.** An initial database was generated from rattled and deformed crystal structures, dimers and snapshots from melt-quench molecular dynamics (MD) simulations with a classical interatomic potential (*blue*). These reference configurations are then evaluated using single-point DFT calculations followed by a GAP fit to the database (*orange*). The GAP potential is then used to again perform melt–quench simulations (*green*). From these simulations shown on the left, selected snapshots (**A**, **B** and **C**) were added to the training database. After being added, they were evaluated by DFT single-point calculations and the potential was refitted. This procedure is repeated, iteratively. The bottom left shows how the quality of the amorphous structure models from the MD increases over the iterations. The melt-quench simulations were performed with different cooling rates and different input structures (see text for details). Reproduced from Ref. 137. Original figure published under the CC-BY 4.0 license (https://creativecommons.org/licenses/by/4.0/).

3.1.2 Dimers and clusters

We have added Si–Si, O–O and Si–O dimers to the database to improve the description of the repulsive behavior at small distances. We included dimers with bond lengths from 5 Å to the lowest distance, where the force is below 40 eV/Å with steps of 0.05 Å. Later, during the iterative melt-quench simulations, we observed clustering of oxygen with up to 5 atoms within the simulations. To avoid this behavior, we added scaled versions of these clusters to the database. The scaling was necessary to avoid too large forces in the training database. We assume that we did not observe similar behavior for silicon, since silicon diamond structures were part of the database.

3.1.3 Melt-quench simulations and iterative fitting

The general melt-quench procedure is shown in Figure 3.1. Since the detailed protocol changes over several iterations, we show the differences between the iterations in Table 3.1. In each iteration three structures were extracted from the MD trajectories. These correspond to the snapshots taken at points **A**, **B** and **C** (see Figure 3.1). The general melt-quench protocol is also outlined in Section 2.2. However, it has been modified in several ways. Differences to the general protocol are that the liquid equilibration time is reduced to 10 ps. Also, in several cases the liquid, quench and room temperature parts are not simulated in an NVT ensemble, but the NPT ensemble. Finally, the temperature of the liquid equilibration part of the MD was adjusted as a function of pressure (NPT) or density (NVT). For a pressure of 0 GPa (NPT) or a density of 2 g/cm^3 (NVT) a temperature of 3000 K was used, while for 10 GPa or a density of 3 g/cm^3 a temperature of 4000 K was used. In between, the temperature was scaled linearly with pressure (NPT) or density (NVT).

The first batch of amorphous and liquid structures were created using the interatomic potential by Broughton *et al.* [109] Here, we used random input structures and quench rates between 10^{10} and 10^{12} K/s. The first three iterations with GAP started from β-cristobalite input structures. We used this structure because the potential did not have too many reference data points for liquid and amorphous structures at this point. However, it was at least familiar with the crystalline β-cristobalite structure. In addition, the NVT ensemble simplified the training by removing the additional degree of freedom of the box change leading to more stable simulations. After these three iterations, we added oxygen clusters to the training set (see also Subsection 3.1.2). These oxygen clusters prevented the occurrence of unphysical clustered oxygen within the melt-quench simulations.

We then performed additional melt-quench simulations, but with random input structures. To make the dataset more consistent, we removed the melt-quench structures generated in the first iteration. Moreover, the entire database was recalculated using the SCAN exchange-correlation functional. To account for structural differences between PBEsol and SCAN, we performed another melt-quench iteration. To improve the quality of the models we reduced the quench rate for this final iteration.

3.2 Fitting of the Gaussian approximation potential

The parameters used to fit the GAP are given in Table 3.2. The δ value determines the weight of the corresponding parts of the potential, e.g. the 2-body interactions are the most important and have a weight 10 times higher than the many-body interactions. The Θ value determines the width of the Gaussians in the 2-body part of the potential. Details on the many-body parameters can be found in Section 2.8.2. In total, we use 4060 sparse points for the whole database. However, they were not automatically distributed across the database, but we assigned a certain number of sparse points to each type of configuration. Liquid structures are the structures taken from point **A** in Figure 3.1, mid-quench structures from point **B** and liquid structures from point **C**. For each of these

Table 3.1: **Melt-quench iterations.** Iterations during the iterative fitting with details regarding the melt-quench simulations. Taken from Ref. 137.

Iteration	Potential	Start	Randomization	Ensemble	Structures	Quench rate (Ks^{-1})
1	Broughton	Random	True	NVT/NPT	300	10^{10}–10^{12}
2	GAP	β-cristobalite	False	NVT	150	10^{15}
3	GAP	β-cristobalite	False	NVT	129	10^{15}
4	GAP	β-cristobalite	False	NVT	300	10^{15}
Add oxygen clusters						
5	GAP	Random	True	NVT	300	10^{15}
Remove structures from first iteration						
Recalculate database with SCAN						
6	GAP	Random	True	NVT	60	10^{13}

structure types in the database, we assign 1000 sparse points. In addition, we assign 1000 sparse points to the crystalline structures and 60 sparse points to the dimers and clusters. This generally results in a large weight on the amorphous and liquid structures, which also have a large chemical diversity.

An additional parameter in the GAP fitting is the regularization. The regularization allows certain deviations from the energies and forces in the fit without adding a large penalty to the loss function. This accounts for the uncertainty in the DFT forces and energies and enables a smoother fit. In addition, the regularization allows for some weighting of different structure, with tighter regularization parameters implying higher weights. For crystalline structures we used values of 0.005 eV/atom for the energy and 0.05 eV/Å for the forces. For the other structures we used values of 0.01 eV/atom and 0.3 eV/Å. This results in a more accurate reproduction of the crystalline phases. For more details on the general regularization we refer to Ref. 246.

3.3 Training database for the Si–O system

GAP is relatively slow compared to other MLIP approaches.[253] Therefore, we tried to use MTPs, which promise much faster evaluation times. Moreover, they have an easy-to-use active learning technique implemented (see Section 2.8.2). While we switched to this potential type, we also started to significantly extend our database. This process is illustrated in Figure 3.2a. Here, we focused on high-pressure silica, silica surfaces and mixed structures of silicon and silica. For a first extension we used small-scale MD simulations with active learning. Later, we used large-scale simulations in combination with amorphous matrix embedding, a new method to extract small-scale periodic cells from large-scale simulations. The training of the high-pressure silica, surfaces, and interfaces was performed in separate tracks, which did not exchange data between each other. Finally, all data were merged to fit an ACE potential. It should be noted, that we added some additional data also for other configurations and defects, like vacancies. Details are given below. An overview of the entire database is given in Table 3.4.

Table 3.2: **GAP parameters.** GAP 2-body and smooth overlap of atomic positions (SOAP) fitting parameters. A detailed description of individual parameters can be found in Section 2.8.2. Taken from Ref. 137.

	2-body			SOAP
	O–O	Si–Si	Si–O	
δ (eV)	4.0	4.0	4.0	0.4
Θ	1.25	2.0	2.0	
r_{cut} (Å)	5.0	5.0	5.0	5.0
r_{Δ} (Å)				1.0
σ_{at} (Å)				0.5
n_{max}				12
l_{max}				4
ζ				4
Sparsification		Uniform		CUR
N_{sparse}(amorphous)				1000
N_{sparse}(mid-quench)				1000
N_{sparse}(liquid)				1000
N_{sparse}(crystalline)				1000
N_{sparse}(cluster)				60
N_{sparse}(total)	15	15	15	4060

3.3.1 Manually prepared data

Crystalline silica and silicon

In addition to the crystalline unit cells added in Subsection 3.1.1, we have also added supercells in this part. The scheme of deformation and displacement of atoms is the same as in Subsection 3.1.1. We have added supercells of α-quartz, β-quartz, moganite, coesite, stishovite, chabazite, α-cristobalite, β-cristobalite, low temperature tridymite, β-tridymite, and tridymite in the $C222_1$ and $P2_12_12_1$ modifications. In addition, we have added hexagonal close-packed (HCP) and face-centered cubic (FCC) structures of silicon under high compression to improve the reliability of the potential at short distances.

High-pressure silica

We used the same procedure as above for unit cells and $2 \times 2 \times 2$ supercells of pyrite and seifertite.

Silica surfaces

The surfaces added to our database are given in Table 3.3. 30 structural models of each of these surface orientations were added to the database. We used different rattle amplitudes for these structures, 10 times 0.01 Å, 10 times 0.05 Å and 10 times 0.1 Å.

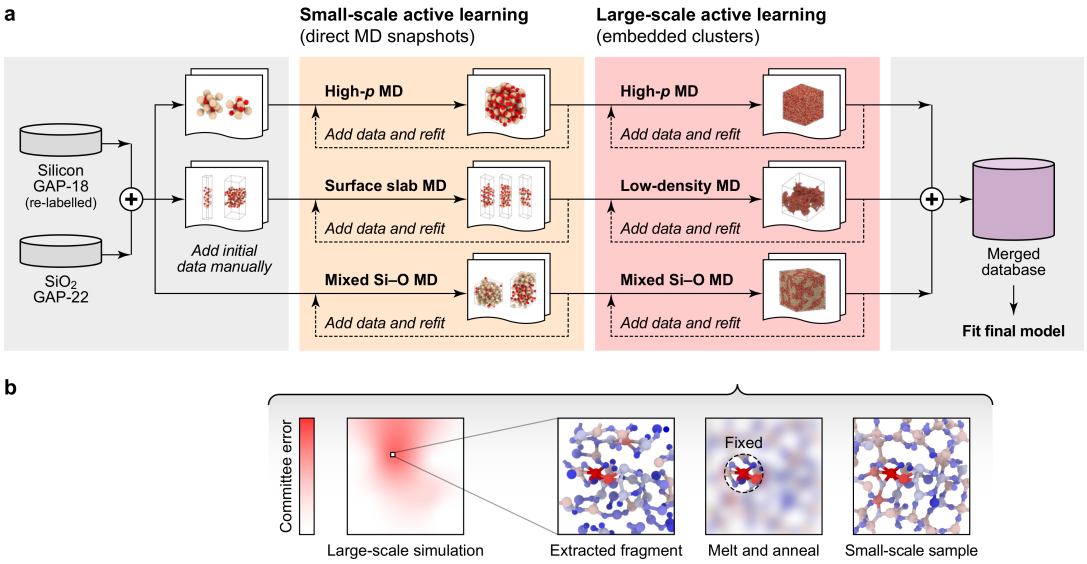

Figure 3.2: **Extending the database for surfaces, high-pressure structures and interfaces** (a) Shows the protocol we used to extend our database. We started with the GAP database (see Section 3.1) and merged it with the recalculated GAP-18 database for silicon.[294] From there, our training process was divided into three tracks. The first track considered high–pressure ("High-p") silica, the second track considered silica surfaces and the third track considered mixed Si–O_x systems of varying composition. In the first step (*gray*), manually generated high-pressure crystal structures and silica surfaces are added to their respective tracks. In the second step (*orange*), small-scale active learning is performed. This includes MD simulations of the corresponding compositions and environments, using an uncertainty indicator in each MD step to find unknown configurations (see Section 2.8.2). The third step (*red*) follows a similar approach to the second step. However, this time we perform large-cell MD simulations instead of small-cell MD simulations with cell sizes feasible for DFT calculations. From these large-scale simulations we extract small-scale cells using the approach shown in (b). We define an uncertainty for each atom (indicated by the red color bar) and then extract a small-cell box surrounding an atom with an uncertainty above a threshold. This extracted fragment has very unfavorable boundaries. However, by keeping the immediate environment of the atom of interest fixed and melting everything else, these boundaries can be energetically drastically improved. Finally, we obtain a structure with an unchanged local environment around the atom of interest embedded in an amorphous matrix. Reproduced from Ref. 138. Original figure published under the CC-BY 4.0 license (https://creativecommons.org/licenses/by/4.0/).

10 further structural models have been created by modifying surface terminations and rattling with 0.01 Å average displacement. Finally, the amorphous surface models were created using amorphous bulk structures generated by melt-quench simulations. These models were cut to create a surface.

Table 3.3: **Surface structures with various orientations.** Surface orientations of structures, which are included in the database. Taken from Ref. 138.

Polymorph	Surfaces
α-quartz	(001), (110), (100), (210)
α-cristobalite	(001), (100), (110)
low temperature tridymite	(100), (001)
β-tridymite	(001), (110), (100), (210)
β-cristobalite	(100), (110), (111)
moganite	(100), (010), (001)

Silica vacancies

Vacancies are easily generated by deleting atoms from α-quartz and amorphous silica structures. To keep charge neutrality, we only removed a stoichiometric number of atoms. This means that always one silicon cation and two oxygen anions have been removed.

Crystalline-amorphous interfaces between Si-SiO_2

We connected two crystalline bulk supercells of silicon and silica within one cell. In this cell we melted one side, while keeping the other side fixed. Interdiffusion was prevented by a repulsive wall between the silicon and the silica side.

Clusters

We performed iterative MD simulations similar to Subsection 3.1.3, starting with $[SiO]_2$ clusters and performing MD simulations with increasing temperature. In the second iteration, larger $[SiO]_3$ clusters were used, and one more dimer was added in each iteration. During the MD simulations the temperature was increased from 100 to 2000 K. The process was proceeded up to a system size of $[SiO]_{32}$ and in each iteration we performed five MD simulations, from where we extracted five snapshots.

3.3.2 Small-scale active learning

An extrapolation threshold of 1.5 and a stopping threshold of 3.0 were used in our simulations (see Section 2.8.2). We started with a series of parallel MD simulations. In each of these MD simulations, we evaluated the extrapolation grade in each time step. If the extrapolation grade exceeded the extrapolation threshold, this configuration was written to a database. At the point where the simulation reached the stopping threshold, the simulation was stopped. All extrapolated files are collected and subjected to a maxvol selection along with the current database. The most extrapolative files are recalculated with DFT and added to the database. Then the potential is reapplied, and the whole procedure starts again from the beginning. At some point, all parallel simulations ran to the end without printing any unknown structures. Then the active learning cycle is converged, and the database for that part of configurational space is completed.

Quenching of SiO_2 and SiO_x

For melt-quench simulations we used the protocol explained in Section 2.2. Input of these simulations have been different crystalline unit and supercells in the case of SiO_2. In the case of SiO_x we used stacked cells of silica and silicon polymorphs, where the composition could be adjusted by the combination of these cells.

High-pressure silica

Similarly, as before we used the protocol from Section 2.2 and varied the pressure between 0-200 GPa. Moreover, after convergences of these calculations, we performed compression simulations at random temperatures between 0 and 1000 K with a starting pressure of 0 GPa going to 200 GPa. Here, we used amorphous structures as input.

SiO_2 surfaces

The manually created surface structures from Subsection 3.3.1 are used as input for MD simulations. These simulations start from a temperature of 50 K and heat up to 3000 K. Afterwards they are cooled to 50 K again.

3.3.3 Large-scale active learning and amorphous matrix embedding

Amorphous matrix embedding

The idea of amorphous matrix embedding is shown in Figure 3.2b. We start with a large-scale simulation for which we need an atom specific uncertainty. Using MTPs, where this atom-specific uncertainty was not initially implemented, we used a committee error, which is the deviation between several MTPs trained on the same training data. The per-atom uncertainty is then given by

$$u_\alpha = \sqrt{\sum_{i \in x,y,z} \sigma(f_{\alpha,i}^{(1..N)})^2}, \tag{3.1}$$

where σ is the standard deviation, $f_{\alpha,i}^{1...N}$ is the i-th component of the force, which is acting on atom α and is calculated by the N committee members.

Based on this, we go one step further in Figure 3.2b. We can now identify atoms with a large uncertainty (typically above 1-2 eV/Å). These atoms of interest and their environments are then cut and added into smaller boxes that are DFT feasible. The size of these boxes is 13 Å plus a margin of 1 Å to prevent atoms from getting too close at the boundary. Now we keep the atom inside the cutoff radius of our interatomic potential (5 Å) fixed and anneal all atoms outside the cutoff radius up to a temperature of 2000 K to 6000 K. This allows significant rearrangement of atoms at the boundary while keeping the atoms inside the cutoff fixed and thus the immediate environment of the atom of interest identical. The final structure has boundaries with much less badly-coordinated atoms and can be used for DFT calculations.

In order to improve the usability of the algorithm, we added several other constraints to the procedure. Similar to the small-scale active learning approach, where there is an upper threshold at which the simulation stops, we also introduce an upper threshold of 5 eV/Å. This prevents too many unfavorable and too unfavorable structures from being added to the database. Furthermore, since local environments can remain very similar over several time steps, we introduce an additional criterion based on the SOAP vector calculated by *DScribe*.[295] We only added structures to the database that have similarities (see Equation 2.58) below 0.9-0.95 compared to the other added structures.

In the case of surfaces, the extraction of a cell is not as trivial as for bulk structures. First, we need to define the surface normal vector of the surface at the atom of interest i,

$$\mathbf{n}_i \approx \sum_j (\mathbf{x}_i - \mathbf{x}_j) \text{ if distance}(i,j) < \text{cutoff}, \tag{3.2}$$

where the position of atom j is given by x_j. The extracted atoms are rotated so that the normal vector is arranged in z-direction. To mimic the surface, the vacuum on both sides of the cell was extended by 5 Å in z-direction. If structures were not periodically connected in the x- and y-direction, additional vacuum layers were added in these directions.

Quenching of SiO_2 and SiO_x

The same protocols with larger supercells as in the case of the small-scale active learning have been used.

Silica surfaces

We used the standard quenching protocol from Section 2.2, however, the part under constant external pressure was replaced by a systematic straining procedure to larger volumes. This straining to larger volumes causes the generation of porous and therefore amorphous surfaces in the structures.

Vacancies

Structures of amorphous silica and quartz, both containing around 65,000 atoms, are heated from room temperature to 3000 K and back to room temperature. Each of these structures contained 150 randomly distributed vacancies, e.g. 50 silicon vacancies and 100 oxygen vacancies.

High-pressure silica

As for the small-scale active learning we compressed structures up to 200 GPa at random temperatures between 0 and 1000 K. Structures sizes of 65,000 atoms have been used.

Clusters

10,000 SiO molecules have been placed within a box. The box size was chosen that it corresponds to a density of 0.011 g/cm^3. Afterwards the structure was compressed at a temperature of 1,400 K up to a density of ≈ 2 g/cm^3.

Table 3.4: **Overview over the final database composition** with detailed breakdown in different structure types. The SiO_2-GAP part are the structures created within Section 3.1. The Si-GAP structures are taken from Ref. 294. Structures, which have been collected by active learning are indicated and the corresponding active learning approach is given (see also discussion in the text). The final fitting weights for the ACE potential is are also shown (see also Section 3.4). Taken from Ref. 138.

Configuration type	Composition	Reference	Active learning	Structures	Atoms	Weights
crystalline	SiO_2	SiO_2 GAP + this work	—	2,620	281,820	100
amorphous	SiO_2	SiO_2 GAP	—	313	60,096	1
half-quenched	SiO_2	SiO_2 GAP	—	311	59,712	1
liquid	SiO_2	SiO_2 GAP	—	313	60,096	1
crystalline (main)	Si	Si GAP	—	1,257	38,680	100
amorphous	Si	Si GAP	—	159	29,632	1
liquid	Si	Si GAP	—	76	5,312	1
surfaces	Si	Si GAP	—	214	22,066	1
defects	Si	Si GAP	—	423	74,548	1
various (e.g. high energy crystal)	Si	Si GAP + this work	—	505	2,556	1
quenched	SiO_2	this work	small-scale	385	19,008	1
quenched	SiO_2	this work	large-scale	417	53,208	1
vacancies	SiO_2	this work	—	278	56,520	1
vacancies	SiO_2	this work	large-scale	780	121,836	1
high-pressure crystals	SiO_2	this work	—	400	19,080	1
high-pressure amorphous	SiO_2	this work	small-scale	166	31,872	1
high-pressure amorphous	SiO_2	this work	large-scale	407	120,246	1
surfaces	SiO_2	this work	—	603	48,477	1
surfaces	SiO_2	this work	small-scale	28	1872	1
surfaces	SiO_2	this work	large-scale	167	8466	1
crystalline-amorphous interfaces	$Si+SiO_2$	this work	—	457	31036	1
quenched	$Si+SiO_2$	this work	small-scale	457	31036	1
quenched	$Si+SiO_2$	this work	large-scale	430	71821	1
clusters (dimers, larger SiO clusters)	various	SiO_2 GAP + this work	—/large-scale	611	24,900	1

3.4 Fitting of the ACE potential

Fitting a MTP to the final structurally rich database was difficult due to the insufficient accuracy achieved by this approach (see Table 3.4). However, we found that the ACE formalism allows for more flexibility than the MTPs. By introducing systematic nonlinearities, we can dramatically increase the ability to fit such a complex database. While the linear ACE is given by Equation 2.74, the Finnis-Sinclair ACE is given by,

$$V_i = \phi_i^{(1)} + \sqrt{\phi_i^{(2)}}. \tag{3.3}$$

However, we have extended this nonlinearity to the following form,

$$V_i = \phi_i^{(1)} + \sqrt{\phi_i^{(2)}} + \sum_j \left(\phi_i^{(j)}\right)^{f_j}, \tag{3.4}$$

Table 3.5: **Comparison of the GAP model with various ACE models.** Energy (ΔE) and force (ΔF) root mean square error (RMSE) are given in the columns for the GAP model (see Section 3.2) and three different ACE models (see text for details). The units are given in meV/atom and eV/Å for energies and forces. Amorphous structures are indicated by 'a' and the Carré, Horbach, Ispas, Kob (CHIK),[108] GAP and ACE structures are generated by melt-quench MD with their corresponding potentials. Taken from Ref. 138.

	SiO_2-GAP		Si–O ACE models					
			Linear ($N=1$)		F–S ($N=2$)		Complex ($N=8$)	
	ΔE	ΔF	ΔE	ΔF	ΔE	ΔF	ΔE	ΔF
SiO_2 crystals	1.0	0.08	0.8	0.07	1.1	0.06	0.9	0.05
a-SiO_2 (CHIK-MD)	3.7	0.19	4.1	0.27	5.1	0.27	2.2	0.19
a-SiO_2 (GAP-MD)	1.1	0.10	10.3	0.13	9.8	0.12	4.6	0.10
a-SiO_2 (ACE-MD)	4.0	0.17	8.0	0.28	7.4	0.26	3.2	0.18
a-SiO_2 surfaces	14.9	0.18	21.4	0.21	18.0	0.18	4.7	0.16
a-Si[a]	> 1,600	> 3.2	115.8	0.38	53.9	0.34	51.5	0.26
a-SiO_x[a]	> 4,200	> 3.5	37.8	0.71	35.0	0.64	38.0	0.43
high-p a-SiO_2[a]	122.7	0.87	15.1	0.48	5.6	0.36	4.6	0.24

[a] Structural models generated using ACE-MD.

where $f_j \in \{1/8, 1/4, 3/8, 3/4, 7/8, 2\}$. Thus, in contrast to one embedding in the case of the linear ACE and two embeddings in the case of the Finnis-Sinclair type ACE, we used a total of eight embeddings. We refer to this ACE as the 'complex' ACE. An overview of the errors for a number of test sets is shown in Table 3.5. We used a total of 600 basis functions for each of the embeddings. In general, only the complex ACE achieves the same errors as the GAP, for cases where the GAP has training data covering that configurational space. However, the linear and Finnis-Sinclair ACE often perform worse than the complex ACE and GAP. Only for parts of configurational space that were not part of the training database do all ACE potentials outperform the GAP. Interestingly, there is one exception, since the GAP was not trained on surfaces, but still outperforms the linear and Finnis-Sinclair ACE.

Moreover, the similar or higher accuracy of the complex ACE comes with an additional advantage in execution time. As shown in Table 3.6, it is only slightly slower than the linear and Finnis-Sinclair ACE. At the same time, it is more than 100 times faster than the GAP. This is particularly remarkable since it can be used in an even larger part of configurational space.

To achieve high accuracy for the important crystalline structures, we set the weight for these structures higher compared to the others (see Table 3.4).

3.5 Summary

We developed a database for a GAP potential for amorphous and crystalline silica. Building on this we extended the database by active learning to high-pressure silica, silica surfaces, and interfaces between silicon and silica. For active learning, we first used standard small-cell approaches and later introduced amorphous matrix embedding,

Table 3.6: **Speed comparison of ACE and GAP.** The timings obtained here, have been determined for cells of 192 atoms over 100 time steps.

	GAP (Ref. 137)	ACE (This work)		
		Linear ($N = 1$)	F–S ($N = 2$)	Complex ($N = 8$)
Timing (μs/(time step · atom))	11,037	61	62	70
Speed-up to GAP	1	181	178	158

which allows small cells to be extracted from large-scale simulations. This approach was used in large-scale active learning simulations. Finally, we fitted an 'complex' ACE potential, which is able to describe the complex structure space of the database, while restoring still the same accuracy as the GAP for crystalline and amorphous silica. Moreover, the newly developed ACE potential is more than 100 times faster than the former GAP and should therefore be preferred. All structure databases labeled with DFT energies and forces and the corresponding potential files can be found in the zenodo repository.[285,286]

Thermodynamics and structural aspects of silica

4

This chapter is based on the following two publications:

Erhard, L.C., Rohrer, J., Albe, K., Deringer, V. *A machine-learned interatomic potential for silica and its relation to empirical models.* npj Computational Materials 8, 90 (2022). https://doi.org/10.1038/s41524-022-00768-w,[137]

and

Erhard, L.C., Rohrer, J., Albe, K., Deringer, V. *Modelling atomic and nanoscale structure in the silicon–oxygen system through active machine learning.* Nature Communications 15, 1927 (2024). https://doi.org/10.1038/s41467-024-45840-9.[138]

In both publications all calculations have been performed by myself. Parts of the work for Ref. 137 has been performed during the time of my master thesis.

The goal of this chapter is to analyze whether machine learning interatomic potentials (MLIP) are able to capture the thermodynamics of the polymorphs of crystalline silica and the energetics and structural aspects of amorphous silica. We will start with energy-volume curves, which allow to compare the stability of the phases. From there we will have a look at the phonon density of states, that allows to calculate the vibrational free energies. This finally leads to a phase diagram calculated using the quasi-harmonic approximation with frozen phonons (see also Subsection 2.4.1). Here, we also make a comparison with already existing classical interatomic potentials. To include anharmonic vibrations, we perform further high temperature phase diagram calculations using thermodynamic integration (see also Subsection 2.4.2). Note that in this chapter we focus on the phase stability below 10 GPa. For very high pressure calculations, please refer to Chapter 5. Finally, we have looked into the energetics of amorphous structures and their structure factor for structure models generated by different interatomic potentials.

Most of the simulations in this part were performed with the Gaussian approximation potential (GAP). For the thermodynamic integration we used the atomic cluster expansion (ACE) potential for performance reasons.

4.1 Elastic properties and energy–volume curves of silica polymorphs

Accurate reproduction of the elastic properties of a material is an essential feature of interatomic potentials. In Figure 4.1a we show energy–volume curves of several silica polymorphs calculated with DFT using the SCAN exchange-correlation functional. Moreover, we show the GAP result for comparison. The GAP agrees very well with the DFT results. This is indeed a first indication that MLIPs are able to reproduce the structural richness and corresponding phase transitions between different silica phases.

Corresponding to the good agreement between the DFT and GAP energy–volume curves, the bulk moduli and equilibrium volumes are also reproduced well. These are shown in Table 4.1. Besides the fit with the DFT, the agreement with the experiment is even more crucial. However, the abilities of the MLIP are limited here because it is fitted to DFT data. Therefore, the choice of the exchange-correlation functional is essential, and the match between the results of the exchange-correlation functional and the experiment is of great importance. Indeed, SCAN seems to be a good choice with

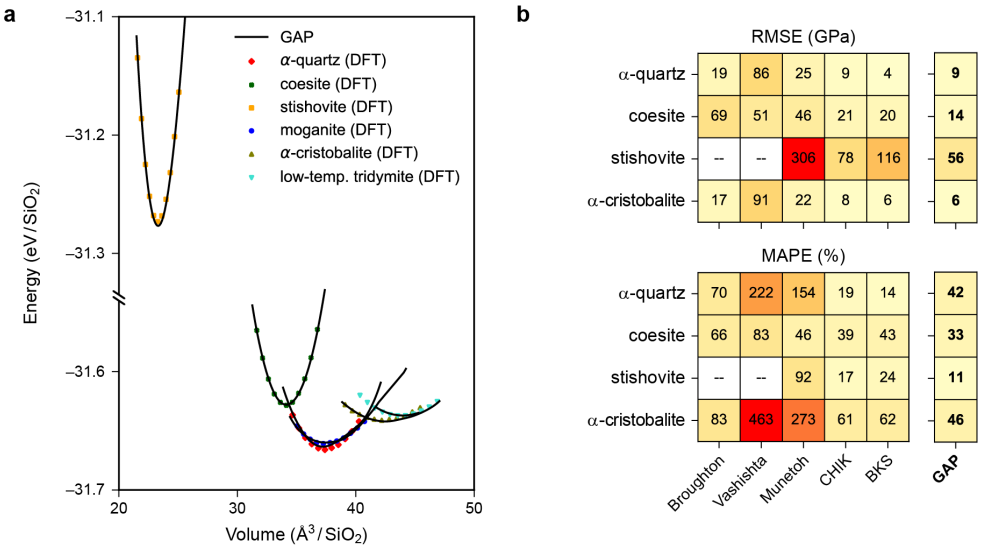

Figure 4.1: **Energy–volume curves and elastic constants.** (a) Strongly constrained and appropriately normed (SCAN)-density functional theory (DFT) (colored symbols) and GAP (solid lines) energy–volume curves for different silica polymorphs. In the case of low temperature tridymite, only the GAP stability region is shown, which is reduced compared to the DFT stability region. (b) Errors (root mean square error (RMSE) and mean absolute percentage error (MAPE)) of the predicted elastic constants of several interatomic potentials compared to experimental values.[296–299] Two potentials, the Vashishta and Broughton potentials, predict that the stishovite structure is unstable, and therefore no elastic constants could be determined. The color coding from yellow to red indicates the size of the error. Very large percentage errors (>100%) are caused by large deviations from small absolute values. Reproduced from Ref. 137. Original figure published under the CC-BY 4.0 license (https://creativecommons.org/licenses/by/4.0/).

Table 4.1: **Bulk moduli and ground–state volumes.** The ground–state (T=0 K) volumes (V) of the corresponding polymorphs and additionally the bulk moduli (K) are shown for the GAP and DFT.[a] If there was experimental data available this is shown additionally. Taken from Ref. 137.

	K (GPa)			V (Å^3/SiO$_2$)		
	Expt.	SCAN	GAP	Expt.	SCAN	GAP
α-quartz	37.7[300]	39.7	36.6	37.8[301]	37.4	37.2
coesite	94.0[302]	106.8	106.4	33.9[214]	34.1	34.1
stishovite	295.0[302]	300.1	307.5	22.9[215]	23.3	23.3
chabazite	—	42.3	50.8	64.9[288]	65.4	65.7
α-cristobalite	16.4[297]	15.5	13.5	42.8[209]	42.3	42.5
moganite	32.2[303]	26.8	25.2	38.1[210]	37.4	37.5
low-tridymite	—	19.0	18.7	44.0[289]	43.8	44.0

[a] Values have been determined using a Birch–Murnaghan fit for hydrostatically deformed cells (see Section 2.4).

respect to the bulk moduli, as can be seen in Table 4.1. Moreover, the ground–state volumes are in even better agreement with the experiment than the bulk moduli.

Even more challenging is the reproduction of experimental elastic constants. As with the bulk moduli, the MLIP is limited by the training data, and since the DFT elastic constants are rarely in perfect agreement with the corresponding experimental values, the MLIP faces additional challenges. Figure 4.1b shows the errors of several interatomic potentials in calculating the elastic constants for several silica polymorphs. It can be seen that the Vashishta and the Munetoh potentials, both, do not perform well here. The Broughton potential shows reasonably well predictions for α-quartz, coesite, and α-cristobalite, but fails to describe stishovite as a stable phase. Finally, the Carré, Horbach, Ispas, Kob (CHIK) and van Beest, Kramer, van Santen (BKS) potentials do fairly well for all phases. However, the GAP performs best for almost all phase. In this sense it is surprising since classical interatomic potentials (CIP) are often fitted to elastic constants. Because GAP is only fitted to DFT data, it supports the quality of the underlying SCAN data. Even for structures with comparatively high RMSEs, GAP provides a reasonably accurate description, since the corresponding MAPEs are low. This is due to the high absolute values of the elastic constants of stishovite and supports the combination of MAPE and RMSE in the analysis of such properties.

4.2 Phonon spectrum of α-quartz

Accurate forces are critical for reproducing vibrational properties such as phonon spectra and temperature-dependent phase diagrams. Figure 4.2 shows the phonon dispersion of α-quartz calculated using the GAP and the Broughton, Munetoh, Vashishta, CHIK and

BKS potentials. All potentials are in good qualitative agreement with the experiment. However, for the Broughton and Vashishta potentials it appears that the phonon dispersion is scaled by a constant factor. In the case of the Munetoh potential the overall agreement is good, but at the K point the acoustic modes almost overlap, in contrast to the experimental measurement. For the BKS potential, the higher modes are shifted to higher frequencies compared to the experiment. Among the CIPs, the CHIK potential has the best agreement with experiment. However, the agreement of the GAP is even better, with only a small deviation in the high frequency phonon branch at the Γ point.

4.2.1 Phase diagrams of silica

Based on the phonon density of states the vibrational entropy can be determined (see Subsection 2.4.1). Using this thermal vibrational entropy, the temperature dependence of the phase stabilities can be calculated. These phase stabilities can be used to construct the phase transition lines in a phase diagram. We used the quasi-harmonic approximation to obtain an additional pressure dependence of the stability fields. The resulting phase diagram for a number of structures is shown in Figure 4.3. We have analyzed the phase stability for α-quartz, coesite and stishovite using the GAP and the Broughton, Munetoh, Vashishta, CHIK and BKS potentials.

The first observation is that only the GAP and the Munetoh potential are able to predict the phase stability field of all three polymorphs in qualitative good agreement with experiment. Also, despite these and the Broughton potential, all other potentials do not predict α-quartz to be the stable phase at ambient conditions. In the case of the Vashishta potential, only coesite is stable over the entire stability range. A similar behavior is shown for the CHIK potential, where stishovite starts to become stable only at pressure of 8 GPa. For the BKS potential the situation is even worse, since stishovite is stable over almost the entire pressure range and coesite becomes the stable phase only at low pressures and high temperatures. In fact, the phase diagram of the BKS potential has been analyzed in previous studies and shows that coesite and α-quartz become stable only at negative pressures.[148] Compared to the other potentials, the Munetoh potential performs much better here. Indeed, the coesite–stishovite boundary is well described, and only the α-quartz–coesite boundary is a bit off. However, the GAP again shows an excellent quantitative description of the phase transition, which again supports the quality of the underlying DFT data. We note that other exchange-correlation functionals such as the local density approximation (LDA) significantly underestimate the transition pressure.[229]

One problem with the phase diagram in Figure 4.3 is that the temperature range shown is limited because the quasi-harmonic approximation is only valid at low temperatures. At the same time, it cannot be used to determine the stability of temperature-stabilizes structures such as β-quartz, β-tridymite, or β-cristobalite. In these structures, atoms are not placed in minimum energy positions, which leads to imaginary phonon modes in the harmonic calculations. To overcome these limitations, we used thermodynamic integration (see Subsection 2.4.2) to calculate a high temperature phase diagram. This phase diagram is shown in Figure 4.4. Details of the calculations can be found in

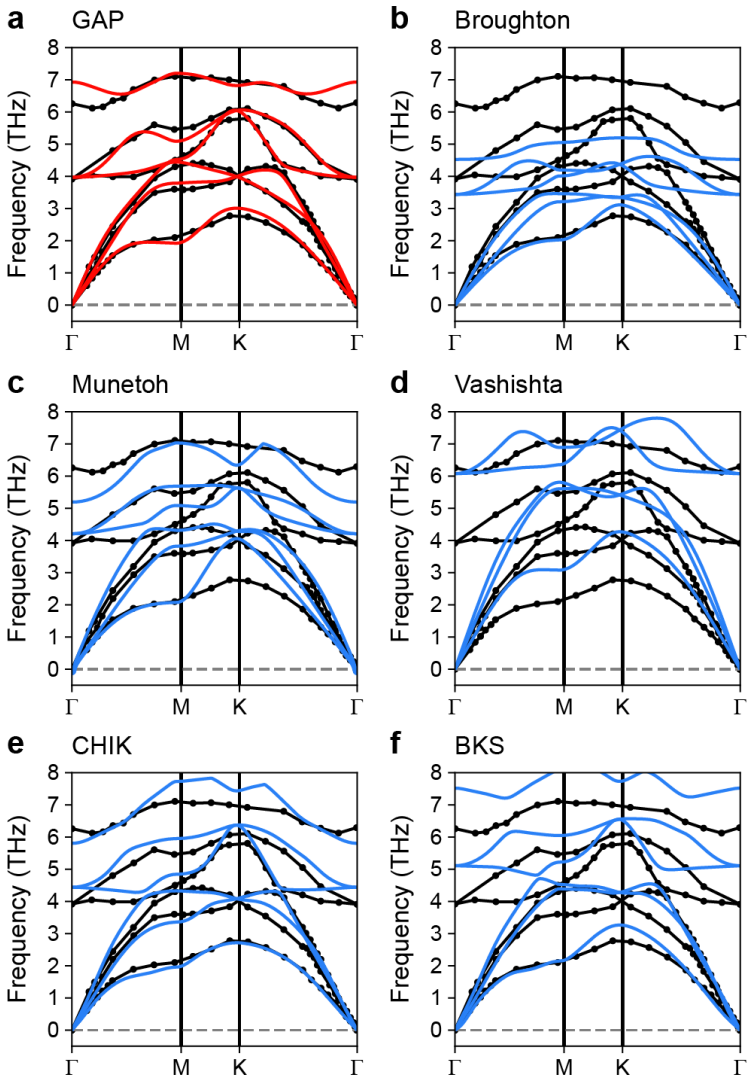

Figure 4.2: **Phonon spectra of α-quartz.** The Γ → M → K → Γ phonon dispersion of α-quartz computed by (a) GAP, (b) the Broughton potential, (c) the Munetoh potential, (d) the Vashishta potential, (e) the CHIK potential and (f) the BKS potential. The black background lines are corresponding experimental data.[304] Reproduced from Ref. 137. Original figure published under the CC-BY 4.0 license (https://creativecommons.org/licenses/by/4.0/).

Subsection 2.4.3. The ACE potential was used for the calculations because calculations with the GAP would not have been feasible with the desired accuracy. The qualitative agreement between the ACE prediction and the experiment is impressive. In particular, the boundaries between α-quartz, β-quartz and coesite are well reproduced. Larger deviations occur in the stability fields of β-cristobalite and tridymite. Compared to experimental observations, these fields are much larger and the melting point is significantly overestimated.

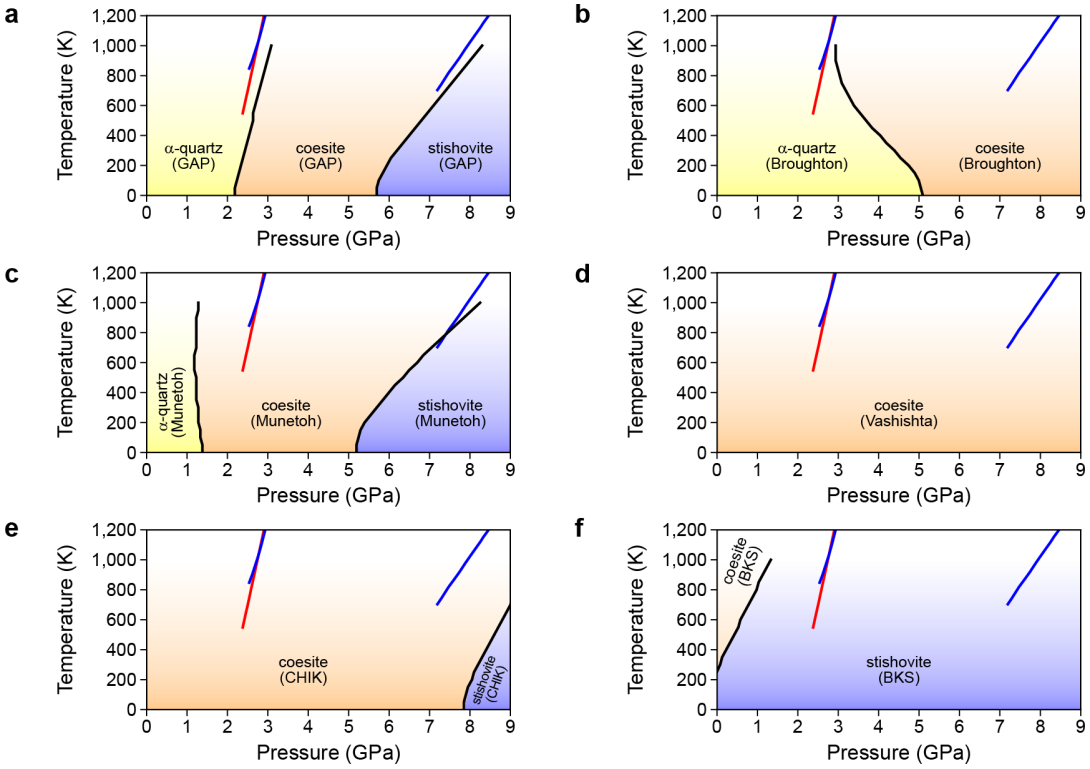

Figure 4.3: **Low-temperature phase diagram of silica.** Phase diagrams calculated for α-quartz, coesite and stishovite using the quasi-harmonic approximation. We used the (a) GAP and the (b) Broughton, (c) Munetoh, (d) Vashishta, (e) CHIK, and (f) BKS potentials. The experimental transition lines are indicated by the red[30] and blue[31] lines, respectively. Since the quasi-harmonic approximation is only valid for lower temperatures, we only show results up to 1,000 K. Reproduced from Ref. 137. Original figure published under the CC-BY 4.0 license (https://creativecommons.org/licenses/by/4.0/).

To study these deviations in detail, we slightly modified the phase diagram. We reduced the stability of cristobalite and tridymite by adding a penalty term of 5 meV/atom to their Gibbs free energy. The resulting phase diagram is shown in Figure 4.5a. It can be seen that the new phase diagram is already much closer to the experimental phase diagram than before. This indicates that the SCAN exchange-correlation functional tends to overestimate the stability of both phases. The error of the MLIP compared to the DFT is about 1 meV/atom, which is too small to explain these deviations.

We note that the phase diagram is quite error sensitive. Especially in the case of tridymite and cristobalite small deviations of 0.1 meV/atom can lead to deviations of the transition temperatures of more than 100 K. The error of the thermodynamic integration as well as the error of the machine-learning potential fit compared to the DFT data are higher or similar to this value of 0.1 meV/atom. This indicates a high uncertainty for this phase transition line. In contrast, the transition lines between quartz, the melt

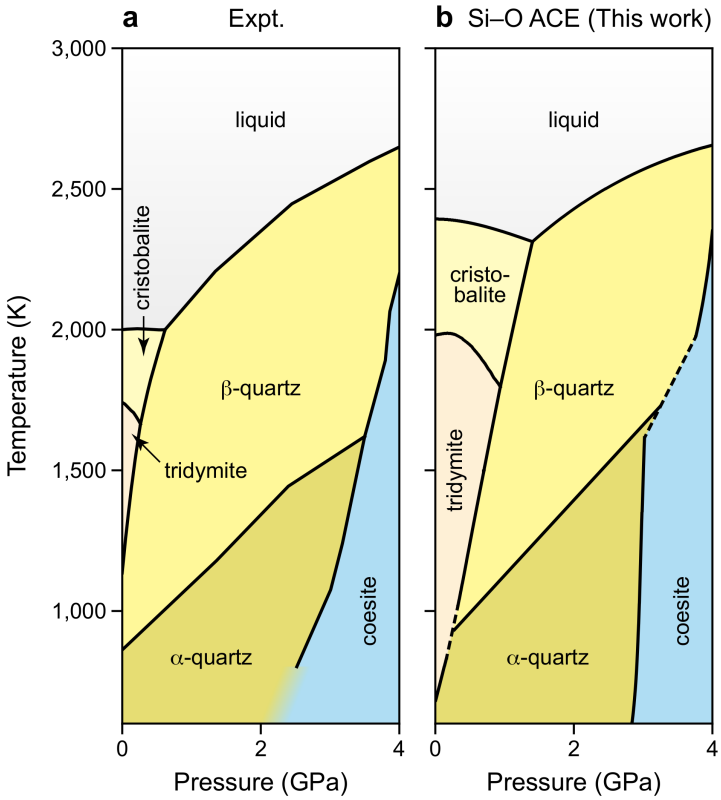

Figure 4.4: **High temperature phase diagram of silica.** (a) Calculated phase diagram from experimental data of silica taken from literature.[17] (b) The phase diagram of silica determined using thermodynamic integration with the ACE potential. Reproduced from Ref. 138. Original figure published under the CC-BY 4.0 license (https://creativecommons.org/licenses/by/4.0/).

and coesite are slightly less sensitive (see Figure 4.5d-f), but still have a not negligible uncertainty.

4.3 Amorphous silica by melt-quench simulations

In this part, we will go beyond the crystalline phases and have a look at the description of the amorphous phase. We have generated amorphous structure models with different interatomic potentials and compared their structure factor with experiment. The general melt-quench protocol is given in Section 2.2. The resulting X-ray structure factors are shown in Figure 4.6a and Figure 4.6b. Although all structure factors of the models reproduce the general form of the experimental structure factor, there are significant deviations in the details. The Munetoh potential generally gives the worst agreement with the experimental structure factor. The first sharp diffraction peak (FSDP) is significantly underestimated, and the second peak is also not well reproduced. The

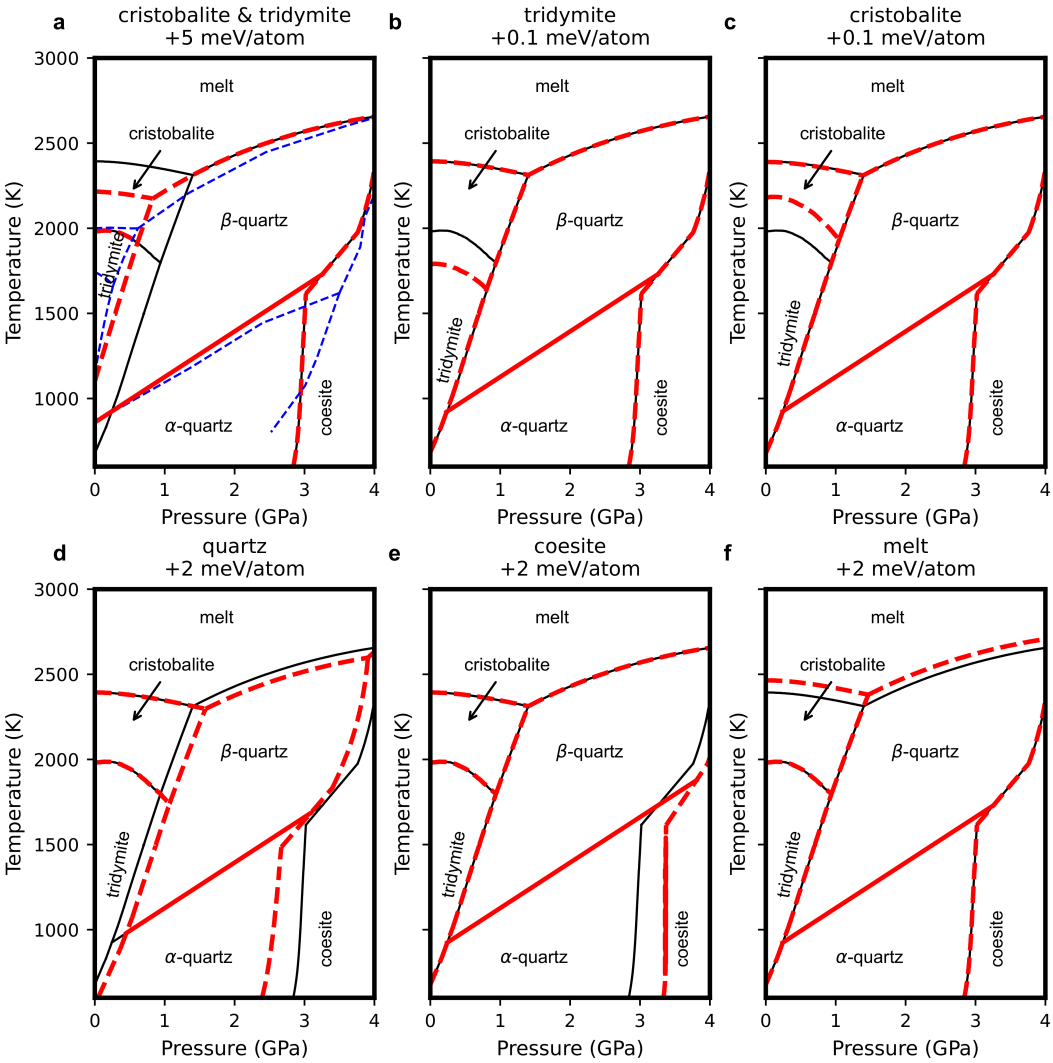

Figure 4.5: **Phase diagram sensitivity.** Modified phase diagrams using energy penalties on different phases. (a) Phase diagram assuming that cristobalite and tridymite are both less favorable (red) compared with the unmodified phase diagram (black) and the experimental[17] one (blue). (b)-(f) Phase diagrams for different destabilized phases (red) compared to the original phase diagram. Note the lower energy penalty for cristobalite and tridymite compared to the other phases. Reproduced from Ref. 138. Original figure published under the CC-BY 4.0 license (https://creativecommons.org/licenses/by/4.0/).

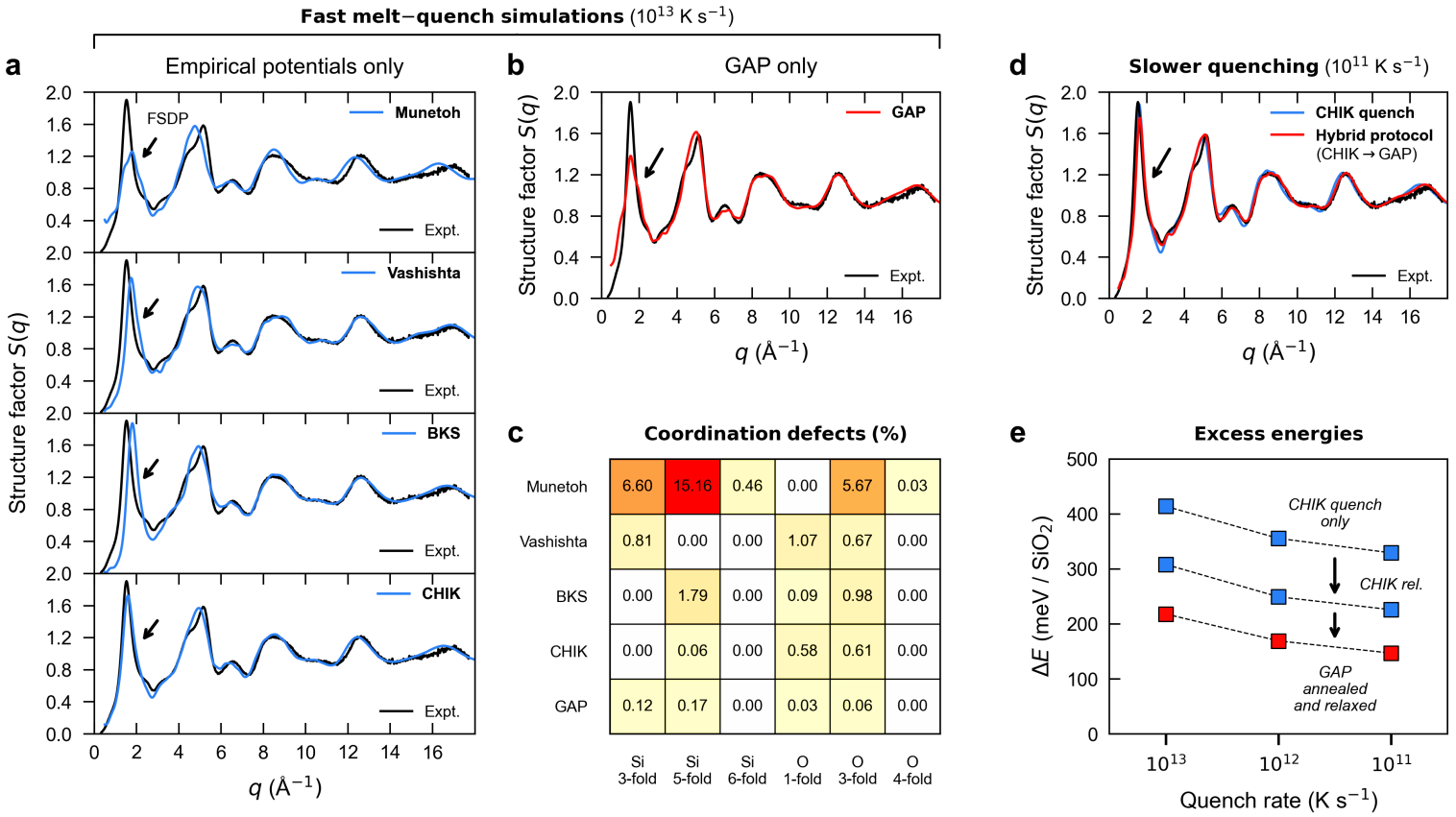

Figure 4.6: **Amorphous silica.** Structure models for amorphous silica have been generated by melt-quench simulations (quench rate: 10^{13} K/s) using various potentials. (a) X-ray structure factors of melt-quenched amorphous silica at 300 K generated by different CIPs (blue lines) compared to experimental data (Ref. 305). (b) X-ray structure factor of a model generated by the GAP (red line) with experimental data. (c) Amount of coordination defects within the amorphous structures generated by the different interatomic potentials. Wrongly-coordinated silicon atoms have more or less than four bonds, while wrongly-coordinated oxygen-atoms have more or less than two bonds. A bond cutoff of 2 Å was used. (d) As in (a) and (b) X-ray structure factor of amorphous models, but this time of an amorphous model generated with a quench rate of 10^{11} K/s using the CHIK potential with subsequent equilibration at 300 K using the GAP ('hybrid protocol'). (e) Energies of the amorphous models referenced to α-quartz depending on the quench-rate before and after CHIK and GAP relaxation. Reproduced from Ref. 137 with a slight modification of the structure factor data due to inclusion of the q dependence of the atomic form factor. Original figure published under the CC-BY 4.0 license (https://creativecommons.org/licenses/by/4.0/).

Table 4.2: **Excess energies of amorphous silica.** Models have been generated by various interatomic potentials. The excess energy is defined by $\Delta E = E_{\text{amo}} - E_{\alpha\text{-quartz}}$ as mean and standard deviation of five simulations. The amorphous energy E_{amo} given by single-point energies (by SCAN, GAP or CHIK) of the quenched and relaxed state using the respective models. In case of the re-relaxed energies, the models have been additionally relaxed using GAP or the CHIK potential.

	ΔE (meV/SiO_2)				
	single-point evaluation			re-relaxed	
	SCAN	GAP	CHIK	GAP	CHIK
Munetoh quench	1,334 ± 79	1,314 ± 74	1,376 ± 30	657 ± 25	678 ± 30
Vashishta quench	310 ± 97	302 ± 82	423 ± 32	248 ± 65	315 ± 32
BKS quench	361 ± 19	364 ± 18	385 ± 15	256 ± 16	315 ± 15
CHIK quench	311 ± 20	317 ± 14	321 ± 16	226 ± 12	(321 ± 16)[a]
GAP quench	235 ± 15	234 ± 16	515 ± 15	(234 ± 16)[a]	399 ± 15

[a] Relaxations have been performed using the same potential as before, therefore, the 'single-point' and 're-relaxed' values are identical.

Vashishta potential and the BKS potential both give a significantly better description of the structure factor than the Munetoh potential. The FSDP as well as the general shape is better described. Although the height of the FSDP is in much better agreement with experiment, the position of the peak is slightly shifted to higher q-values. In general, the CHIK potential gives the best agreement with experiment. The structure factor is in almost perfect agreement, and the height and position of the FSDP are also in good agreement. In contrast, the GAP structure factor agrees well with the experiment for the second peak and higher q values, but underestimates the height of the FSDP significantly like the Munetoh potential.

Another important feature describing the quality of amorphous models is the defect density. Figure 4.6c shows the number of coordination defects in the corresponding structures. While the structure generated by the Munetoh potential has an extremely high number of wrongly coordinated atoms, the GAP generated structures have almost no defects. Similarly, the CHIK structures contain only a few wrongly coordinated atoms. For different types of potentials we also observe different types of defects. The GAP structures contain mainly wrongly coordinated silicon atoms and the CHIK structures mainly wrongly coordinated oxygen atoms.

In addition to these structural factors, the energetics are essential in judging the quality of amorphous structures. DFT, CHIK and GAP single–point energies for small-scale structures generated by different potentials are shown in Table 4.2. First, we see that the agreement between DFT and GAP in predicting the energies is excellent even for the high energy structures. Second, the structures generated by the Munetoh potential are in general energetically completely off compared to the other structures. Immediately after the quenching process and the first relaxation, the GAP generated structures are energetically most favorable. However, after the re-relaxation of the CHIK-generated structures, within the error bars, they are even slightly more favorable than the structures directly generated by the GAP.

Considering the low-defect density, the excellent structure factor and low energy of the CHIK-generated structures, this opens up a new way to produce realistic amorphous silica structure models. By combining low quench rate CHIK molecular dynamics (MD) simulation with subsequent GAP equilibration, a realistic structure with a structure factor close to the experiment and accurate energetics and bond distances can be generated. This is shown in Figure 4.6d, where the structure factor of a CHIK-only melt-quench simulation and a 'hybrid' simulation are shown. Both simulations capture the structure factor of silica quite well. After equilibration of the slow-quenched CHIK model with the GAP, the FSDP decreases slightly in height, but the minimum between the first and second peaks is better reproduced. The energy of the resulting models is shown in Figure 4.6e. Depending on the quench rate of the initial CHIK quench, a significant gain in energy can be achieved, especially compared to the energy values in Table 4.2. Moreover, energy values close to experimentally determined values between 77 and 130 meV/SiO_2 can be reached.[306–308]

Although we are now able to generate realistic amorphous structure models for silica, the result is not completely satisfactory. It is still not clear why the GAP does not give a structure with a reasonable structure factor in melt-quench simulations, while more primitive CIPs achieve better results. One possible reason could be the lack of long-range interactions. CHIK as well as BKS and the Vashishta potential include long-range interactions and are all able to give higher FSDPs in the generated structures. In the literature, the origin of the FSDP peak is discussed to be caused by intermediate range ordering of SiO_4 tetrahedra.[197,309] However, in the case of other related materials such as titania[310] and hafnia,[311] a better match between the MLIP generated structure factor and the experiment was possible. However, unlike silica, both materials are not typically glass forming. While silica has a critical cooling rate of $\approx 10^{-3}$ K/s,[312] amorphous hafnia[313] and amorphous titania are commonly produced by deposition from the gas phase or in the case of titania also by sol-gel synthesis.[314] These methods correspond to significantly higher quench rates and are therefore orders of magnitude closer to the quench rates achievable by simulations. A similar behavior is found in the case of metallic glasses like Cu-Zr, where also much higher experimental quench rates are necessary, and the corresponding structure factors from a MLIP matches the experimental reference well.[315] Finally, we have no compelling evidence that the differences in quench rates or the lack of long-range interactions are causing the difference in the height of the FSDP. Here, further research is needed.

4.4 Summary

In this chapter, we have demonstrated the ability of MLIPs to reproduce the thermodynamic properties of silica. We showed that the accuracy of the MLIP strongly depends on the exchange-correlation functional used for the training data. However, if the MLIP provides accurate energies and forces, as SCAN does for silica, highly accurate bulk moduli and phonon spectra can be calculated. Moreover, the agreement of calculated phase diagrams with experiments is also superior to CIPs. We show that

we can calculate both low-temperature phase diagrams using the quasi-harmonic approximation and high-temperature phase diagrams using thermodynamic integration in good agreement with experiment. Moreover, we discuss the uncertainties of these phase diagrams and explain that already small differences in the energies provided by the exchange-correlation functional can lead to significantly shifted phase transition temperatures and pressures. Finally, we have investigated the ability of the GAP model to describe amorphous phases. The energetic agreement for many structural models with the SCAN reference is excellent. However, structural models generated within melt-quench simulations significantly underestimate the height of the FSDP. To overcome this issue and to generate realistic amorphous structure models, we introduced a hybrid approach combining the GAP with the CHIK potential. This allows to generate low energy structures with close-to-experiment structure factors.

Silica under high-pressure 5

This chapter is based on the following four publications:

Erhard, L.C., Rohrer, J., Albe, K., Deringer, V. *A machine-learned interatomic potential for silica and its relation to empirical models.* npj Computational Materials 8, 90 (2022). https://doi.org/10.1038/s41524-022-00768-w,[137]

and

Erhard, L.C., Rohrer, J., Albe, K., Deringer, V. *Modelling atomic and nanoscale structure in the silicon–oxygen system through active machine learning.* Nature Communications 15, 1927 (2024). https://doi.org/10.1038/s41467-024-45840-9,[138]

and

Erhard, L.C., Utt, D., Klomp, A., Albe, K. *Crystal structure identification with 3D convolutional neural networks with application to high-pressure phase transitions in SiO_2.* Modelling and Simulation in Materials Science and Engineering 32, 065029 (2024). http://dx.doi.org/10.1088/1361-651X/ad64f3,[200]

and

Erhard, L.C., Otzen, C., Rohrer, J., Prescher, C., Albe, K. *Understanding phase transitions of α-quartz under high-pressures by machine-learning driven atomistic simulations.* submitted (2024). https://doi.org/10.48550/arXiv.2406.17676.[65]

In Ref. 65,137,138 all calculations have been performed by myself. In Ref. 200 Daniel Utt substantially contributed to the work. Specifically, he implemented the DG-CNN structure identification model and trained the models for the simple crystal structures. Moreover, he performed extensive parameter testing for these systems. My contributions had been the creation of the training database for SiO_2, the training of the structure identification algorithm for SiO_2 and the analysis of the SiO_2 shock simulation.

In this section, we will examine the behavior of silica under high pressure. We will start with the stable crystalline phases over a wide range of pressures and how well these phases are described by the atomic cluster expansion (ACE) potential. Later, we will apply the potential to several phase transformation simulations. We investigate the shock behavior of amorphous silica and α-quartz within molecular dynamics (MD) simulations. Moreover, we try to understand the formation of rosiaite-structured silica in dynamic compression experiments.

5.1 Transition pressures of high-pressure phases

As mentioned in Section 1.1 silica undergoes several phase transitions with increasing pressure and has a number of metastable phases at high pressures. While α-quartz and the higher pressure phase coesite both contain fourfold coordinated silicon, higher pressure phases contain sixfold coordinated silicon. Furthermore, most of the enthalpically competitive high-pressure polymorphs are based on a hexagonal close-packed (HCP) oxygen sublattice.[316] These structures are illustrated in Figure 1.4. For an accurate description of the high-pressure transition of silica, an accurate reproduction of the energetics of these phases is essential.

To analyze this, Figure 5.1a shows the energy-volume curves of several silica polymorphs. Note that not all of these polymorphs were explicitly included in the training database. In particular, the rosiaite-type,[60] SnO_2-type,[72] $NaTiF_4$-type,[72] $P2_1/c$-type[72] and d-NiAs-type silica were not part of the database. Although these phases are not included in the database, the density functional theory (DFT) energy–volume curves are reproduced with nearly the same accuracy as the phase included in the training dataset. In the case of d-NiAs-structured silica, no DFT reference values are shown. In the d-NiAs structure, oxygen is arranged in a HCP sublattice, while silicon is randomly distributed in the octahedral voids. To achieve system sizes capable of properly describing this stochastic distribution, more than 1000 atoms are required. Therefore, DFT cannot be used to determine the energy-volume curves of this structure. We have generated 10 of these structures with different random distributions of silicon in the octahedral voids. In fact, the overall behavior of all these structures is very similar. The ACE results are shown only for compression, since under tension the structure is extremely unstable and amorphizes. Therefore, it can be expected to be unstable under ambient conditions.

Figure 5.1b shows the enthalpy as a function of pressure. From these values, the stable phase at 0 K can be determined (see Section 2.4). Between 2.5 and 3.0 GPa α-quartz transforms to coesite, which is slightly higher than extrapolated experimental results from high temperatures suggest.[30] At higher pressures of 5.5 to 6 GPa, coesite transforms to stishovite, which is in good agreement with corresponding experiments.[31] Stishovite is stable over a wide range of pressures and transforms to $CaCl_2$-type silica. Both phases are structurally similar, with the main difference being a distortion in the a and b lattice parameters. In the case of stishovite, both parameters are identical, but in the case of $CaCl_2$, both are different. Since this shift is a thermal effect, we cannot determine the phase transition using the enthalpy, but instead rely on MD simulations.

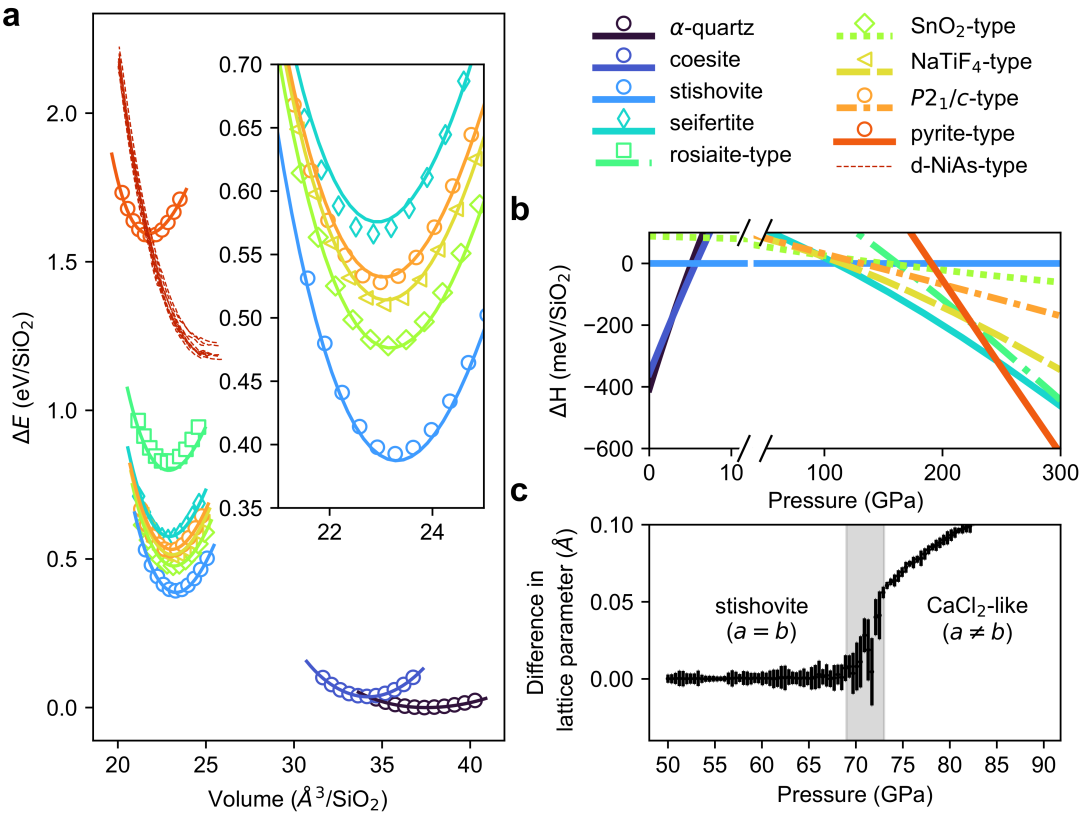

Figure 5.1: **Energy volume curves and enthalpies of high-pressure polymorphs.** (**a**) Energy-volume curves of various stable and metastable high-pressure silica polymorphs calculated with ACE (*lines*) and with DFT (*points*). In case of the d-NiAs structure we show due to the system size (3000 atoms) only the ACE results. (**b**) Enthalpy difference referenced to stishovite in dependence of the pressure. Color coding is identical to (**a**). (**c**) Difference between the a and b lattice parameters of stishovite/$CaCl_2$-structured silica at 300 K at different pressures as extracted from ACE MD simulations. In case of the tetragonal stishovite both lattice parameters are identical, while there is a difference in case of the orthorhombic $CaCl_2$ structure. The figure is a combination of figures from Ref. 138 and 65 with additional data in case of the enthalpy. (**c**) is inspired from Ref. 137, however, was recomputed using the ACE model.

The phase transition between the two phases is shown in Figure 5.1c. We show the difference between the average lattice parameters a and b of an initial stishovite supercell after equilibration at 300 K as a function of pressure. It can be clearly seen that around a pressure of 70 GPa there is a transition from stishovite to a $CaCl_2$-like structure. Experimentally, this transition is measured to occur at lower pressures, around 50 to 60 GPa.[34,317] According to the enthalpy plot, stishovite transforms to seifertite at pressures of ≈110 GPa, which is in good agreement with experimental observations for the transition between $CaCl_2$ and seifertite at 120 GPa and 2400 K, considering the temperature difference.[35] At pressures of ≈246 GPa, the ACE predicts that pyrite-type silica becomes the stable phase. Experimental results found this transition at a pressure

of ≈260 GPa, but at 1800 K.[36] Most remarkably, all metastable phases are correctly predicted to be metastable over a wide range of pressures. This points to the quality of the potential, which appears to be reliable over a wide range of pressures and phases, as well as the underlying DFT data, which give transition pressures that are generally in good agreement with the experimental observations.

5.2 Compression of amorphous silica at room temperature

In addition to the accurate description of high-pressure crystalline phases, an accurate description of the amorphous phase at high pressures is also an important property of machine learning interatomic potentials (MLIP) for silica. Figure 5.2 shows the performance of the ACE potential in a compression simulation of amorphous silica up to 175 GPa. Figure 5.2a depicts the coordination number of silicon during this simulation. For reference, we also show the results of *ab initio* MD simulations[318] and experimental measurements.[52,53] Especially at lower pressures, the agreement between the ACE simulation and all references is impressive. However, while up to 50 GPa ACE seems to be in good agreement with at least one experiment, at higher pressures it underestimates the coordination number of silicon compared to experiment. In contrast, at high pressures the *ab initio* simulations are in good agreement with our results. These results also underestimate the coordination number of silicon. At a pressure of 175 GPa, the average coordination number of our simulation is about 6, while in the experiment it is about 7. Since this is an average coordination number, it does not mean that there are no atoms that are sevenfold-coordinated. As can be seen in Figure 5.2b, there is indeed a significant amount of silicon atoms that are sevenfold-coordinated. The discrepancies may be explained by the different time scales. While our MD simulations simulate a time of about 1 ns, the experimental time scales are more than 10 orders of magnitude longer. This could also explain, the deviation of the *ab initio* reference from the experiment.

Finally, as mentioned in Chapter 1, it may be somewhat surprising that silicon can be sevenfold-coordinated in amorphous silica at pressures as low as 175 GPa. In Figure 5.2c we show some exemplary coordination polyhedra of sevenfold-coordinated silicon taken from the snapshots of our simulations. The pressure ranges in which these polyhedra occur are pressure ranges in which all stable silica polymorphs contain only sixfold-coordinated silicon. At higher pressures, however, pyrite becomes stable, containing silicon atoms with 6+2 coordination, with similarities to the sevenfold-coordinated silica.[54]

5.3 Shock compression of α-quartz and vitreous silica

As discussed in Section 1.1 the study of shocks is essential for understanding the formation of amorphous lamellae in naturally shocked quartz. Experimentally, there are two ways to approach these natural meteorites shocks. Recent *in situ* shock experiments were able to identify phases formed during the ≈100 ns after the shock. The total

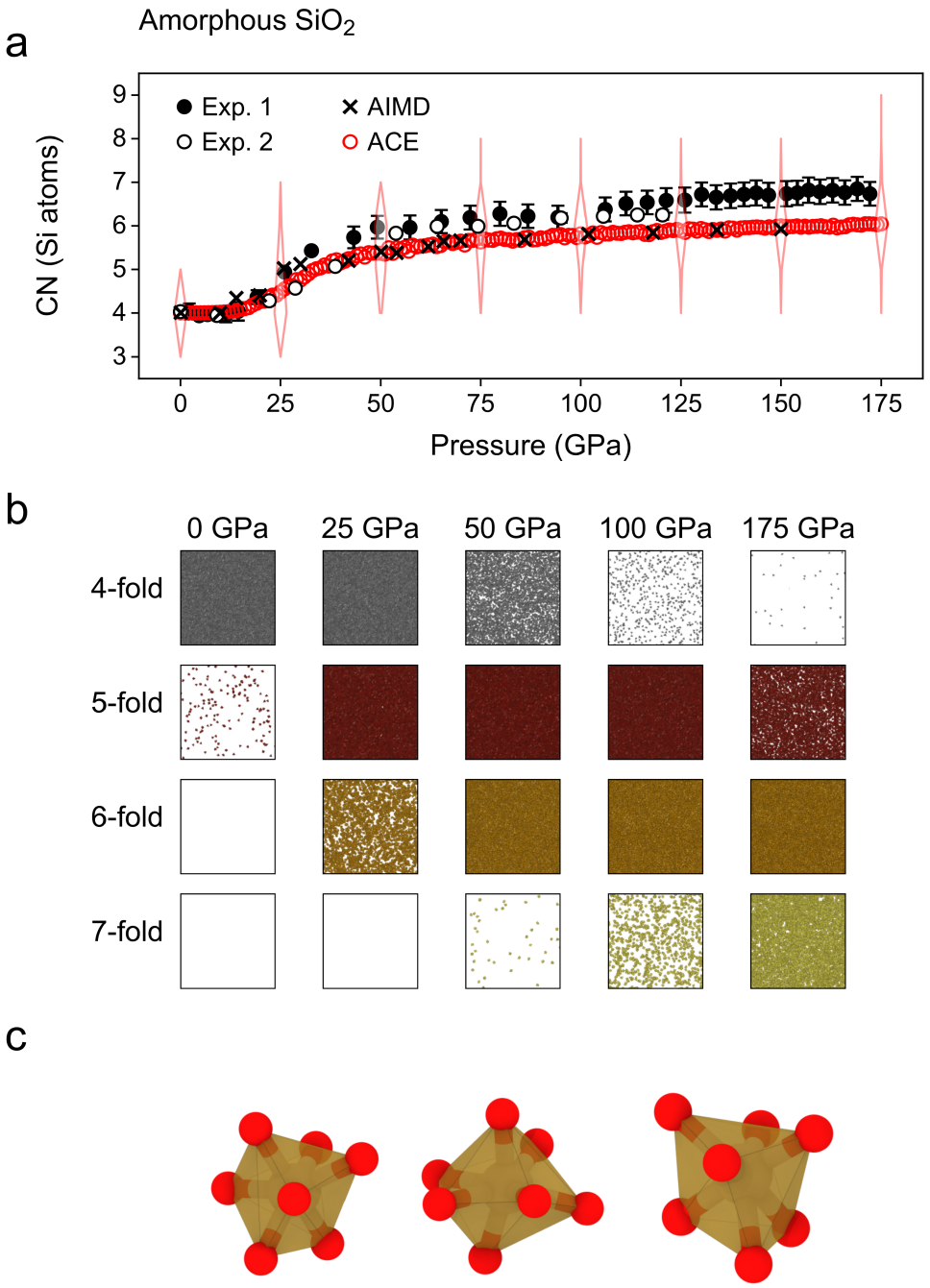

Figure 5.2: **Compression of amorphous silica at room temperature.** (a) Average coordination number (CN) of silicon within silica at different pressures. The violin plot indicates the distribution of the coordination number. Reference data from experiments ('Exp. 1'[52], 'Exp. 2'[53]) and *ab initio* MD[318] is additionally shown. (b) Silicon coordination polyhedra with certain coordination numbers shown for several snapshots of the simulation. (c) Selected coordination polyhedra of sevenfold-coordinated silicon. The simulation has been performed by increasing the pressure iteratively. First over 2.5 ps the pressure was increased by 1 GPa, followed by an equilibration of 2.5 ps. This was repeated up to a pressure of 175 GPa. Reproduced from Ref. 138. Original figure published under the CC-BY 4.0 license (https://creativecommons.org/licenses/by/4.0/).

shock state, however, does not last much longer.[64,78] In contrast, meteorite shocks last from microseconds to seconds, depending on their size.[319] Because of these time differences, other experimental approaches have been developed using rapid compression in diamond anvil cells, but these are four orders of magnitude slower than natural meteorite impacts.[60] The timescales of MD simulations can reach the timescales of shock experiments, allowing a direct comparison between the two methods. Moreover, MD simulations allow direct observation of kinetic processes at the atomistic level. In this section, we will compare the shock behavior of quartz and amorphous silica and analyze similarities and differences. We will use the Hugoniostat method described in Section 2.3. Afterwards in the subsequent section, we investigate the differences between the results of our shock simulations and the results of the dynamic diamond anvil cell experiments.

Figure 5.3 shows the time evolution of amorphous silica under a shock at a pressure of 50 GPa. We analyzed the shock simulation using two methods. The first method is a newly developed machine-learning based structure identification scheme for silica (see Section 2.7). This scheme classifies each atom based on its 64 nearest neighbors. The corresponding per atom classifications are shown in Figure 5.3a for certain snapshots and the phase fraction over time is shown in Figure 5.3b. It can be seen that almost the whole structure is identified as amorphous in the beginning, before the shock starts. After a few picoseconds the structure starts to partially melt. However, after 250 ps the proportion of crystalline phases increases strongly. Most remarkably, several crystallites with the d-NiAs structure appear. This structure is based on HCP oxygen sublattice with silicon randomly distributed in the octahedral voids (see Figure 1.4). Additional support for this structure is provided by the PTM results shown in Figure 5.3c-d. Even at this stage of the shock, most of the oxygen sublattice is crystallized within a HCP lattice. After a maximum at about 300 ps, the proportion of the d-NiAs phase is already decreasing. Instead, SnO_2-, $NaTiF_4$ and $P2_1/c$-type silica and even more stishovite appear more frequently. All these phases share the HCP oxygen sublattice, but show different arrangements of silicon atoms (see Figure 1.4). Besides the spread of these phases, the amount of amorphous phase and melt continues to decrease. Finally, after 2.5 ns, stishovite dominates with a still growing phase fraction of about 60%.

These results are in good agreement with thermodynamics expectations, since stishovite is the stable phase under these conditions. Moreover, *in situ* shock experiments have observed stishovite under shock of amorphous silica under these conditions.[78] However, the kinetic process of this stishovite formation was unclear. We can now clearly observe that stishovite does not crystallize directly from the amorphous phase. Instead, an intermediate crystalline phase, the d-NiAs with the same HCP oxygen sublattice, crystallizes first from the amorphous phase. This corresponds to a rapid ordering of the oxygen atoms. Only after that the silicon atoms are ordered, which allows the occurrence of SnO_2-, $NaTiF_4$ and $P2_1/c$-type domains all with slightly different silicon ordering. Finally, due to energetics stishovite becomes the dominant phase. We note here that the PTM alone would not be able to differentiate between these phases. Instead, the detailed DG-CNN structure identification enabled these extremely revealing results.

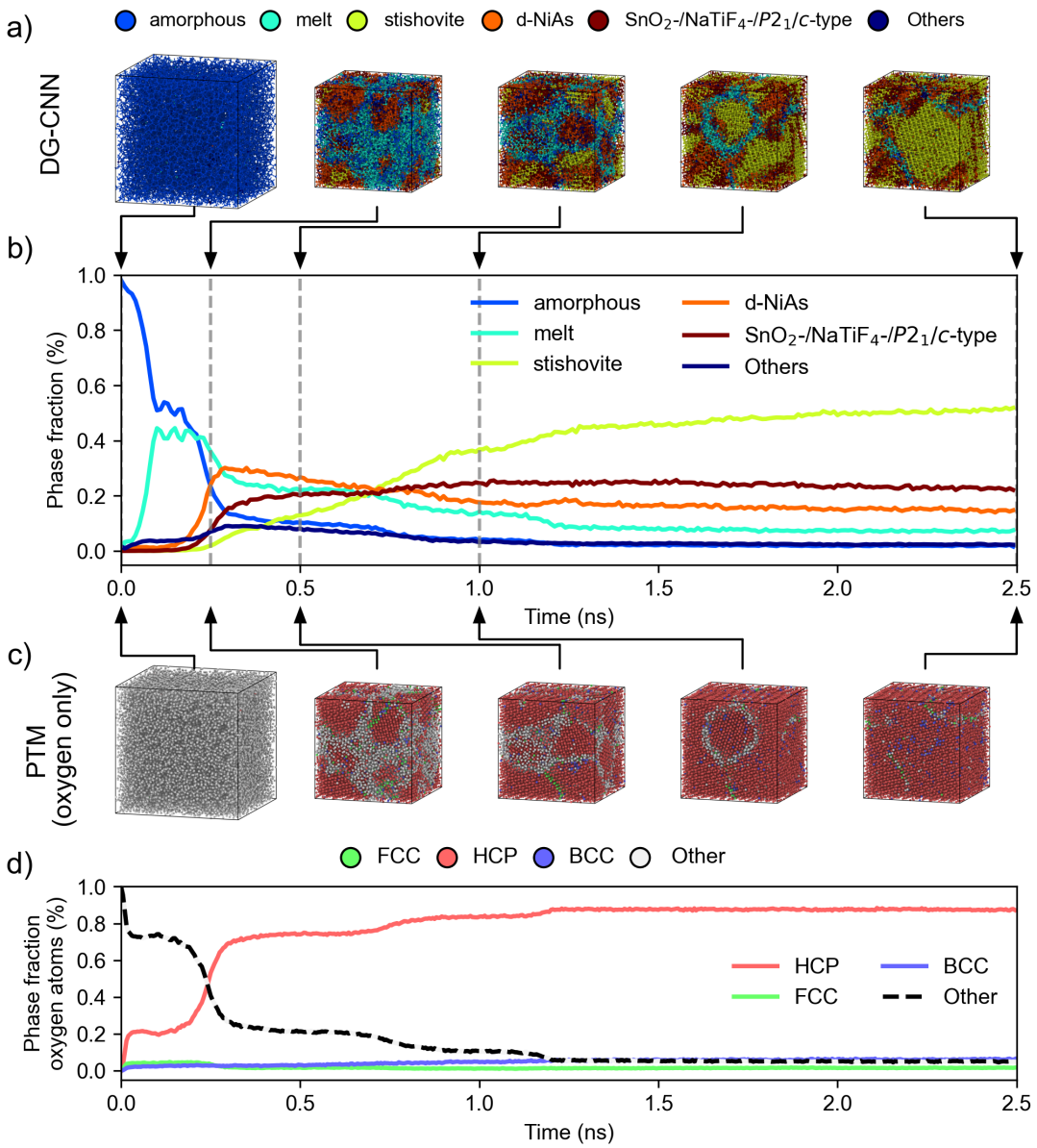

Figure 5.3: **Shock simulation of amorphous silica.** Hydrostatic shock simulation of vitreous silica at a pressure of 56 GPa over a time of 2.5 ns. (a) Dynamic Graph-Convolutional Neural Network (DG-CNN) (see Section 2.7) structure identification applied to snapshots from the shock simulation. Different phases are colored accordingly. (b) Phase fractions of the different phases during the shock simulations. Colors are the same as in (a). (c) Polyhedral template matching (PTM) results on the oxygen sublattice for the same simulation and corresponding phase fractions in (d). Reproduced from Ref. 200. Original figure published under the CC-BY 4.0 license (https://creativecommons.org/licenses/by/4.0/).

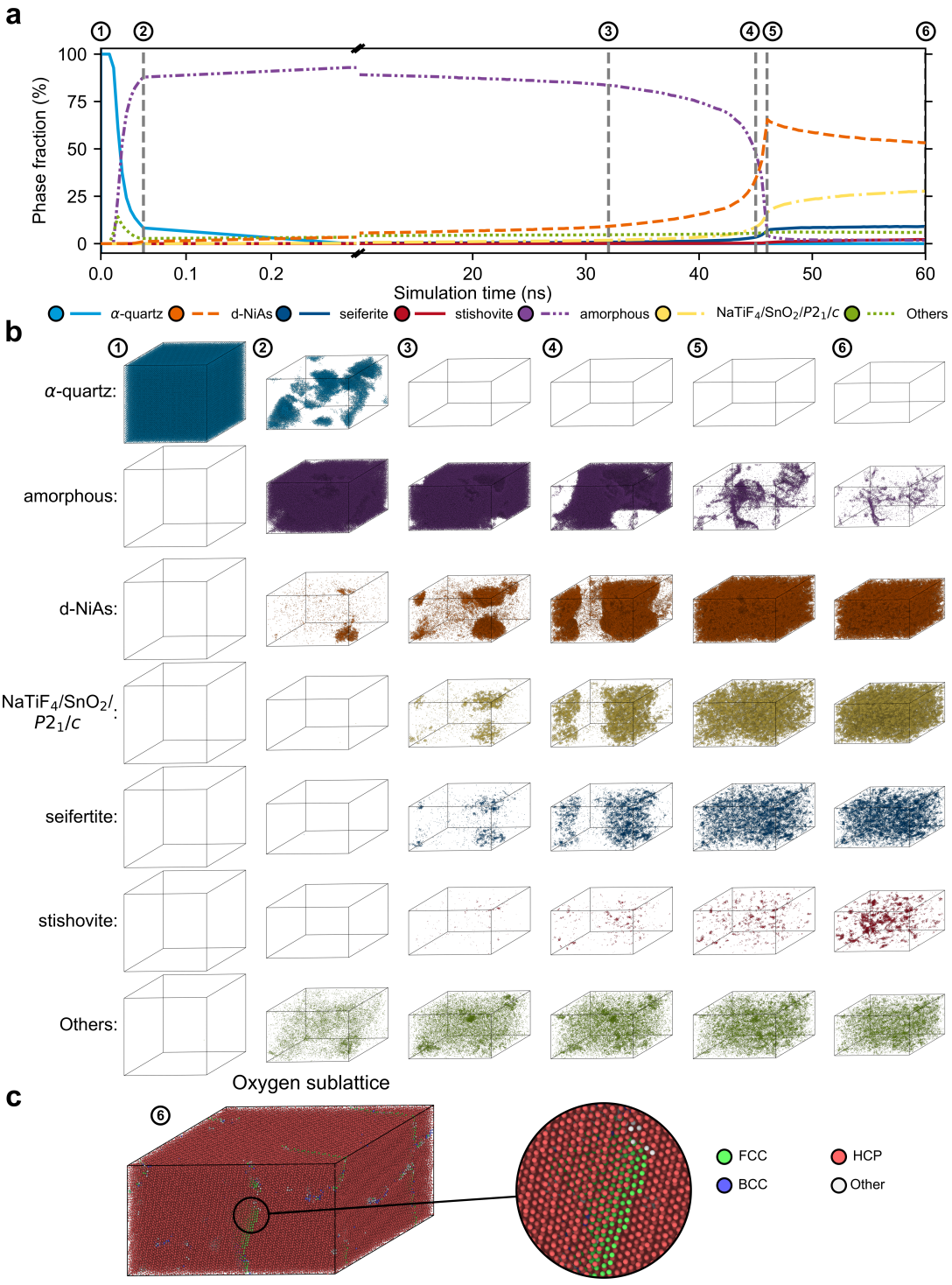

Figure 5.4: **Shock simulation of quartz.** Uniaxial shock simulation of quartz at pressure of 56 GPa over a time of 60 ns. (a) Phase fraction of various phase as identified using the DG-CNN structure identification (see Section 2.7). (b) Snapshots at various time steps showing the occurrence and distribution of selected phases in the structure based on a DG-CNN classification. (c) Final snapshot after 60 ns showing only the oxygen sublattice with PTM structure identification. Reproduced from Ref. 65.

In an *in situ* shock experiment of α-quartz at similar pressures, the d-NiAs phase was observed instead of stishovite. To investigate this behavior and to see where the differences come from, we performed additional shock simulations for α-quartz. The result is shown in Figure 5.4. In contrast to the shock simulation of amorphous silica, the time scales in this case are significantly longer. Instead of 2.5 ns, we simulated 60 ns. The phase fractions predicted by the DG-CNN are shown in Figure 5.4a. Already 100 ps after the start of the shock, most of the structure is amorphized and only traces of α-quartz remain in the structure. At the same time, a small crystallite has already appeared within the amorphous matrix, which can be classified as d-NiAs structured silica. This can be seen in Figure 5.4b. The seed grows slowly over time, at least on MD time-scales, and in contrast to the fast growth during the shock of amorphous silica. It takes about 46 ns for the structure to be almost completely crystallized. At this time the d-NiAs phase clearly dominates with a phase fraction of about 70%. With longer simulation times this phase fraction decreases again. This is accompanied by an increase in the SnO_2-, $NaTiF_4$ and $P2_1/c$-type silica and seifertite domains, while the increase in the stishovite fraction is much smaller. As before, the PTM identifies the oxygen sublattice as mostly HCP after 60 ns (see Figure 5.4c).

Although the DG-CNN structure identification is good for identifying the structure at the atomic level, an even better proof of agreement with experiment is the comparison of measured XRD pattern with calculated XRD pattern. This comparison is shown in Figure 5.5. The agreement between the experimental XRD pattern from Tracy *et al.* [64] and that of our simulation cell after 60 ns is impressive. Although the experimental spectrum is quite noisy, the characteristic peaks are well reproduced by the simulated spectrum. Moreover, in addition to the sharp peaks that also appear in the theoretical spectrum of the d-NiAs phase, a broad peak at a 2Θ value of 12° appears in both patterns. The origin of this peak was not entirely clear, but two possible options were discussed by Tracy *et al.* [64] The first option was that it was caused by a superposition of the crystalline phase with an amorphous phase. The corresponding broad peak would originate from the first sharp diffraction peak (FSDP) of the amorphous phase. This option can be excluded by our simulations, since the entire structure is clearly crystallized. The other possible assumption they made was that local short-range ordering of the silicon atoms within the d-NiAs structure leads to this broad peak. This is clearly supported by our data. First, the DG-CNN structure identification clearly shows that there are a certain number of SnO_2-, $NaTiF_4$ and $P2_1/c$-type silica and seifertite domains that do not have random ordering of the silicon atoms. Instead, the silicon atoms in these domains must have a localized short range order. Second, the decomposition of the XRD spectrum in Figure 5.5 clearly shows that the first broad peak is caused only by Si-Si contributions, which clearly supports the assumption of localized ordering.

The combination of both shock simulations, the vitreous silica simulation and the quartz simulation, demonstrates the importance of the d-NiAs structure. The results clearly show that this phase occurs as an intermediate state in the crystallization process to stishovite and other metastable phases. The differences in the results between the two simulations are probably due to the different temperatures over the simulation time. These temperature profiles are shown in Figure 5.6. Note that the temperatures

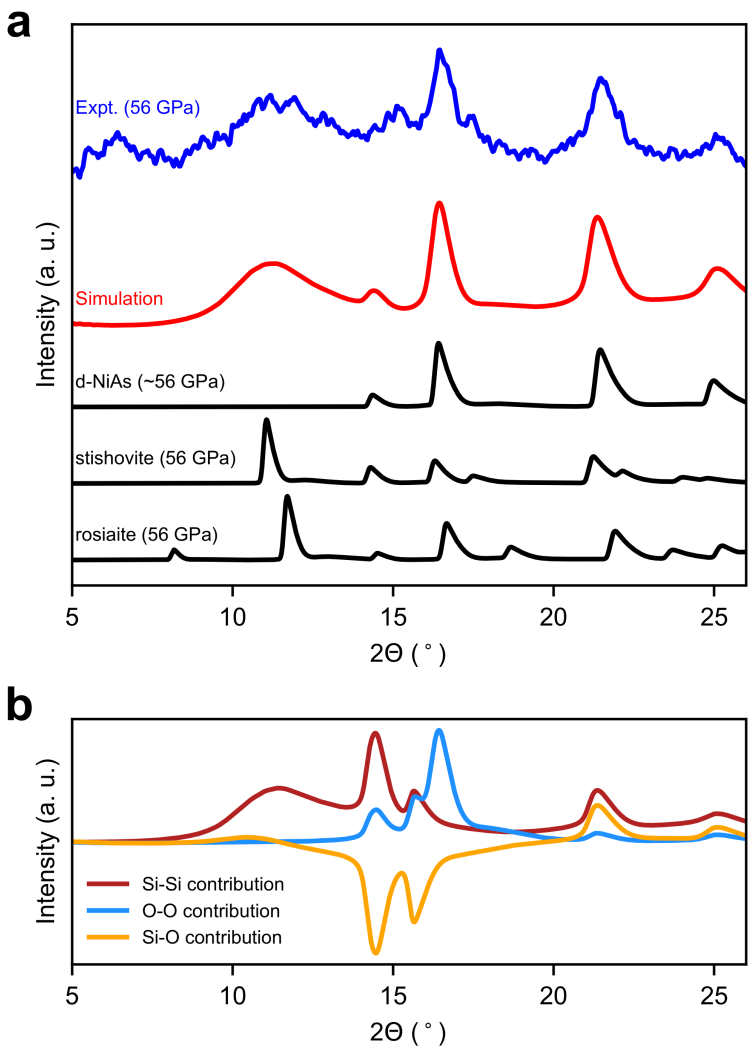

Figure 5.5: **X-ray diffraction (XRD) pattern of shocked quartz.** (a) XRD pattern of quartz from experiment at 56 GPa pressure[64] compared to the pattern of the final snapshots (after 60 ns) of the MD shock simulations with theoretical pattern of several crystalline high-pressure polymorphs. The wavelength distribution is assumed to be identical to the distribution in experiment.[64] (b) Contributions of different distances, e.g. Si-Si, O-O and Si-O, to the total XRD pattern of the shocked structure. Reproduced from Ref. 65.

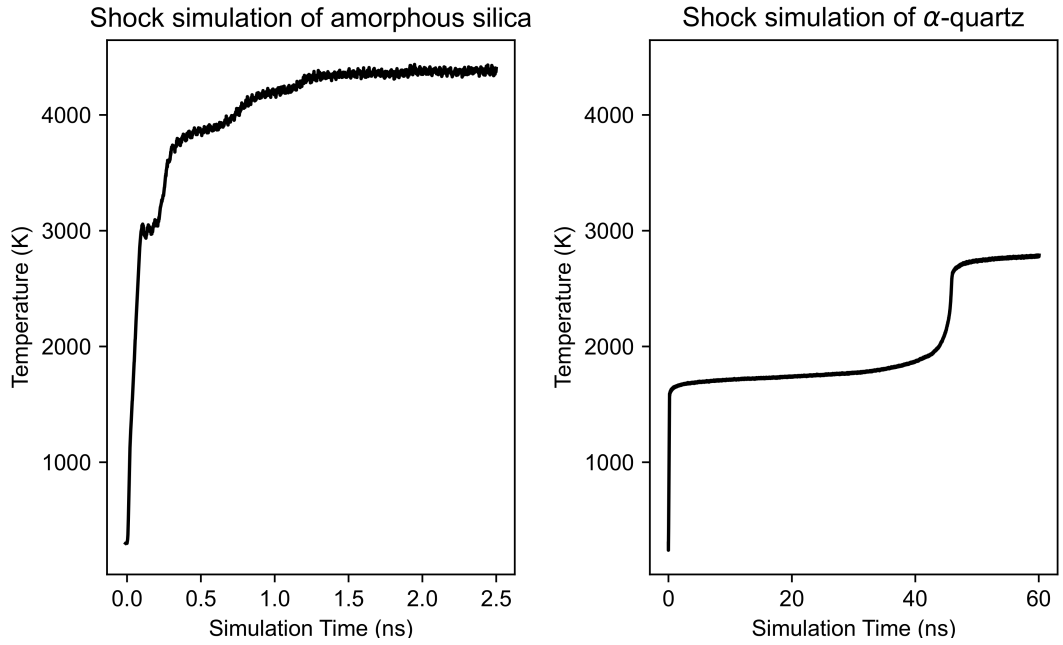

Figure 5.6: **Temperature during shock simulations.** The temperature as a function of the time during both shock simulations shown in Figure 5.3 and Figure 5.4.

change dynamically during the shock and are given by the Hugoniot relations (see Section 2.3). In the case of amorphous silica, the temperature rises extremely fast to values higher than 4000 K, which allows for fast kinetics. In contrast, we observe much lower temperatures for α-quartz. Only after the end of the crystallization the temperature rises to values slightly below 3000 K, which is still lower compared to the case of amorphous silica. This suggests that the shock of amorphous silica can be seen as an accelerated version of the shock of α-quartz. Correspondingly, after longer simulation times in the case of α-quartz, one would expect further ordering of the silicon atoms, eventually ending in a phase fraction of 100% stishovite.

5.4 The occurrence of rosiaite-type silica

While the shock simulations are in excellent agreement with the experiment, we did not observe rosiaite-structured silica as in the dynamic diamond anvil cell experiments on quartz.[60,74] One reason for this may be the significantly longer time scales of these experiments and that rosiaite-type silica may take longer to crystallize from the amorphous phase. At the same time, these experiments were performed at room temperature and pressures only up to 30 GPa. Based on the energetics in Figure 5.1a crystallization via the amorphous phase and the d-NiAs phase as intermediate states seems unrealistic. Instead, one would expect rather the direct formation of stishovite within this process. Correspondingly, we observed almost no rosiaite-structured silica in our shock simulations. Recently, Tsuchidya *et al.* proposed a diffusionless mechanism of direct

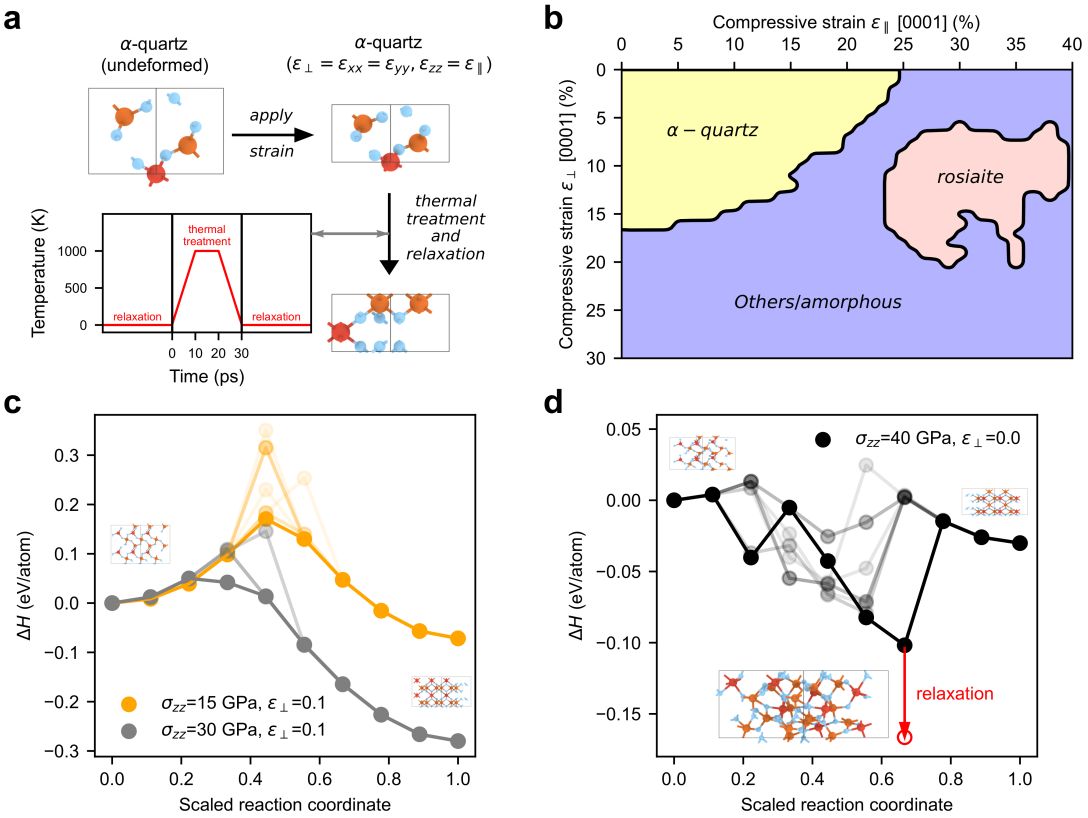

Figure 5.7: **Formation of rosiaite-structured silica from quartz.** (a) Deformation of quartz according to two strains $\epsilon_\perp$ perpendicular to the c-direction and $\epsilon_\parallel$ parallel to the c-direction. After the deformation of the quartz cell, the structure undergoes a thermal treatment to allow relaxation of the positions. The final structure is structurally analyzed. (b) Results of the DG-CNN structure identification on the final deformed and relaxed structures based on different supercell sizes in dependence of the strain state. The stability regions of α-quartz and rosiaite-structured silica are shown. In the other regions mainly amorphous silica has been dominating, despite some exceptions for other crystalline structures. (c) Transitions paths from solid-state nudge elastic band (SS-NEB) calculations from quartz to rosiaite-structured silica. The initial state is quartz strained by a perpendicular strain $\epsilon_\perp$ of 0.1 and relaxed in c-direction according to an external pressure of 15 GPa (*orange*) or 30 GPa (*gray*). From this state the transition to rosiaite-structured silica is performed, assuming a fixed cell size in a-b-direction, but with allowed relaxation within c-direction. The transparent background line arise from many possible transformation ways from α-quartz to rosiaite-structured silica, e.g. one oxygen atom can move to several oxygen positions in rosiaite-structured silica. Only the lowest energy path is drawn as bold. Final rosiaite structures with corresponding final oxygen and silicon positions are taken from (b) at a strain of $\epsilon_\parallel$=0.27. (d) Same transition as in (c), however, this time under a perpendicular strain $\epsilon_\perp$ of zero. Here, rosiaite-structured silica becomes only more stable than α-quartz under pressures of roughly 40 GPa. In the transition path there are several lower enthalpy configurations appearing, which are disordered.

transformation of α-quartz to rosiaite-structured silica.[73] They performed DFT calculations in which they deformed α-quartz by applying high strains to the cell and observed a transformation to rosiaite-structured silica. Based on these calculations, we will now investigate the conditions under which this direct and diffusionless transformation occurs.

Figure 5.7a shows the approach we used to explore the possible transformation of α-quartz. We systematically deformed α-quartz over a wide range of different strains parallel and perpendicular to the c-axis. After deformation, we applied a thermal treatment and performed energy minimization with respect to atomic positions. Finally, on the deformed and minimized cells, we used our DG-CNN structure identification to identify the corresponding crystal structures.

The average result for a wide range of α-quartz supercells is shown in Figure 5.7b. It can be clearly seen that rosiaite-structured silica appears over a wide range of strains applied to quartz. We note that even for 8×8×8 supercells, the resulting rosiaite-type structures are often so free of defects that symmetry analysis by `spglib`[320] can identify them as belonging to the appropriate $P\bar{3}1m$ space group. It is clear from the results that rosiaite occurs only in cases where the strain state is not purely uniaxial, but also includes strain components perpendicular to the main strain direction. At the same time, a purely isostatic strain state, e.g. equal strain in all directions, would also not lead to the appearance of rosiaite-structured silica.

Figure 5.7c shows the barrier between α-quartz and rosiaite-structured silica as determined by SS-NEB calculations. First, the α-quartz is strained to a certain perpendicular strain $\epsilon_\perp$=0.1. The lattice constant in the c-direction is determined by structural relaxation under the given pressure of 15 GPa (*gray*) or 30 GPa (*orange*). The final rosiaite states are taken from the phase transformation calculations from Figure 5.7b ($\epsilon_\parallel$=0.27) and are strained to the same lattice size in a-b direction as α-quartz. The lattice parameter in the c-direction is determined identically as for α-quartz. Therefore, during the SS-NEB, calculation only the c-axis is changed, while the a- and b-axes are fixed. Since atoms within α-quartz can move to different equivalent positions within the rosiaite-structured silica, there are many possible paths. The lowest energy path is shown in bold, while the other paths are shown in a light transparent color. In both cases, at 15 GPa and 30 GPa, there is a clearly defined barrier. In the case of 15 GPa, the height of the barrier is higher than 150 meV/atom, and in the case of 30 GPa pressure in c-direction, it decreases to roughly 50 meV/atom.

Additionally, Figure 5.7d shows the transition path between α-quartz and rosiaite-structured silica, but under strain $\epsilon_\perp$=0.0. Under these conditions, rosiaite-type silica becomes energetically more favorable at pressures of about 40 GPa. The energy gain of the transformation is also significantly lower. Moreover, it can be seen that several intermediate images have a lower enthalpy compared to both α-quartz and rosiaite-structured silica. After relaxing these images, we obtain disordered structures. This implies that the system prefers to amorphize under these conditions and that direct transformation into the rosiaite structure is not possible.

How does this relate to the shock experiments and the dynamic diamond anvil cell compression experiments? In fact, through discussion with experimentalists, we have

found that during diamond anvil cell compression experiments, not only strain in the main compression direction can be observed, but also a strain of about 10% perpendicular to this compression direction, induced by the matrix material surrounding the sample. This is in excellent agreement with our observations in Figure 5.7b. At the same time the enthalpy barriers calculated for the transition from α-quartz to rosiaite-type silica can be realistically overcome within the experimental timescales. In contrast, in our shock simulations as well as in the shock experiments, there is probably no strain component perpendicular to the loading direction. Therefore, quartz seems to amorphize rather than directly transform into rosiaite-type silica, which is also in good agreement with our observations in the shock simulations. In the case of natural shocks, things get more complicated. On the one hand, the times are shorter than in the compression experiments. Therefore, it is not clear whether they are sufficient to overcome the barrier between α-quartz and rosiaite. However, it may be possible, especially if stresses are slightly higher than 30 GPa. In addition to the required timescales, the boundary conditions must also match. Since these depend on the exact composition of the rocks and their environment, they are likely to be highly dependent on the specific characteristic of each individual impact and are difficult to predict. All in all, it seems from the mentioned results that the formation of amorphous lamellae can be induced by a number of processes, depending on the specific conditions of the impact:

- Direct amorphization
- Amorphization with subsequent crystallization and reamorphization after the shock
- Direct transition to another crystalline structure and reamorphization after the shock

From the shock and the SS-NEB simulations we can conclude that direct amorphization of quartz is possible. Moreover, recrystallization can be observed, although it may not occur depending on the temperature and pressure conditions. Also, depending on the stress and strain boundary conditions, direct transitions to rosiaite-type silica may occur. In summary, all of these processes appear to be realistic and could also occur in nature.

5.5 Summary

In this chapter, we have shown the capabilities of the ACE potential in performing high pressure simulations of silica. First, we showed that the potential is able to reproduce the experimental thermodynamics of the systems, focusing on the phase stabilities. Here, the potential showed excellent qualitative agreement and in many cases close to quantitative agreement. Based on these positive aspects, we started to analyze the shock behavior of amorphous silica and α-quartz. We found that amorphous silica transforms to stishovite with an intermediate d-NiAs-like phase under shocks of 50 GPa. In this

d-NiAs-phase, oxygen is arranged in a HCP sublattice, as in the case of stishovite. However, silicon atoms are randomly arranged in octahedral voids. Over the time of the shock simulation, this silicon ordered, eventually leading to the structure of stishovite. In the case of shocked quartz, the d-NiAs structure was also observed. However, due to the lower temperatures in this simulation, no final transformation to stishovite could be identified even after a simulation time of 60 ns. Only a local ordering of the silicon atoms was found, which does not correspond to a long-range order. All these results are in excellent agreement with experimental observations and deepen the understanding of them. Finally, we also tried to understand the formation of rosiaite-type silica observed in dynamic diamond anvil cell compression experiments. We found that this phase can only be created under certain boundary conditions, which require not only strain along the c-direction in α-quartz, but also strain perpendicular to it. From these results we found that there are essentially three scenarios for the formation of amorphous lamellae in quartz in natural impacts. Direct amorphization, amorphization with subsequent crystallization and reamorphization after the shock state has vanished, or direct transformation of quartz into another crystalline phase such as rosiaite-type silica with subsequent amorphization after the shock state has disappeared. Based on our results, all three outcomes seem to be possible and depend on the exact boundary conditions such as stress, strain, shock duration and temperature.

Modelling of silicon monoxide 6

This chapter is based on the following publication:

Erhard, L.C., Rohrer, J., Albe, K., Deringer, V. *Modelling atomic and nanoscale structure in the silicon–oxygen system through active machine learning.* Nature Communications 15, 1927 (2024). https://doi.org/10.1038/s41467-024-45840-9.[138]

All calculations in this work have been performed by myself.

In this chapter, we study the structural properties of silicon monoxide using the atomic cluster expansion (ACE) potential. First, we analyze the ability of the ACE potential to describe interfaces between silicon and silica, which is essential for a proper description of silicon monoxide. We then perform melt-quench simulations with the ACE potential to generate structural models of silicon monoxide. These models are compared with models from available classical potentials, such as the Munetoh[117] potential and the Charge-optimized many-body (COMB)[114] potential. Finally, we investigate the possibility of generating structural models of SiO with crystalline silicon instead of amorphous silicon. We observe the crystallization process at the atomistic scale and evaluate under which conditions this crystallization is energetically favorable.

6.1 Interfaces between silicon and silica

An accurate description of the interface energy between silicon and silica is an essential feature of an interatomic potential for the Si–O system. Figure 6.1 shows the interface energies between silicon and silica for different interfaces. We show results for small scale crystalline-amorphous and amorphous-amorphous models that are accessible by density functional theory (DFT) calculations. First, we compute interface energies by single-point evaluations of the energy for unrelaxed interface structures, which were simply added together manually. In general DFT and ACE results are in good agreement, but the ACE systematically underestimates the interface energy. Nevertheless, the hierarchy of interfaces is well reproduced regardless of the type of interface. The interfaces structures were then relaxed using the ACE. Since DFT relaxation would have been too expensive, we used single-point evaluations on these relaxed structures to evaluate the

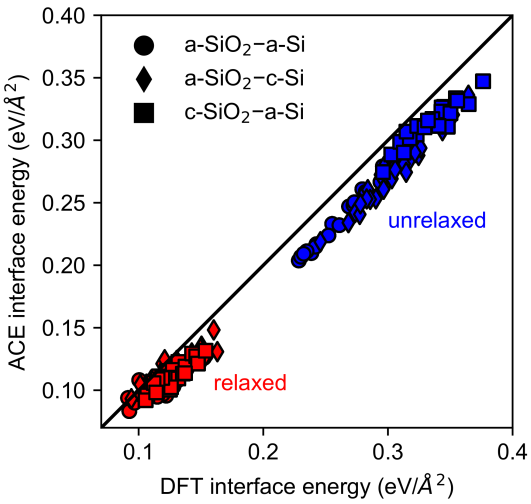

Figure 6.1: **Interface energies between different types of silicon and silica.** Interface models between amorphous silica and amorphous silicon (a-SiO_2–a-Si), amorphous silica and silicon diamond (a-SiO_2–c-Si) and quartz and amorphous silicon (c-SiO_2–a-Si) with corresponding interface energies calculated by ACE and DFT for the ACE-relaxed (*red*) and unrelaxed (*blue*) structures. Reproduced from Ref. 138. Original figure published under the CC-BY 4.0 license (https://creativecommons.org/licenses/by/4.0/).

corresponding DFT interface energies. The first observation is that both, the ACE and the DFT interface energies, are significantly lower, showing the capability of the ACE to find a reasonable relaxed interface. Moreover, the ACE and DFT interface energies of the relaxed interfaces are in good agreement, with a slight underestimation of the energies by the ACE. However, in contrast to the unrelaxed interface structures, the underestimation of the interface energies is smaller here. Also, some discrepancies can be explained by the fact that the DFT energies are not determined from a DFT-relaxed structure, which would correspond to at least a slightly lower energy.

Finally, it can be concluded here that the ACE potential slightly underestimates the interface energy between silicon and silica, especially for unrelaxed high-energy interfaces. Nevertheless, the ACE potential gives a good qualitative description of the interface energies. Moreover, for the important low-energy interfaces the quantitative description is surprisingly good. This makes the ACE a promising model for an accurate description of silicon monoxide.

6.2 Structural models of silicon monoxide from melt-quench simulations

Figure 6.2a shows atomistic models of silicon monoxide generated by melt-quench simulations (see Section 2.2). All structures show a clear segregation between silicon and silica. As the quench-rate decreases, the grain size increases, and the interface area decreases. The structures prepared with the intermediate quench rate have grain sizes

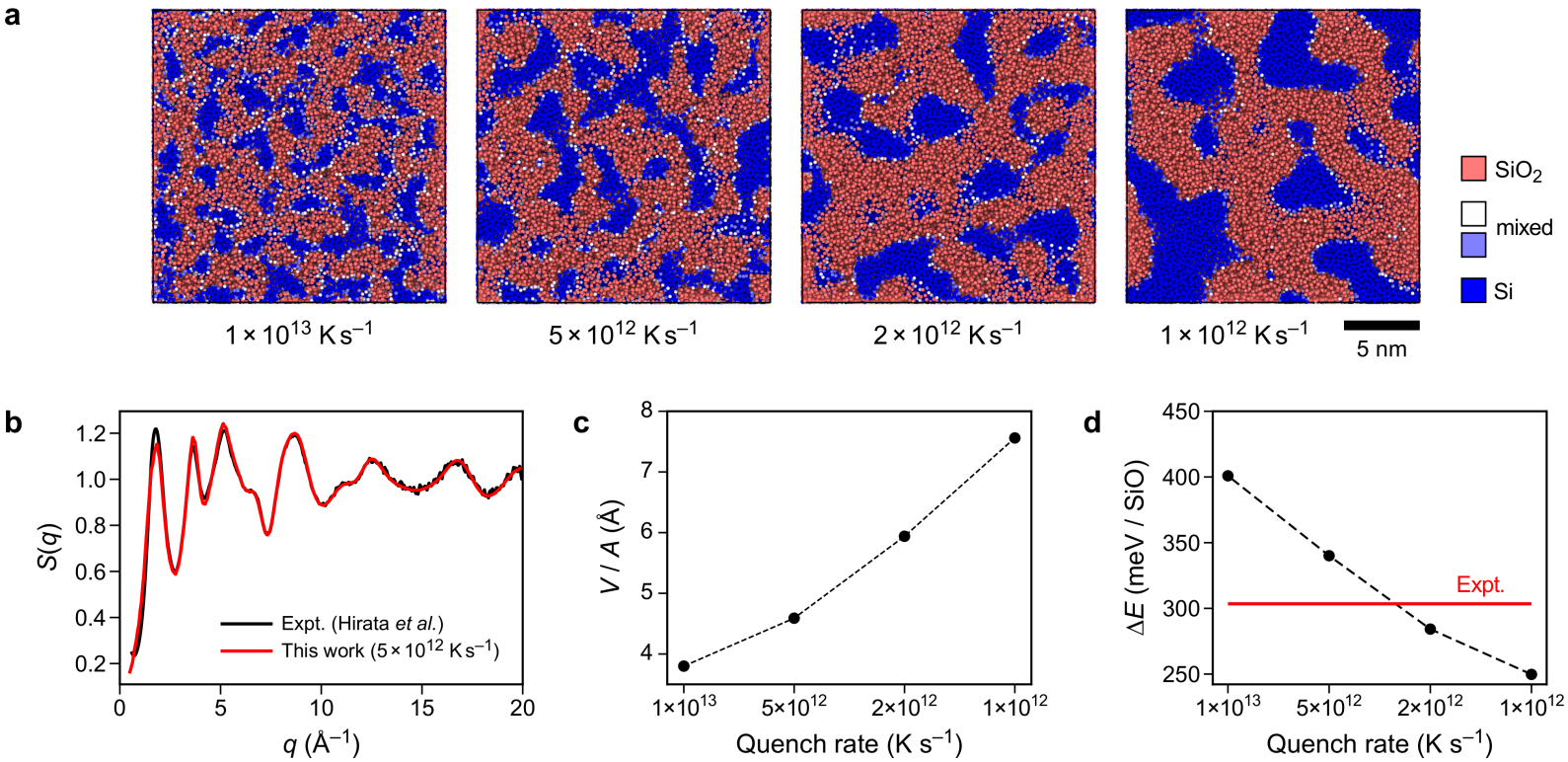

Figure 6.2: **Nanoscale segregation in amorphous silicon monoxide.** (a) Melt-quench generated atomistic models of SiO from different quench rates between 10^{13} and 10^{12} K s^{-1}. The color of the atoms is based on the number of neighbors less than 2 Å apart, which would correspond to zero in Si (*blue*) and four in SiO_2 (*red*). (b) Structure factor $S(q)$ as a function of the wave vector q for the 5×10^{12} K/s quenched structure at 300 K compared to the experimental structure factor from Ref. 102. (c) Ratio of the silicon grain volume to the silica-silicon interface area as a function of the quench rate. (d) Energy difference between the structural models of silicon monoxide compared to a mixture of α-quartz and silicon in its diamond structure. The experimental enthalpy of formation is given for comparison.[321] Reproduced from Ref. 138. Original figure published under the CC-BY 4.0 license (https://creativecommons.org/licenses/by/4.0/).

in good agreement with the experimentally observed grain sizes of 3-4 nm.[101] The X-ray structure factor of the structure quenched with a quench rate of 5×10^{12} K/s is shown in Figure 6.2b and compared with the experimental structure factor. The agreement between the two structure factors is almost perfect. Moreover, the first sharp diffraction peak (FSDP) has almost the same height in both cases. This is particularly surprising, since the FSDP is significantly underestimated for pure silica (see Section 4.3). However, in contrast to silica, silicon monoxide is produced by deposition of SiO from the gas phase.[322] This corresponds to significantly higher quench rates, which may be similar to the quench rates in our simulations. The structure factors of the other structural models are shown in Figure 6.3. All the structure factors of the models generated by the ACE potential show good agreement, while the model generated by a quench rate of 5×10^{12} K/s is probably the best match. For consistency, we also looked at the results for two classical interatomic potentials for Si–O. The Munetoh potential and the COMB potential. The structure factor of a structure generated with the Munetoh is shown in Figure 6.3c. Compared to the experimental structure factor, the result is totally off. In fact, the corresponding structure also shows no reasonable segregation between silicon and silica. In the case of the COMB potential, we observed pore formation during our melt-quench protocol, which induced a strong volume increase. Therefore, we simply re-equilibrated our best matching ACE structure with this potential. The resulting structure factor is shown in Figure 6.3f and is significantly worse than for the ACE. This indicates that the structure is strongly changed by the equilibration.

Figure 6.2c shows the ratio between the volume of the silicon grains and the interface area between the silicon and silica regions. In the case of a spherical inclusion, this could be directly translated into a grain diameter of $d = 6 \cdot V_{\mathrm{Si,grains}}/A_{\mathrm{interface}}$. This corresponds to grain diameters of 24 to 54 Å in the different structures, again in good agreement with the observed grain size and the experimental grain sizes of 3-4 nm.[101] Finally, we investigate the energetics of the relaxed structural models from Figure 6.2a. The results are shown in Figure 6.2d. The energetics of the structures quenched with 5×10^{12} K/s and 2×10^{12} K/s are close to the experimental measured enthalpy of formation.[321] The structures quenched with 2×10^{12} K/s and 1×10^{12} K/s have even lower energies than the experimentally measured value. This is in good agreement with the slightly larger grain sizes of the 1×10^{12} K/s quenched structure and the correspondingly lower interface area. However, it may be surprising that a melt-quench structure is energetically more stable than an experimental structure. Again, this can be explained by the fact that experimentally the material is deposited from the gas phase, inducing a not well equilibrated structure with high formation energy.

6.3 Partially crystallized silicon in silicon monoxide

Experimentally, it has been observed that pure amorphous silicon monoxide partially crystallizes when annealed above 850°C.[323] However, this crystallization is confined to the silicon grains, while the silica remains amorphous. To create partially crystallized structures, we used the silicon monoxide structures from Section 6.2 and performed

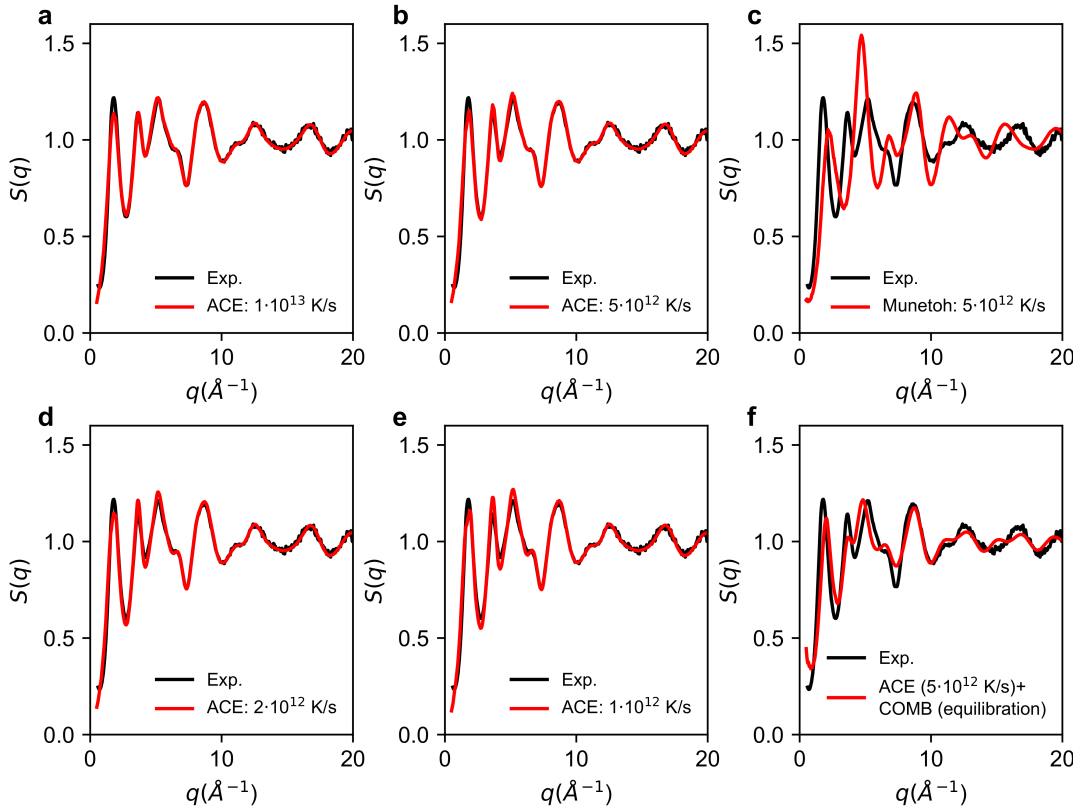

Figure 6.3: **Structure factors of silicon monoxide models.** Structure factors $S(q)$ as a function of the wave vector q for several structural models and compared to experimental measurements (*black*).[102] (a-b,d-e) Structure factors of the models from Figure 6.2a generated at different quench rates with the ACE potential. (c) Structure factor of a model generated with the Munetoh potential using a quench rate of 5×10^{12} K/s. (f) Structure factor of the ACE structure quenched at 5×10^{12} K/s and equilibrated with the COMB potential for SiO. Reproduced from Ref. 138. Original figure published under the CC-BY 4.0 license (https://creativecommons.org/licenses/by/4.0/).

a thermal treatment on these structures, as shown in Figure 6.4a. In this thermal treatment, we cooled the structure over 20 ns from 1400 K to 1200 K. During this simulation, the silicon within the silicon grains partially crystallizes as determined by PTM. The resulting difference is shown in Figure 6.4b, where the silica regions of the matrix are hidden. There are significant differences in the final crystallinity between the different structures from Section 6.2, as shown in Figure 6.4c-f and the bottom panel of Figure 6.4a. While the structures with large silicon grains tend to have a higher proportion of crystalline silicon, the structures with smaller silicon grains show almost no crystallization. This is also supported by the structure factors of the corresponding structures. Figure 6.4g shows the structure factors of the two structures with small silicon grains. There are no sharp peaks in the structure factors for these structures that would indicate crystallinity. In contrast, Figure 6.4h shows the structure factors of

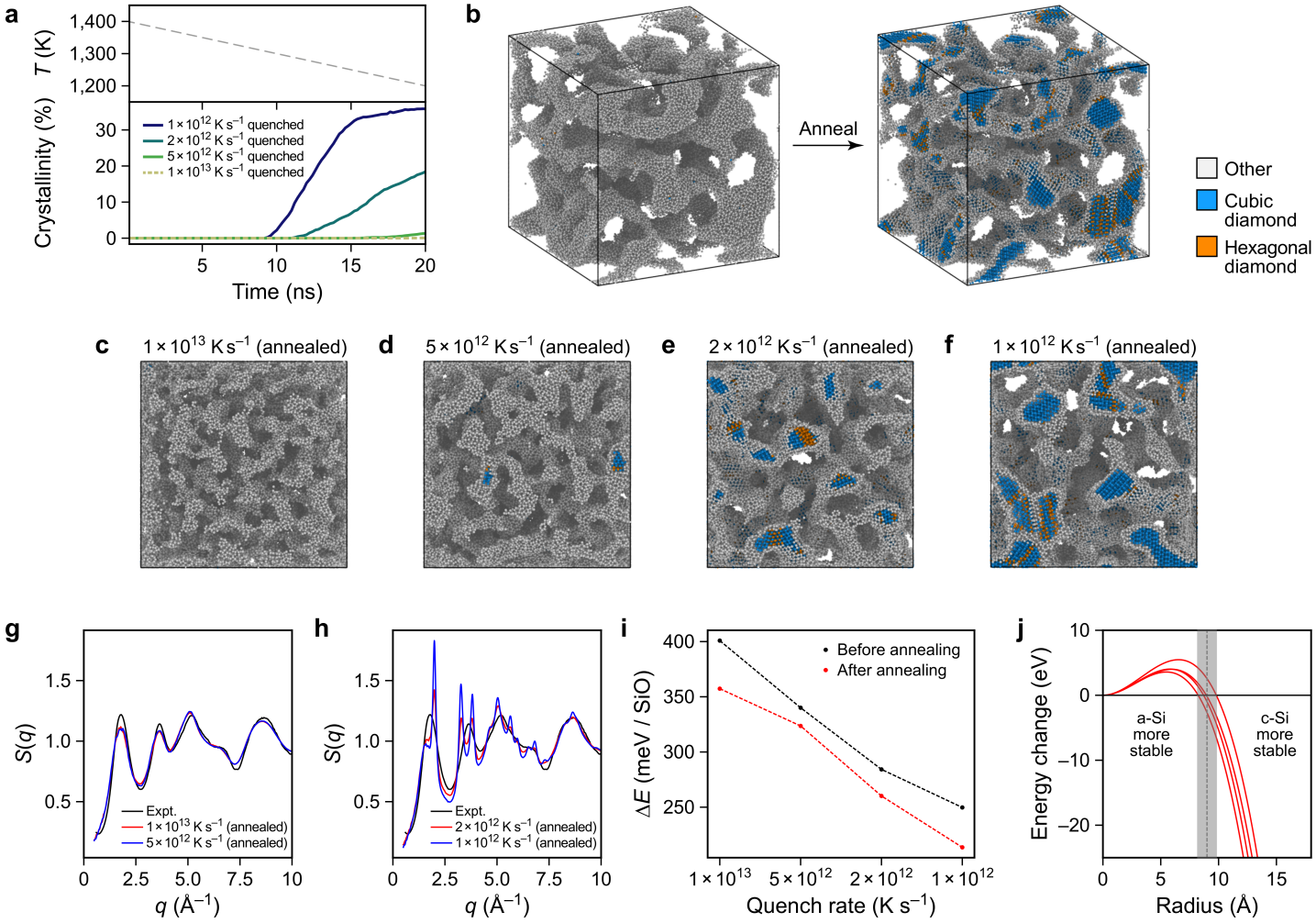

Figure 6.4: Caption on the next page.

Figure 6.4: **Crystalline silicon in silicon monoxide.** (a) Quench simulation of silicon monoxide models from 1,400 K to 1200 K over 20 ns. The input structures are the final structures from Figure 6.2. The bottom panel shows the fraction of crystalline silicon referenced to the total number of silicon atoms in the silicon grains for different input structures. (b) Silicon monoxide structure (10^{12} K s^{-1}) before and after thermal treatment, showing only silicon atoms with less than two oxygen neighbors (2 Å cutoff). The atoms are colored according to their structure as identified by polyhedral template matching (PTM) with a root mean square deviation cutoff of 0.1. (c-f) Silicon monoxide structures from Figure 6.2 after their thermal treatment with the same color coding and atoms shown in (b). (g-h) X-ray structure factors $S(q)$ of the models in (c-f) compared to the experimental structure factor of silicon monoxide.[102] (i) Energy of formation as in Figure 6.2d comparing the structures before and after thermal treatment. (j) Energy difference of an amorphous and a crystalline spherical silicon inclusion in an amorphous silica matrix as a function of inclusion radius. A negative value indicates that crystalline silicon is more stable than amorphous silicon. Several interface energies from Figure 6.6 are used as input for the different functions to illustrate the uncertainty of the model. Reproduced from Ref. 138. Original figure published under the CC-BY 4.0 license (https://creativecommons.org/licenses/by/4.0/).

the silicon monoxide structures with larger silicon grains. Sharp peaks can be seen in these structure factors, clearly indicating partial crystallization of the structure.

Figure 6.5 visualizes the crystallization process of silicon within silicon monoxide. We show only those silicon atoms that are identified as crystalline by a PTM analysis. At 1400 K there are no crystalline atoms in the structure, as expected at the temperature. At 1310 K the first crystalline seed appears, which then grows with decreasing temperature. After a further temperature drop to 1306 K, a second seed appears. Both seeds continue to grow until they percolate the entire silicon network within the silica matrix. While the silicon rearranges during the simulation, the silica matrix remains unchanged.

The energy of formation of the structures before and after annealing is shown in Figure 6.4i. Indeed, at least for these specific structures, there seems to be no relationship between the energy gain and the degree of crystallinity after thermal treatment. This seems surprising at first, but can be explained by several points. In particular, the rapidly quenched structure can gain additional energy by rearrangement of silicon atoms during the now much slower quench. This can reduce the interface energy between silicon and silica as well as the internal energy of the silicon. At the same time, for the structure with a high degree of crystallinity, they pay an additional penalty due to the increase in the interface energy between crystalline silicon and amorphous silica compared to the interface between amorphous silicon and amorphous silica.

Figure 6.6 shows the interface energies for various types of manually constructed interfaces, as well as for the interfaces in the silicon monoxide structures. The interface energy between crystalline silicon and amorphous silica is the least favorable. This is not surprising, since within crystalline silicon the atoms are constrained in their arrangement at the interface. However, the internal energy of crystalline silicon is lower than in the amorphous state. Since silicon in its amorphous state can better adapt to the interface, the corresponding amorphous silicon–amorphous silica interface

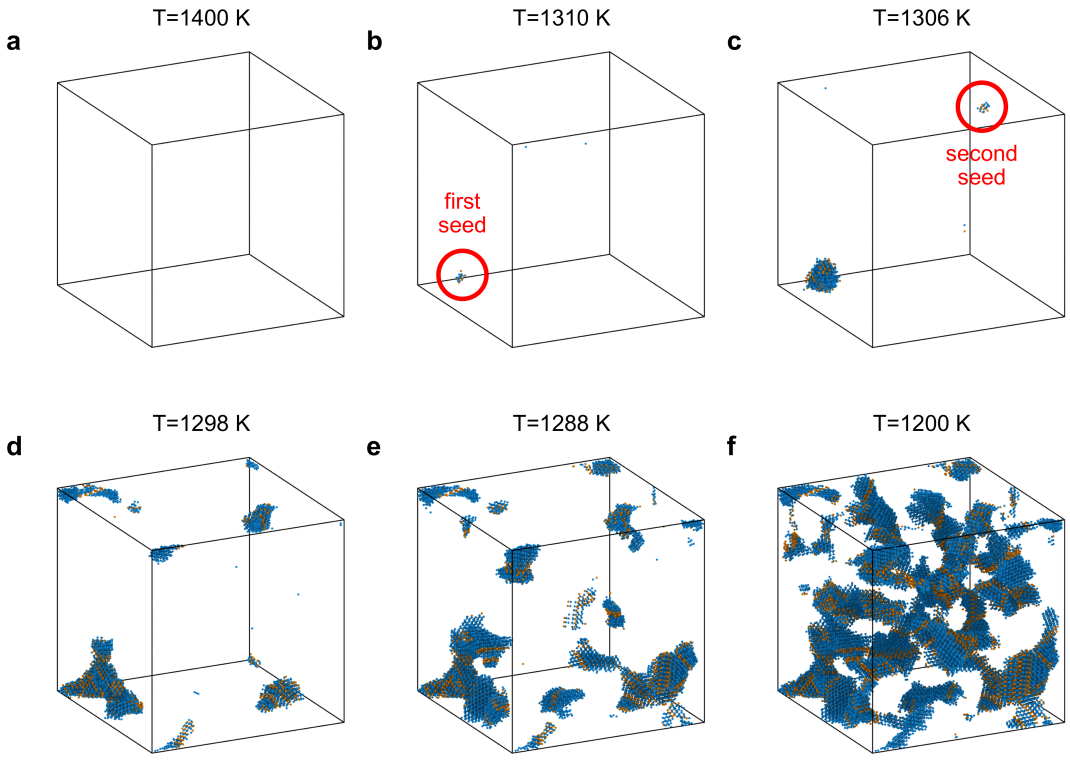

Figure 6.5: **Crystallization process of silicon in silicon monoxide.** Crystallization process from Figure 6.4a is shown in detail. Only silicon atoms identified as being in the cubic diamond structure (*blue*) or hexagonal diamond structure (*orange*) are shown. Structure identification is performed using PTM with a root mean square deviation of 0.1. (a) The structure is fully amorphous or liquid. (b) A first small silicon seed appears. (c) The first seed has grown while a second seed has appeared. (d-f) The crystalline silicon network continues to grow until it percolates the entire structure. Reproduced from Ref. 138. Original figure published under the CC-BY 4.0 license (https://creativecommons.org/licenses/by/4.0/).

has a lower interface energy. Another interface energy that is important during the crystallization process is the amorphous silicon–crystalline silicon interface energy. This interface energy is the lowest of these three types and its importance arises from its role during seed formation and growth. When the seed is formed within the amorphous silicon, a crystalline silicon–amorphous silicon interface is introduced in addition to the crystalline silicon–amorphous silica interface.

All the mentioned interface energies were determined from manually induced interfaces. However, these models do not account for proper interface relaxation since we only performed energetic minimization and a short low-temperature molecular dynamics (MD) simulation to adjust atomic positions. An example of better relaxed interfaces are the silicon monoxide models from Section 6.2. We can also calculate interface energies for these structures by using amorphous references created with equivalent quench

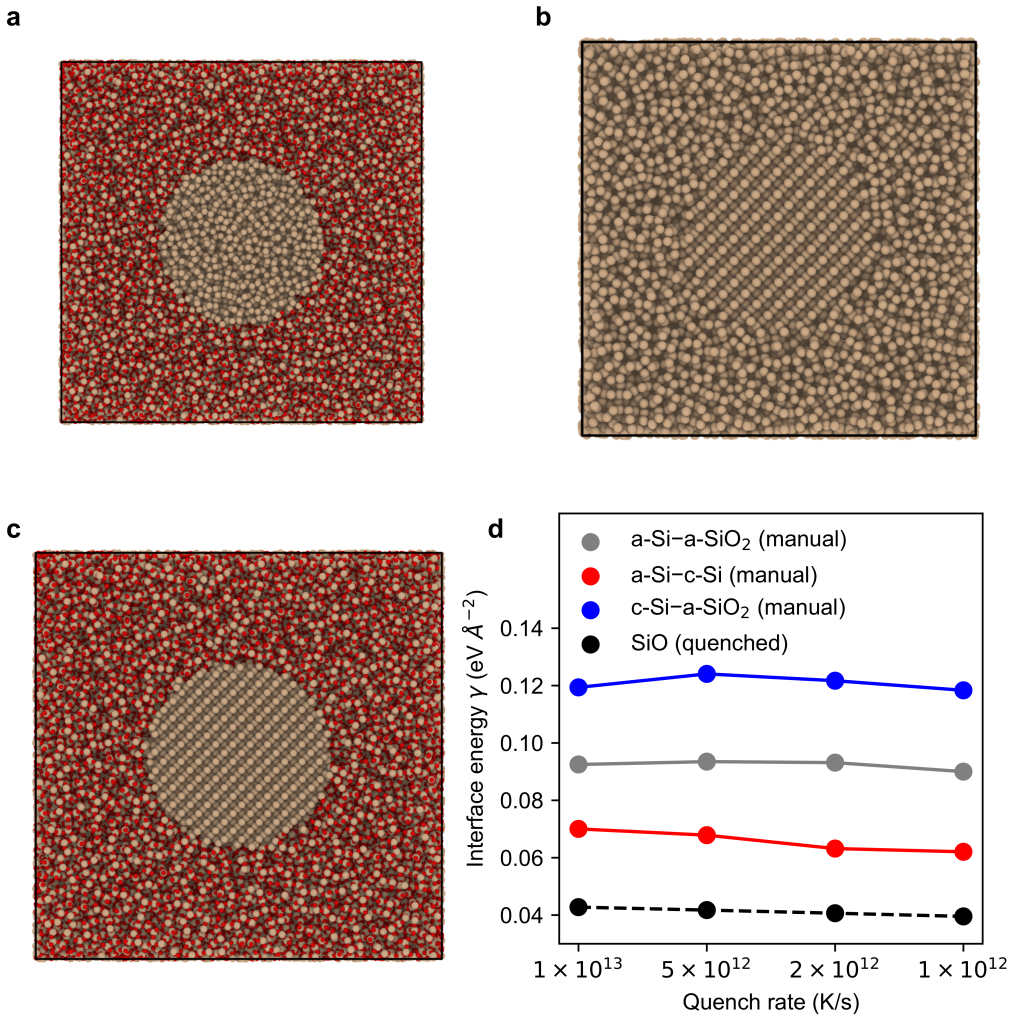

Figure 6.6: **Interface models of silicon and silica.** (a) Amorphous silicon inclusion in a silica matrix. (b) Amorphous silicon in a crystalline silicon matrix. (c) Crystalline silicon in amorphous silica. (d) Interface energies calculated from the models in (a-c) with amorphous structures generated at different quench rates. The interface models were manually constructed by slicing the crystalline and amorphous structures. Interface relaxation was performed by first, energetic optimization, second a thermal treatment by heating from 10 K to 300 K in 50 ps, holding for another 50 ps and cooling to 10 K for 50 ps, followed by a final energetic optimization. Interface energies for the silicon monoxide structures from Figure 6.2 are calculated using the corresponding interface areas and reference energies from amorphous structures quenched at the same quench rate. Reproduced from Ref. 138. Original figure published under the CC-BY 4.0 license (https://creativecommons.org/licenses/by/4.0/).

rates. These are also shown in Figure 6.6d. The corresponding interface energies are significantly lower compared to those from manually constructed amorphous silicon–amorphous silica interfaces. This can be explained by the better interface relaxation, but also by the fact that atoms can arrange themselves in such a way that only favorable interface arrangements occur.

One way to analyze the conditions under which silicon crystallizes in silicon monoxide is to make the following thermodynamic assessment. The energy differences between the crystalline state and the non-crystalline state are given by,

$$\Delta E = 4\pi r^2 \left(\gamma_{\text{c-Si–a-SiO}_2} - \gamma_{\text{a-Si–a-SiO}_2}\right) - \frac{4\pi r^3 (E_{\text{a-Si}} - E_{\text{c-Si}})}{3V_{\text{atom}}}. \tag{6.1}$$

For this equation, we assume that we have a spherical silicon inclusion with radius r in a silica matrix. Moreover, we only check whether it is more stable for the whole inclusion to be amorphous or crystalline and do not check for partially crystalline cases. $\gamma_{\text{c-Si–a-SiO}_2}$ is the interface energy between crystalline silicon and amorphous silica and $\gamma_{\text{a-Si–a-SiO}_2}$ is the interface energy between amorphous silicon and amorphous silica. $E_{\text{a-Si}}$ is the energy of amorphous silicon, $E_{\text{c-Si}}$ is the energy of crystalline silicon, and V_{atom} is the volume per atom. If we use the interface energies of the manually constructed interfaces from Figure 6.6 to calculate the energy differences, we obtain the curves shown in Figure 6.4j. Each curve corresponds to the interface energies from one quench rate. Although the interface energies are only rough approximations, we can see that the results agree quite well with our observations. For a radius below 9 Å crystallization is not favorable. However, for larger grains crystallization becomes favorable. This is exactly the same behavior as observed in our MD simulations, although the threshold is not exactly the same.

6.4 Summary

In this section, we first validated the ACE model for silicon and silica and showed that the DFT interface energies are well reproduced. We then performed melt-quench simulations for structures with the composition SiO. The resulting structural models show impressive agreement with experimental measurements of silicon monoxide. Grain size, X-ray structure factor and energetics are in excellent agreement with experimental measurements. We emphasize that these are the first realistic structural models of silicon monoxide on the scale of more than 100,000 atoms, and thus the first models capable of capturing the corresponding nanostructure. Finally, we annealed these structures to produce models with partially crystallized silicon. We observed that the silicon grains require a minimum size to observe crystallization and proposed a model to describe this behavior based on simple interface energies. Moreover, our MD simulations provided detailed insights into the crystallization process.

7 Summary

In this work, we have developed two machine learning interatomic potentials (MLIP) for the Si–O system and applied them to several problems. We started by creating a database for silica containing crystalline and amorphous structures as well as some clusters. The amorphous structures were generated using iterative 'batch' learning with a Gaussian approximation potential (GAP). Later, we changed the MLIP approach from GAP to moment tensor potentials (MTP) and atomic cluster expansion (ACE) potentials and subsequently extended the database. In particular, for the extension we used small-scale active learning approaches as they are currently implemented for MTPs, but also introduced a new large-scale active learning method. In this method we extract small-scale density functional theory (DFT) feasible cells from large-scale simulations using amorphous matrix embedding. We have used this approach to expand the database with additional data for high-pressure silica, silica surfaces, and most notably silicon-silica mixtures. The final potential is a non-linear ACE potential, which provides an excellent trade-off between accuracy and speed. We have applied the potential to the following cases.

7.1 Thermodynamic and structural aspects of silica

In this part, we have tested the ability of the MLIP to reproduce experimental properties of silica mainly related to thermodynamics of crystalline phases, but also to structural aspects of silica glass. In this respect, the MLIP is limited by two factors. The accuracy in reproducing the underlying DFT data and the accuracy of the exchange-correlation functional used for the training data. We show over a wide range of properties ranging from elastic constants, bulk moduli to phonon dispersion, that the potential is in excellent agreement with experiment and has higher accuracies than available classical interatomic potentials. However, the quality of the underlying strongly constrained and appropriately normed (SCAN) exchange-correlation functional is fully revealed in the calculation of the phase diagram. We have calculated the phase diagram of silica using two different methods, the quasi-harmonic approximation with frozen phonons and thermodynamic integration. In both cases the MLIPs show excellent qualitative and often even quantitative agreement. This is in strong contrast to the available classical interatomic potentials, which often fail to predict the correct stability fields. Although the phase diagram calculated by thermodynamic integration allows insights into phase

transitions even at high temperatures, it has certain limitations. These are the accuracy of the underlying DFT data as well as the influence of small errors (<1 meV) on the phase transition lines.

Besides the thermodynamics, we also investigated the ability of the MLIP to generate realistic atomic models of amorphous silica. We found that the MLIP significantly underestimated the first sharp diffraction peak (FSDP) of the X-ray structure factors. In contrast, this behavior was not observed for some classical interatomic potentials (CIP) such as the Carré, Horbach, Ispas, Kob (CHIK) potential. To overcome this issue and to obtain an accurate description of the energetics of the system, which are well described by the MLIP, we introduced a 'hybrid' approach. This approach uses first a slow CHIK quench followed by an equilibration with the MLIP, yielding amorphous structures in excellent agreement with the experiment.

7.2 High-pressure silica

For high pressure silica, we have started by validating the ACE potential for several stable and metastable high pressure phases. The potential reproduces the DFT results for these phases extremely well, even for phases that are not part of the training database. Moreover, the phase transition pressures for high pressure transitions agree well with experimental measurements. We then applied the ACE potential to shock simulations of amorphous silica and quartz. By using a new machine-learning based structure identification model, we are able to obtain detailed insights into the processes during shock. We are able to observe that amorphous silica transforms to stishovite within the shock simulations. However, instead of a direct transformation to stishovite, an intermediate phase with the defective nickel arsenide (d-NiAs) structure is observed. This phase has the same hexagonal close-packed (HCP) oxygen sublattice as stishovite, but silicon atoms are randomly distributed in octahedral voids. Additionally, we observed the same d-NiAs structure in shock simulations of quartz, but no formation of stishovite. Both results are in excellent agreement with experimental observations and provide new insights into the crystallization process of silica under high pressure, e.g. by an initial ordering of the oxygen atoms followed by an ordering of the silicon atoms if the time scales are sufficient. Finally, we tried to understand the formation of rosiaite-structured silica observed in dynamic diamond anvil cell compression experiments. We found that this phase can only occur if quartz is not only compressed along the z-axis, but if additional strain perpendicular to the compression direction is applied. If this strain is not applied, quartz prefers to amorphize.

7.3 Silicon monoxide

The interface between silicon and silica is essential for understanding the structural properties of silicon monoxide. Therefore, we first investigated the ability of the ACE potential to describe interface energies. We found good agreement between the DFT and ACE interface energies. We then performed melt-quench simulations with different

quench-rates to generate structural models of silicon monoxide. These models are in excellent agreement with experimental observations in terms of grain size, X-ray structure factor, and energetics. By modifying the quench rate, structural properties can be tuned. Moreover, we show that the ACE behaves much better than available CIPs, which fail for this task. Using the generated structural models, we performed annealing simulations to crystallize the silicon within the silicon monoxide structures. Indeed, for the models with larger silicon grain sizes this approach works successfully and significant crystallites can be seen. However, for the models with too small silicon grains no or almost no crystallization is observed. To understand this behavior we used a thermodynamically based model. Based on interface energies, we evaluated under which grain sizes it is favorable for the silicon to crystallize and under which conditions it prefers to remain in the amorphous state and found that a grain radius of more than 9 Å seems to be necessary for crystallization.

Outlook 8

Although this thesis provided significant achievements in understanding the complex structure of silicon monoxide and the shock behavior of silica under pressure, there are still unsolved questions. In the following we will discuss some of these and possible future work.

8.1 More accurate machine-learning potentials

All our current machine learning interatomic potentials (MLIP) are short-ranged only. However, since silica is an ionic system, long-range interactions may be necessary for an even more accurate description. This could solve the issue of the low height of the first sharp diffraction peak (FSDP) in the structure factor (see Section 4.3). In the case of pure MLIPs, equivariant message-passing graph neural networks have become increasingly popular in recent years.[324,325] These potentials incorporate semi-local information into the energy computation by representing the atoms as a graph network and allowing messages to pass over larger distances. However, even these potentials have a cutoff that limits the interaction range.

Other approaches include the explicit treatment of charges such as the 3rd generation and 4th generation neural network potentials (NNP) by Behler and coworkers.[234,257] The advantage of these models is that they can actually describe the differences in charge states of silicon within pure silicon and silica. Moreover, there are now graph neural networks that directly incorporate charge.[326] Using these approaches with the current database could further increase the accuracy of the potential compared to the corresponding density functional theory (DFT) data and allow even better quantitative results.

Finally, another option would be to improve the quality of the underlying training data. Currently, the strongly constrained and appropriately normed (SCAN) exchange-correlation functional is probably an excellent choice for silica. However, it is only an approximation of the exact potential energy surface. In the future, it may be possible to generate a more accurate database using machine-learned exchange-correlation functionals.[327]

8.2 High-pressure simulations

Shock simulations of quartz and amorphous silica have provided significant insight into the behavior of silica at high pressures. However, there are other polymorphs of silica that are of interest under compression. Cristobalite shows a very interesting behavior, as it undergoes several phase transitions to cristobalite II,[328] cristobalite X-I,[329,330] and seifertite.[329,331] Other experiments even suggested that seifertite appears at a pressure of 11 GPa,[332] well below its stability pressure suggesting that there is a direct transition path. Molecular dynamics (MD) simulations of this compression could be extremely helpful in understanding possible transitions. Finally, they could further help to understand why seifertite has been observed in meteorites that are thought to have experienced shock pressures lower than those required for seifertite formation.[332–336]

For a better understanding of the Earth's interior the MLIP could also be extended to include other elements. For example, both iron and magnesium may be relevant, and first interatomic potentials for these systems (e.g. Fe–Si–O[337] and Mg–Si–O[338]) have been developed. Nevertheless, a further extension for a complete description of the system to including impurities and defects could be highly interesting.

8.3 Silicon monoxide

In this work, we presented for the first time atomic scale models of silicon monoxide that take into account the nanostructure of this material. We found that by using different quench rates, we can generate different nanostructures with different grain sizes. It would be very interesting to reproduce this experimentally by using different deposition rates and temperature gradients. If this were the case, it would be a first step towards tuning the properties of silicon monoxide.

Building on this, since silicon monoxide is a promising material for battery applications, extending the potential to describe lithium is a promising step. Understanding the behavior of lithium, such as the diffusion, in silicon monoxide could further advance the use of this material in batteries. Moreover, by combining simulation studies and experiments, it may be possible to tune the grain size for optimal use in batteries.

Curriculum Vitæ

Research Experience

since 01/2021 — Scientific staff member (*Wissenschaftlicher Mitarbeiter*)
Materials Modelling Group
Prof. Dr. rer. nat. Karsten Albe,
Technische Universität Darmstadt, Germany

04/2022 - 10/2022 — Visiting scientist
Deringer group
University of Oxford, UK

03/2020 - 09/2020 (mainly virtual)
Visiting scientist
Deringer group
University of Oxford, UK

Education

01/2021 — Master of Science in Materials Science
Technische Universität Darmstadt, Germany

10/2018 — Bachelor of Science in Materials Science
Technische Universität Darmstadt, Germany

06/2015 — Secondary education (*Abitur*)
Christian-Wirth-Schule, Usingen, Germany

Peer Reviewed Articles

L. C. Erhard, J. Rohrer, K. Albe, and V. L. Deringer, *A machine-learned interatomic potential for silica and its relation to empirical models*, npj Computational Materials 8, 1–12 (2022)

L. C. Erhard, J. Rohrer, K. Albe, and V. L. Deringer, *Modelling atomic and nanoscale structure in the silicon–oxygen system through active machine learning*, Nature Communications 15, 1927 (2024)

L. C. Erhard, D. Utt, A. J. Klomp, and K. Albe, *Crystal structure identification with 3D convolutional neural networks with application to high-pressure phase transitions in SiO_2*, Modelling and Simulation in Materials Science and Engineering 32, 065029 (2024)

Submitted Articles

L. C. Erhard, C. Otzen, J. Rohrer, C. Prescher, and K. Albe, *Understanding phase transitions of α-quartz under high-pressures by machine-learning driven atomistic simulations*, submitted, arXiv preprint arXiv:2406.17676 (2024)

Oral Presentations at International Conferences

09/2023 NHR Conference, Berlin, Germany, '*Unraveling the atomic structure of silicon monoxide using high-performance computing and machine-learning*' L. C. Erhard, J. Rohrer, K. Albe, V. L. Deringer

09/2023 GAP/(M)ACE User Meeting, Warwick, United Kingdom '*Modelling atomic and nanoscale structure in the silicon-oxygen system through active machine-learning*' L. C. Erhard, J. Rohrer, K. Albe, V. L. Deringer

03/2023 DPG Spring Meeting, Dresden, Germany '*A machine-learned interatomic potential for silica and mixed silica-silicon systems*' L. C. Erhard, J. Rohrer, K. Albe, V. L. Deringer

10/2022 MMM 10, Baltimore, United States of America '*Benchmarking of different machine-learning interatomic potential approaches for silica*' L. C. Erhard, J. Rohrer, K. Albe, V. L. Deringer

09/2022 DPG Spring Meeting, Dresden, Germany '*A machine-learned interatomic potential for crystalline and amorphous silica*' L. C. Erhard, J. Rohrer, K. Albe, V. L. Deringer

Bibliography

[1] R. L. Rudnick and S. Gao, *4.1 - Composition of the Continental Crust*, Treatise on Geochemistry (Second Edition) (H. D. Holland and K. K. Turekian, eds.), Elsevier, Oxford, January 2014, pp. 1–51.

[2] P. J. Heaney, *Chapter 1. Structure and Chemistry of the Low-Pressure Silica Polymorphs*, Silica: Physical Behavior, Geochemistry, and Materials Applications (P. J. Heaney, C. T. Prewitt, and G. V. Gibbs, eds.), De Gruyter, 1994, pp. 1–40.

[3] H. B. Walther, *Quality Requirements of Quartz Sand in the Building Industry*, Quartz: Deposits, Mineralogy and Analytics (J. Götze and R. Möckel, eds.), Springer, Berlin, Heidelberg, 2012, pp. 53–70.

[4] A. Soleimani Dorcheh and M. Abbasi, *Silica aerogel; synthesis, properties and characterization*, Journal of Materials Processing Technology 199, 10–26 (2008).

[5] P. M. Piccione, C. Laberty, S. Yang, M. A. Camblor, A. Navrotsky, and M. E. Davis, *Thermochemistry of Pure-Silica Zeolites*, The Journal of Physical Chemistry B 104, 10001–10011 (2000).

[6] J. Weitkamp, *Zeolites and catalysis*, Solid State Ionics 131, 175–188 (2000).

[7] P. Venuto and E. Habib, *Fluid catalytic cracking with zeolite catalysts*, Chemical Industries, M. Dekker, 1979.

[8] P. Swenson, B. Tanchuk, E. Bastida, W. An, and S. M. Kuznicki, *Water desalination and de-oiling with natural zeolite membranes — Potential application for purification of SAGD process water*, Desalination 286, 442–446 (2012).

[9] W. G. Cady, *Piezoelectricity: An introduction to the theory and applications of electromechanical phenomena in crystals*, 1. ed., 2. impr. ed., International Series in Pure and Applied Physics, McGraw-Hill, New York [u.a.], 1946.

[10] W. A. Marrison, *The evolution of the quartz crystal clock*, The Bell System Technical Journal 27, 510–588 (1948).

[11] J. S. Danel and G. Delapierre, *Quartz: A material for microdevices*, Journal of Micromechanics and Microengineering 1, 187–198 (1991).

[12] R. K. Ratnesh, A. Goel, G. Kaushik, H. Garg, Chandan, M. Singh, and B. Prasad, *Advancement and challenges in MOSFET scaling*, Materials Science in Semiconductor Processing 134, 106002 (2021).

[13] A. Jain, S. P. Ong, G. Hautier, W. Chen, W. D. Richards, S. Dacek, S. Cholia, D. Gunter, D. Skinner, G. Ceder, and K. A. Persson, *Commentary: The Materials Project: A materials genome approach to accelerating materials innovation*, APL Materials 1, 011002 (2013).

[14] A. P. Bartók, R. Kondor, and G. Csányi, *On representing chemical environments*, Phys. Rev. B 87, 184115 (2013).

[15] L. McInnes, J. Healy, N. Saul, and L. Großberger, *UMAP: Uniform Manifold Approximation and Projection*, Journal of Open Source Software 3, 861 (2018).

[16] V. L. Deringer, M. A. Caro, and G. Csányi, *A general-purpose machine-learning force field for bulk and nanostructured phosphorus*, Nature Communications 11, 5461 (2020).

[17] V. Swamy, S. K. Saxena, B. Sundman, and J. Zhang, *A thermodynamic assessment of silica phase diagram*, Journal of Geophysical Research: Solid Earth 99, 11787–11794 (1994).

[18] A. K. A. Pryde and M. T. Dove, *On the Sequence of Phase Transitions in Tridymite*, Physics and Chemistry of Minerals 26, 171–179 (1998).

[19] U. Müller, *Inorganic Structural Chemistry*, 1 ed., John Wiley & Sons, Ltd, 2006.

[20] A. J. Leadbetter, T. W. Smith, and A. F. Wright, *Structure of High Cristobalite*, Nature Physical Science 244, 125–126 (1973).

[21] K. Kihara, *Thermal change in unit-cell dimensions, and a hexagonal structure of tridymite*, Zeitschrift für Kristallographie - Crystalline Materials 148, 237–254 (1978).

[22] I. P. Swainson, M. T. Dove, and D. C. Palmer, *Infrared and Raman spectroscopy studies of the α–β phase transition in cristobalite*, Physics and Chemistry of Minerals 30, 353–365 (2003).

[23] R. F. D. Dombal and M. A. Carpenter, *High-temperature phase transitions in Steinbach tridymite*, European Journal of Mineralogy 5, 607–622 (1993).

[24] D. Cellai, M. A. Carpenter, B. Wruck, and E. K. H. Salje, *Characterization of high-temperature phase transitions in single crystals of Steinbach tridymite*, American Mineralogist 79, 606–614 (1994).

[25] H. Graetsch and O. W. Flörke, *X-ray powder diffraction patterns and phase relationship of tridymite modifications*, Zeitschrift für Kristallographie - Crystalline Materials 195, 31–48 (1991).

[26] L. Coes, *A New Dense Crystalline Silica*, Science 118, 131–132 (1953).

[27] S. M. Stishov and S. V. Popova, *A new dense modification of silica*, Geokhimiya 10, 837–839 (1961).

[28] E. C. T. Chao, E. M. Shoemaker, and B. M. Madsen, *First Natural Occurrence of Coesite*, Science 132, 220–222 (1960).

[29] E. C. T. Chao, J. J. Fahey, J. Littler, and D. J. Milton, *Stishovite, SiO_2, a very high pressure new mineral from Meteor Crater, Arizona*, Journal of Geophysical Research (1896-1977) 67, 419–421 (1962).

[30] S. R. Bohlen and A. L. Boettcher, *The quartz ⥋ coesite transformation: A precise determination and the effects of other components*, Journal of Geophysical Research: Solid Earth 87, 7073–7078 (1982).

[31] M. Akaogi, H. Yusa, K. Shiraishi, and T. Suzuki, *Thermodynamic properties of α-quartz, coesite, and stishovite and equilibrium phase relations at high pressures and high temperatures*, Journal of Geophysical Research: Solid Earth 100, 22337–22347 (1995).

[32] K. J. Kingma, R. E. Cohen, R. J. Hemley, and H.-k. Mao, *Transformation of stishovite to a denser phase at lower-mantle pressures*, Nature 374, 243–245 (1995).

[33] Y. Tsuchida and T. Yagi, *A new, post-stishovite highpressure polymorph of silica*, Nature 340, 217–220 (1989).

[34] R. A. Fischer, A. J. Campbell, B. A. Chidester, D. M. Reaman, E. C. Thompson, J. S. Pigott, V. B. Prakapenka, and J. S. Smith, *Equations of state and phase boundary for stishovite and $CaCl_2$-type SiO_2*, American Mineralogist 103, 792–802 (2018).

[35] M. Murakami, K. Hirose, S. Ono, and Y. Ohishi, *Stability of $CaCl_2$-type and α-PbO_2-type SiO_2 at high pressure and temperature determined by in-situ X-ray measurements*, Geophysical Research Letters 30 (2003).

[36] Y. Kuwayama, K. Hirose, N. Sata, and Y. Ohishi, *The Pyrite-Type High-Pressure Form of Silica*, Science 309, 923–925 (2005).

[37] W. H. Zachariasen, *The Atomic Arrangement in Glass*, Journal of the American Chemical Society 54, 3841–3851 (1932).

[38] B. E. Warren, *The Diffraction of X-Rays in Glass*, Physical Review 45, 657–661 (1934).

[39] F. Ordway, *Condensation model producing crystalline or amorphous tetrahedral networks*, Science 143, 800–801 (1964).

[40] D. L. Evans and S. V. King, *Random Network Model of Vitreous Silica*, Nature 212, 1353–1354 (1966).

[41] R. J. Bell and P. Dean, *Properties of Vitreous Silica: Analysis of Random Network Models*, Nature 212, 1354–1356 (1966).

[42] D. A. Keen and R. L. McGreevy, *Structural modelling of glasses using reverse Monte Carlo simulation*, Nature 344, 423–425 (1990).

[43] P. Vashishta, R. K. Kalia, J. P. Rino, and I. Ebbsjö, *Interaction potential for SiO_2 : A molecular-dynamics study of structural correlations*, Phys. Rev. B 41, 12197–12209 (1990).

[44] R. G. Della Valle and H. C. Andersen, *Molecular dynamics simulation of silica liquid and glass*, The Journal of Chemical Physics 97, 2682–2689 (1992).

[45] A. Nakano, R. K. Kalia, and P. Vashishta, *First sharp diffraction peak and intermediate-range order in amorphous silica: Finite-size effects in molecular dynamics simulations*, Journal of Non-Crystalline Solids 171, 157–163 (1994).

[46] S. R. Elliott, *Medium-range structural order in covalent amorphous solids*, Nature 354, 445–452 (1991).

[47] S. R. Elliott, *Origin of the first sharp diffraction peak in the structure factor of covalent glasses*, Physical Review Letters 67, 711–714 (1991).

[48] P. H. Gaskell and D. J. Wallis, *Medium-range order in silica, the canonical network glass*, Physical Review Letters 76, 66–69 (1996).

[49] A. C. Wright, R. N. Sinclair, and A. J. Leadbetter, *Effect of preparation method on the structure of amorphous solids in the system As–S*, Journal of Non-Crystalline Solids 71, 295–302 (1985).

[50] A. C. Wright, *Neutron scattering from vitreous silica. V. The structure of vitreous silica: What have we learned from 60 years of diffraction studies?*, Journal of Non-Crystalline Solids 179, 84–115 (1994).

[51] S. Sato, M. Miyakawa, T. Taniguchi, Y. Onodera, K. Ohara, K. Ikeda, N. Kitamura, Y. Idemoto, and S. Kohara, *Synthesis of hyperordered permanently densified silica glasses by hot compression above the glass transition temperature*, Journal of the Ceramic Society of Japan advpub, 24013 (2024).

[52] C. Prescher, V. B. Prakapenka, J. Stefanski, S. Jahn, L. B. Skinner, and Y. Wang, *Beyond sixfold coordinated Si in SiO_2 glass at ultrahigh pressures*, Proceedings of the National Academy of Sciences 114, 10041–10046 (2017).

[53] Y. Kono, Y. Shu, C. Kenney-Benson, Y. Wang, and G. Shen, *Structural Evolution of SiO_2 Glass with Si Coordination Number Greater than 6*, Physical Review Letters 125, 205701 (2020).

[54] M. Murakami, S. Kohara, N. Kitamura, J. Akola, H. Inoue, A. Hirata, Y. Hiraoka, Y. Onodera, I. Obayashi, J. Kalikka, N. Hirao, T. Musso, A. S. Foster, Y. Idemoto, O. Sakata, and Y. Ohishi, *Ultrahigh-pressure form of SiO_2 glass with dense pyrite-type crystalline homology*, Physical Review B 99, 045153 (2019).

[55] F. Langenhorst, *Shock experiments on pre-heated α- and β-quartz: II. X-ray and TEM investigations*, Earth and Planetary Science Letters 128, 683–698 (1994).

[56] B. F. Bohor, P. J. Modreski, and E. E. Foord, *Shocked Quartz in the Cretaceous-Tertiary Boundary Clays: Evidence for a Global Distribution*, Science 236, 705–709 (1987).

[57] L. W. Alvarez, W. Alvarez, F. Asaro, and H. V. Michel, *Extraterrestrial Cause for the Cretaceous-Tertiary Extinction*, Science 208, 1095–1108 (1980).

[58] A. A. Chiarenza, A. Farnsworth, P. D. Mannion, D. J. Lunt, P. J. Valdes, J. V. Morgan, and P. A. Allison, *Asteroid impact, not volcanism, caused the end-Cretaceous dinosaur extinction*, Proceedings of the National Academy of Sciences 117, 17084–17093 (2020).

[59] E.-R. Carl, U. Mansfeld, H.-P. Liermann, A. Danilewsky, F. Langenhorst, L. Ehm, G. Trullenque, and T. Kenkmann, *High-pressure phase transitions of α-quartz under nonhydrostatic dynamic conditions: A reconnaissance study at PETRA III*, Meteoritics & Planetary Science 52, 1465–1474 (2017).

[60] C. Otzen, H.-P. Liermann, and F. Langenhorst, *Evidence for a rosiaite-structured high-pressure silica phase and its relation to lamellar amorphization in quartz*, Nature Communications 14, 606 (2023).

[61] L. E. McNeil and M. Grimsditch, *Pressure-amorphized SiO_2 α-quartz: An anisotropic amorphous solid*, Physical Review Letters 68, 83–85 (1992).

[62] K. J. Kingma, C. Meade, R. J. Hemley, H.-k. Mao, and D. R. Veblen, *Microstructural Observations of α-Quartz Amorphization*, Science 259, 666–669 (1993).

[63] R. J. Hemley, A. P. Jephcoat, H. K. Mao, L. C. Ming, and M. H. Manghnani, *Pressure-induced amorphization of crystalline silica*, Nature 334, 52–54 (1988).

[64] S. J. Tracy, S. J. Turneaure, and T. S. Duffy, *Structural response of α-quartz under plate-impact shock compression*, Science Advances 6, eabb3913 (2020).

[65] L. C. Erhard, C. Otzen, J. Rohrer, C. Prescher, and K. Albe, *Understanding phase transitions of α-quartz under high-pressures by machine-learning driven atomistic simulations*, submitted, arXiv preprint arXiv:2406.17676 (2024).

[66] K. J. Kingma, R. J. Hemley, H.-k. Mao, and D. R. Veblen, *New high-pressure transformation in α-quartz*, Physical Review Letters 70, 3927–3930 (1993).

[67] K. J. Kingma, H.-K. Mao, and R. J. Hemley, *Synchrotron X-ray diffraction of SiO_2 to multimegabar pressures*, High Pressure Research 14, 363–374 (1996).

[68] N. Choudhury and S. L. Chaplot, Ab Initio *studies of phonon softening and high-pressure phase transitions of α -quartz SiO_2*, Physical Review B 73, 094304 (2006).

[69] R. Martoňák, D. Donadio, A. R. Oganov, and M. Parrinello, *Crystal structure transformations in SiO_2 from classical and ab initio metadynamics*, Nature Materials 5, 623–626 (2006).

[70] C. Campañá, M. H. Müser, J. S. Tse, D. Herzbach, and P. Schöffel, *Irreversibility of the pressure-induced phase transition of quartz and the relation between three hypothetical post-quartz phases*, Physical Review B 70, 224101 (2004).

[71] J. Haines, J. M. Léger, F. Gorelli, and M. Hanfland, *Crystalline Post-Quartz Phase in Silica at High Pressure*, Physical Review Letters 87, 155503 (2001).

[72] D. M. Teter, R. J. Hemley, G. Kresse, and J. Hafner, *High Pressure Polymorphism in Silica*, Physical Review Letters 80, 2145–2148 (1998).

[73] T. Tsuchiya and S. Nakagawa, *A new high-pressure structure of SiO_2 directly converted from α-quartz under nonhydrostatic compression*, Journal of Physics: Condensed Matter 34, 304003 (2022).

[74] C. Otzen, H.-P. Liermann, and F. Langenhorst, *A New Mechanism for Stishovite Formation During Rapid Compression of Quartz and Implications for Asteroid Impacts*, Journal of Geophysical Research: Planets 129, e2023JE008126 (2024).

[75] L.-G. Liu, W. A. Bassett, and J. Sharry, *New high-pressure modifications of GeO_2 and SiO_2*, Journal of Geophysical Research: Solid Earth 83, 2301–2305 (1978).

[76] T. Sekine, M. Akaishi, and N. Setaka, *Fe_2N-type SiO_2 from shocked quartz*, Geochimica et Cosmochimica Acta 51, 379–381 (1987).

[77] V. P. Prakapenka, G. Shen, L. S. Dubrovinsky, M. L. Rivers, and S. R. Sutton, *High pressure induced phase transformation of SiO_2 and GeO_2: Difference and similarity*, Journal of Physics and Chemistry of Solids 65, 1537–1545 (2004).

[78] S. J. Tracy, S. J. Turneaure, and T. S. Duffy, *In situ X-Ray Diffraction of Shock-Compressed Fused Silica*, Physical Review Letters 120, 135702 (2018).

[79] J. S. Tse, D. D. Klug, and Y. Le Page, *Novel high pressure phase of silica*, Physical Review Letters 69, 3647–3649 (1992).

[80] B. W. H. van Beest, G. J. Kramer, and R. A. van Santen, *Force fields for silicas and aluminophosphates based on* ab initio *calculations*, Phys. Rev. Lett. 64, 1955–1958 (1990).

[81] Q. Y. Hu, J.-F. Shu, W. G. Yang, C. Park, M. W. Chen, T. Fujita, H.-K. Mao, and H. W. Sheng, *Stability limits and transformation pathways of α -quartz under high pressure*, Physical Review B 95, 104112 (2017).

[82] J. Badro, D. M. Teter, R. T. Downs, P. Gillet, R. J. Hemley, and J.-L. Barrat, *Theoretical study of a five-coordinated silica polymorph*, Physical Review B 56, 5797–5806 (1997).

[83] R. M. Wentzcovitch, C. Da Silva, J. R. Chelikowsky, and N. Binggeli, *A New Phase and Pressure Induced Amorphization in Silica*, Physical Review Letters 80, 2149–2152 (1998).

[84] H. Schnöckel and R. Köppe, *Reactions with Matrix-Isolated SiO Molecules*, Silicon Chemistry, John Wiley & Sons, Ltd, 2003, pp. 20–32.

[85] D. Poat, *Properties of pulse-deposited thin-film silicon monoxide capacitors*, Thin Solid Films 4, 123–136 (1969).

[86] C. G. Granqvist and A. Hjortsberg, *Surfaces for radiative cooling: Silicon monoxide films on aluminum*, Applied Physics Letters 36, 139–141 (1980).

[87] G. Hass, *Preparation, Structure, and Applications of Thin Films of Silicon Monoxide and Titanium Dioxide*, Journal of the American Ceramic Society 33, 353–360 (1950).

[88] Z. Liu, Q. Yu, Y. Zhao, R. He, M. Xu, S. Feng, S. Li, L. Zhou, and L. Mai, *Silicon oxides: A promising family of anode materials for lithium-ion batteries*, Chemical Society Reviews 48, 285–309 (2019).

[89] J. Yang, Y. Takeda, N. Imanishi, C. Capiglia, J. Y. Xie, and O. Yamamoto, *SiO_x-based anodes for secondary lithium batteries*, Solid State Ionics 152–153, 125–129 (2002).

[90] L. Zhang, J. Deng, L. Liu, W. Si, S. Oswald, L. Xi, M. Kundu, G. Ma, T. Gemming, S. Baunack, F. Ding, C. Yan, and O. G. Schmidt, *Hierarchically Designed SiO_x/SiO_y Bilayer Nanomembranes as Stable Anodes for Lithium Ion Batteries*, Advanced Materials 26, 4527–4532 (2014).

[91] C. F. Mabery, *The composition of certain products from the Cowles electrical furnace*, Journal of the Franklin Institute 122, 271–274 (1886).

[92] G. W. Brady, *A Study of Amorphous SiO*, The Journal of Physical Chemistry 63, 1119–1120 (1959).

[93] R. J. Temkin, *An analysis of the radial distribution function of SiO_x*, Journal of Non-Crystalline Solids 17, 215–230 (1975).

[94] H. R. Philipp, *Optical and bonding model for non-crystalline SiO_x and SiO_xN_y materials*, Journal of Non-Crystalline Solids 8–10, 627–632 (1972).

[95] H. N. Potter, *Silicon Monoxide*, Transcript Electrochemical Society 12, 191–214 (1907).

[96] S. C. H. Lin and M. Joshi, *Structure of Silicon Monoxide*, Journal of The Electrochemical Society 116, 1740 (1969).

[97] M. V. Coleman and D. J. D. Thomas, *The Structure of Silicon Oxide Films*, physica status solidi (b) 22, 593–602 (1967).

[98] R. Engelke, Th. Roy, H.-G. Neumann, and K. Hübner, *Chemical bond and related properties of SiO_2*, Physica Status Solidi (a) 65, 271–280 (1981).

[99] J. A. Yasaitis and R. Kaplow, *Structure of Amorphous Silicon Monoxide*, Journal of Applied Physics 43, 995–1000 (1972).

[100] A. Hohl, T. Wieder, P. van Aken, T. Weirich, G. Denninger, M. Vidal, S. Oswald, C. Deneke, J. Mayer, and H. Fuess, *An interface clusters mixture model for the structure of amorphous silicon monoxide (SiO)*, Journal of Non-Crystalline Solids 320, 255–280 (2003).

[101] K. Schulmeister and W. Mader, *TEM investigation on the structure of amorphous silicon monoxide*, Journal of Non-Crystalline Solids 320, 143–150 (2003).

[102] A. Hirata, S. Kohara, T. Asada, M. Arao, C. Yogi, H. Imai, Y. Tan, T. Fujita, and M. Chen, *Atomic-scale disproportionation in amorphous silicon monoxide*, Nature Communications 7, 11591 (2016).

[103] S. C. Jung, H.-J. Kim, J.-H. Kim, and Y.-K. Han, *Atomic-Level Understanding toward a High-Capacity and High-Power Silicon Oxide (SiO) Material*, The Journal of Physical Chemistry C 120, 886–892 (2016).

[104] J. Moon, *Tailoring the oxygen content in lithiated silicon oxide for lithium-ion batteries*, International Journal of Energy Research 45, 7315–7325 (2021).

[105] C.-Y. Chou and G. S. Hwang, *Lithiation Behavior of Silicon-Rich Oxide ($SiO_{1/3}$): A First-Principles Study*, Chemistry of Materials 25, 3435–3440 (2013).

[106] S. Tsuneyuki, M. Tsukada, H. Aoki, and Y. Matsui, *First-Principles Interatomic Potential of Silica Applied to Molecular Dynamics*, Phys. Rev. Lett. 61, 869–872 (1988).

[107] E. Flikkema and S. Bromley, *A new interatomic potential for nanoscale silica*, Chemical Physics Letters 378, 622–629 (2003).

[108] A. Carré, J. Horbach, S. Ispas, and W. Kob, *New fitting scheme to obtain effective potential from Car-Parrinello molecular-dynamics simulations: Application to silica*, EPL (Europhysics Letters) 82, 17001 (2008).

[109] J. Q. Broughton, C. A. Meli, P. Vashishta, and R. K. Kalia, *Direct atomistic simulation of quartz crystal oscillators: Bulk properties and nanoscale devices*, Phys. Rev. B 56, 611–618 (1997).

[110] K. de Boer, A. Jansen, and R. van Santen, *Ab initio approach to the development of interatomic potentials for the shell model of silica polymorphs*, Chemical Physics Letters 223, 46–53 (1994).

[111] P. Tangney and S. Scandolo, *An* ab initio *parametrized interatomic force field for silica*, The Journal of Chemical Physics 117, 8898–8904 (2002).

[112] L. Huang and J. Kieffer, *Molecular dynamics study of cristobalite silica using a charge transfer three-body potential: Phase transformation and structural disorder*, The Journal of Chemical Physics 118, 1487–1498 (2003).

[113] E. Demiralp, T. Çağin, and W. A. Goddard, *Morse Stretch Potential Charge Equilibrium Force Field for Ceramics: Application to the Quartz-Stishovite Phase Transition and to Silica Glass*, Phys. Rev. Lett. 82, 1708–1711 (1999).

[114] T.-R. Shan, B. D. Devine, J. M. Hawkins, A. Asthagiri, S. R. Phillpot, and S. B. Sinnott, *Second-generation charge-optimized many-body potential for Si/SiO_2 and amorphous silica*, Physical Review B 82, 235302 (2010).

[115] A. Yasukawa, *Using An Extended Tersoff Interatomic Potential to Analyze The Static-Fatigue Strength of SiO_2 under Atmospheric Influence*, JSME international journal. Ser. A, Mechanics and material engineering 39, 313–320 (1996).

[116] J. Yu, S. B. Sinnott, and S. R. Phillpot, *Charge optimized many-body potential for the Si/SiO_2 system*, Physical Review B 75, 085311 (2007).

[117] S. Munetoh, T. Motooka, K. Moriguchi, and A. Shintani, *Interatomic potential for Si–O systems using Tersoff parameterization*, Computational Materials Science 39, 334–339 (2007).

[118] T. Watanabe, D. Yamasaki, K. Tatsumura, and I. Ohdomari, *Improved interatomic potential for stressed Si, O mixed systems*, Applied Surface Science 234, 207–213 (2004).

[119] T. Watanabe, H. Fujiwara, H. Noguchi, T. Hoshino, and I. Ohdomari, *Novel Interatomic Potential Energy Function for Si, O Mixed Systems*, Japanese Journal of Applied Physics 38, L366–L369 (1999).

[120] A. C. T. van Duin, A. Strachan, S. Stewman, Q. Zhang, X. Xu, and W. A. Goddard, *ReaxFFSiO Reactive Force Field for Silicon and Silicon Oxide Systems*, The Journal of Physical Chemistry A 107, 3803–3811 (2003).

[121] B. P. Feuston and S. H. Garofalini, *Empirical three-body potential for vitreous silica*, The Journal of Chemical Physics 89, 5818–5824 (1988).

[122] Z. Jiang and R. A. Brown, *Modelling oxygen defects in silicon crystals using an empirical interatomic potential*, Chemical Engineering Science 49, 2991–3000 (1994).

[123] A. Pedone, G. Malavasi, M. C. Menziani, A. N. Cormack, and U. Segre, *A New Self-Consistent Empirical Interatomic Potential Model for Oxides, Silicates, and Silica-Based Glasses*, J. Phys. Chem. B 110, 11780–11795 (2006).

[124] J. R. Kermode, S. Cereda, P. Tangney, and A. De Vita, *A first principles based polarizable O(N) interatomic force field for bulk silica*, The Journal of Chemical Physics 133, 094102 (2010).

[125] S. Trillot, J. Lam, S. Ispas, A. K. A. Kandy, M. E. Tuckerman, N. Tarrat, and M. Benoit, *Elaboration of a neural-network interatomic potential for silica glass and melt*, Computational Materials Science 236, 112848 (2024).

[126] I. A. Balyakin, S. V. Rempel, R. E. Ryltsev, and A. A. Rempel, *Deep machine learning interatomic potential for liquid silica*, Physical Review E 102, 052125 (2020).

[127] A. Erlebach, P. Nachtigall, and L. Grajciar, *Accurate large-scale simulations of siliceous zeolites by neural network potentials*, npj Computational Materials 8, 1–12 (2022).

[128] I. S. Novikov and A. V. Shapeev, *Improving accuracy of interatomic potentials: More physics or more data? A case study of silica*, Materials Today Communications 18, 74–80 (2019).

[129] K. Zongo, H. Sun, C. Ouellet-Plamondon, and L. K. Béland, *A unified moment tensor potential for silicon, oxygen, and silica*, arXiv:2311.15170 (2023).

[130] S. Sundararaman, L. Huang, S. Ispas, and W. Kob, *New optimization scheme to obtain interaction potentials for oxide glasses*, The Journal of Chemical Physics 148, 194504 (2018).

[131] M. J. Sanders, M. Leslie, and C. R. A. Catlow, *Interatomic potentials for SiO_2*, Journal of the Chemical Society, Chemical Communications, 1271–1273 (1984).

[132] H. Liu, Y. Li, Z. Fu, K. Li, and M. Bauchy, *Exploring the landscape of Buckingham potentials for silica by machine learning: Soft vs hard interatomic forcefields*, The Journal of Chemical Physics 152, 051101 (2020).

[133] Y. Qi, X. Guo, H. Wang, S. Zhang, M. Li, P. Zhou, and D. Guo, *Reversible densification and cooperative atomic movement induced "compaction" in vitreous silica: A new sight from deep neural network interatomic potentials*, Journal of Materials Science 58, 9515–9532 (2023).

[134] S. Takamoto, T. Kumagai, T. Yamasaki, T. Ohno, C. Kaneta, A. Hatano, and S. Izumi, *Charge-transfer interatomic potential for investigation of the thermal-oxidation growth process of silicon*, Journal of Applied Physics 120, 165109 (2016).

[135] E. Lee, K.-R. Lee, M. I. Baskes, and B.-J. Lee, *A modified embedded-atom method interatomic potential for ionic systems: 2NNMEAM+Qeq*, Physical Review B 93, 144110 (2016).

[136] L. Cvitkovich, F. Fehringer, C. Wilhelmer, D. Milardovich, D. Waldhör, and T. Grasser, *Machine Learning Force Field for Thermal Oxidation of Silicon*, arXiv:2405.13635 (2024).

[137] L. C. Erhard, J. Rohrer, K. Albe, and V. L. Deringer, *A machine-learned interatomic potential for silica and its relation to empirical models*, npj Computational Materials 8, 1–12 (2022).

[138] L. C. Erhard, J. Rohrer, K. Albe, and V. L. Deringer, *Modelling atomic and nanoscale structure in the silicon–oxygen system through active machine learning*, Nature Communications 15, 1927 (2024).

[139] A. Koneru, H. Chan, S. Manna, T. D. Loeffler, D. Dhabal, A. A. Bertolazzo, V. Molinero, and S. K. R. S. Sankaranarayanan, *Multi-reward reinforcement learning based development of inter-atomic potential models for silica*, npj Computational Materials 9, 1–13 (2023).

[140] K. Kobayashi, M. Okumura, H. Nakamura, M. Itakura, M. Machida, S. Urata, and K. Suzuya, *Machine learning molecular dynamics reveals the structural origin of the first sharp diffraction peak in high-density silica glasses*, Scientific Reports 13, 18721 (2023).

[141] E. B. Tadmor and R. E. Miller, *Modeling Materials: Continuum, Atomistic and Multiscale Techniques*, Cambridge University Press, November 2011.

[142] D. Frenkel and B. Smit, *Understanding molecular simulation: From algorithms to applications*, Elsevier, 2023.

[143] S. Sundararaman, L. Huang, S. Ispas, and W. Kob, *New interaction potentials for alkali and alkaline-earth aluminosilicate glasses*, The Journal of Chemical Physics 150, 154505 (2019).

[144] Y. Jia, H. Zhang, M. K. Shukla, S. Larson, S. Nouranian, A. M. Rajendran, and S. Jiang, *Mechanical behavior of alpha quartz with void defects under tension: A molecular dynamics study using different interatomic potentials*, Modelling and Simulation in Materials Science and Engineering 32, 025005 (2024).

[145] A. K. Rappe and W. A. Goddard, *Charge equilibration for molecular dynamics simulations*, J. Phys. Chem. 95, 3358–3363 (1991).

[146] T.-R. Shan, B. D. Devine, T. W. Kemper, S. B. Sinnott, and S. R. Phillpot, *Charge-optimized many-body potential for the hafnium/hafnium oxide system*, Physical Review B 81, 125328 (2010).

[147] K. de Boer, A. P. J. Jansen, R. A. van Santen, G. W. Watson, and S. C. Parker, *Free-energy calculations of thermodynamic, vibrational, elastic, and structural properties of \ensuremath{\alpha}-quartz at variable pressures and temperatures*, Physical Review B 54, 826–835 (1996).

[148] I. Saika-Voivod, F. Sciortino, T. Grande, and P. H. Poole, *Phase diagram of silica from computer simulation*, Physical Review E 70, 061507 (2004).

[149] D. Herzbach, K. Binder, and M. H. Müser, *Comparison of model potentials for molecular-dynamics simulations of silica*, The Journal of Chemical Physics 123, 124711 (2005).

[150] B. J. Cowen and M. S. El-Genk, *On force fields for molecular dynamics simulations of crystalline silica*, Computational Materials Science 107, 88–101 (2015).

[151] B. J. Cowen and M. S. El-Genk, *Bond-order reactive force fields for molecular dynamics simulations of crystalline silica*, Computational Materials Science 111, 269–276 (2016).

[152] A. P. Thompson, H. M. Aktulga, R. Berger, D. S. Bolintineanu, W. M. Brown, P. S. Crozier, P. J. in 't Veld, A. Kohlmeyer, S. G. Moore, T. D. Nguyen, R. Shan, M. J. Stevens, J. Tranchida, C. Trott, and S. J. Plimpton, *LAMMPS - a flexible simulation tool for particle-based materials modeling at the atomic, meso, and continuum scales*, Computer Physics Communications 271, 108171 (2022).

[153] M. J. Abraham, T. Murtola, R. Schulz, S. Páll, J. C. Smith, B. Hess, and E. Lindahl, *GROMACS: High performance molecular simulations through multi-level parallelism from laptops to supercomputers*, SoftwareX 1–2, 19–25 (2015).

[154] V. L. Deringer, M. A. Caro, and G. Csányi, *Machine Learning Interatomic Potentials as Emerging Tools for Materials Science*, Adv. Mater. 31, 1902765 (2019).

[155] J. Behler and M. Parrinello, *Generalized Neural-Network Representation of High-Dimensional Potential-Energy Surfaces*, Phys. Rev. Lett. 98, 146401 (2007).

[156] R. Drautz, *Atomic cluster expansion for accurate and transferable interatomic potentials*, Physical Review B 99, 014104 (2019).

[157] A. V. Shapeev, *Moment Tensor Potentials: A Class of Systematically Improvable Interatomic Potentials*, Multiscale Model. Simul. 14, 1153–1173 (2016).

[158] A. P. Bartók, M. C. Payne, R. Kondor, and G. Csányi, *Gaussian Approximation Potentials: The Accuracy of Quantum Mechanics, without the Electrons*, Phys. Rev. Lett. 104, 136403 (2010).

[159] H. Wang, L. Zhang, J. Han, and W. E, *DeePMD-kit: A deep learning package for many-body potential energy representation and molecular dynamics*, Computer Physics Communications 228, 178–184 (2018).

[160] K. T. Schütt, H. E. Sauceda, P.-J. Kindermans, A. Tkatchenko, and K.-R. Müller, *SchNet – A deep learning architecture for molecules and materials*, The Journal of Chemical Physics 148, 241722 (2018).

[161] A. Singraber, T. Morawietz, J. Behler, and C. Dellago, *Parallel Multistream Training of High-Dimensional Neural Network Potentials*, Journal of Chemical Theory and Computation 15, 3075–3092 (2019).

[162] A. Singraber, J. Behler, and C. Dellago, *Library-Based LAMMPS Implementation of High-Dimensional Neural Network Potentials*, Journal of Chemical Theory and Computation 15, 1827–1840 (2019).

[163] R. M. Martin, *Electronic Structure: Basic Theory and Practical Methods*, Cambridge University Press, Cambridge, 2004.

[164] J. Kohanoff, *Electronic Structure Calculations for Solids and Molecules: Theory and Computational Methods*, Cambridge University Press, Cambridge, 2006.

[165] S. Nosé, *A molecular dynamics method for simulations in the canonical ensemble*, Molecular Physics 52, 255–268 (1984).

[166] W. G. Hoover, *Canonical dynamics: Equilibrium phase-space distributions*, Phys. Rev. A 31, 1695–1697 (1985).

[167] W. Shinoda, M. Shiga, and M. Mikami, *Rapid estimation of elastic constants by molecular dynamics simulation under constant stress*, Physical Review B 69, 134103 (2004).

[168] M. E. Tuckerman, J. Alejandre, R. López-Rendón, A. L. Jochim, and G. J. Martyna, *A Liouville-operator derived measure-preserving integrator for molecular dynamics simulations in the isothermal–isobaric ensemble*, Journal of Physics A: Mathematical and General 39, 5629 (2006).

[169] R. Ravelo, B. L. Holian, T. C. Germann, and P. S. Lomdahl, *Constant-stress Hugoniostat method for following the dynamical evolution of shocked matter*, Physical Review B 70, 014103 (2004).

[170] H. J. Melosh, *Impact cratering : A geologic process*, New York : Oxford University Press ; Oxford : Clarendon Press (1989).

[171] J. W. Forbes, *Shock Wave Compression of Condensed Matter: A Primer*, Springer Berlin Heidelberg, Berlin, Heidelberg, 2012.

[172] S. Melchionna, G. Ciccotti, and B. Lee Holian, *Hoover NPT dynamics for systems varying in shape and size*, Molecular Physics 78, 533–544 (1993).

[173] W. G. Hoover, *Constant-pressure equations of motion*, Physical Review A 34, 2499–2500 (1986).

[174] J.-B. Maillet, M. Mareschal, L. Soulard, R. Ravelo, P. S. Lomdahl, T. C. Germann, and B. L. Holian, *Uniaxial Hugoniostat: A method for atomistic simulations of shocked materials*, Physical Review E 63, 016121 (2000).

[175] J. M. D. Lane, J. P. Koski, K. A. Jones, and T. J. Vogler, *Effect of initial temperature on compaction and strength of porous silica under shock compression*, Physical Review B 106, 094102 (2022).

[176] F. Birch, *Finite Elastic Strain of Cubic Crystals*, Physical Review 71, 809–824 (1947).

[177] T. Katsura and Y. Tange, *A Simple Derivation of the Birch–Murnaghan Equations of State (EOSs) and Comparison with EOSs Derived from Other Definitions of Finite Strain*, Minerals 9, 745 (2019).

[178] A. Togo, *First-principles Phonon Calculations with Phonopy and Phono3py*, Journal of the Physical Society of Japan 92, 012001 (2023).

[179] A. Togo, L. Chaput, T. Tadano, and I. Tanaka, *Implementation strategies in phonopy and phono3py*, Journal of Physics: Condensed Matter 35, 353001 (2023).

[180] D. Frenkel and A. J. C. Ladd, *New Monte Carlo method to compute the free energy of arbitrary solids. Application to the fcc and hcp phases of hard spheres*, The Journal of Chemical Physics 81, 3188–3193 (1984).

[181] S. Menon, Y. Lysogorskiy, J. Rogal, and R. Drautz, *Automated free-energy calculation from atomistic simulations*, Physical Review Materials 5, 103801 (2021).

[182] M. de Koning, *Optimizing the driving function for nonequilibrium free-energy calculations in the linear regime: A variational approach*, The Journal of Chemical Physics 122, 104106 (2005).

[183] D. Wallace, *Thermodynamics of Crystals*, Dover Books on Physics, Dover Publications, 1998.

[184] G. W. Ford and G. E. Uhlenbeck, *The theory of linear graphs with application to the theory of the virial development of the properties of gases*, Studies in statistical mechanics 1 (1962).

[185] R. Paula Leite, R. Freitas, R. Azevedo, and M. de Koning, *The Uhlenbeck-Ford model: Exact virial coefficients and application as a reference system in fluid-phase free-energy calculations*, The Journal of Chemical Physics 145, 194101 (2016).

[186] M. de Koning, A. Antonelli, and S. Yip, *Optimized Free-Energy Evaluation Using a Single Reversible-Scaling Simulation*, Physical Review Letters 83, 3973–3977 (1999).

[187] D. Sheppard, P. Xiao, W. Chemelewski, D. D. Johnson, and G. Henkelman, *A generalized solid-state nudged elastic band method*, The Journal of Chemical Physics 136, 074103 (2012).

[188] H. Jónsson, G. Mills, and K. W. Jacobsen, *Nudged elastic band method for finding minimum energy paths of transitions*, Classical and Quantum Dynamics in Condensed Phase Simulations (LERICI, Villa Marigola), WORLD SCIENTIFIC, June 1998, pp. 385–404.

[189] P. Xiao, J.-G. Cheng, J.-S. Zhou, J. B. Goodenough, and G. Henkelman, *Mechanism of the $CaIrO_3$ post-perovskite phase transition under pressure*, Physical Review B 88, 144102 (2013).

[190] A. Ghasemi, P. Xiao, and W. Gao, *Nudged elastic band method for solid-solid transition under finite deformation*, The Journal of Chemical Physics 151, 054110 (2019).

[191] W. Gao, https://github.com/Gao-Group/FD-NEB , 2023.

[192] R. Terrell, S. Chill, P. Xiao, J. Duncan, S. Stauffer, R. Bandy, and J. Janssen, https://theory.cm.utexas.edu/tsase/.

[193] P. Debye, *Zerstreuung von Röntgenstrahlen*, Annalen der Physik 351, 809–823 (1915).

[194] A. Stukowski, *Visualization and analysis of atomistic simulation data with OVITO–the Open Visualization Tool*, Modelling Simul. Mater. Sci. Eng. 18, 015012 (2010).

[195] A. Leonardi and D. L. Bish, *High-performance powder diffraction pattern simulation for large-scale atomistic models* via *full-precision pair distribution function computation*, Journal of Applied Crystallography 49, 1593–1608 (2016).

[196] T. Egami and S. J. L. Billinge, *Underneath the Bragg Peaks: Structural Analysis of Complex Materials*, Newnes, December 2012.

[197] Q. Mei, C. J. Benmore, S. Sen, R. Sharma, and J. L. Yarger, *Intermediate range order in vitreous silica from a partial structure factor analysis*, Physical Review B 78, 144204 (2008).

[198] T. E. Faber and J. M. Ziman, *A theory of the electrical properties of liquid metals*, The Philosophical Magazine: A Journal of Theoretical Experimental and Applied Physics 11, 153–173 (1965).

[199] P. J. Brown, A. G. Fox, E. N. Maslen, M. A. O'Keefe, and B. T. M. Willis, *Intensity of diffracted intensities*, International Tables for Crystallography Volume C: Mathematical, Physical and Chemical Tables (E. Prince, ed.), Springer Netherlands, Dordrecht, 2004, pp. 554–595.

[200] L. C. Erhard, D. Utt, A. J. Klomp, and K. Albe, *Crystal structure identification with 3D convolutional neural networks with application to high-pressure phase transitions in SiO_2*, Modelling and Simulation in Materials Science and Engineering 32, 065029 (2024).

[201] P. M. Larsen, S. Schmidt, and J. Schiøtz, *Robust structural identification via polyhedral template matching*, Modelling and Simulation in Materials Science and Engineering 24, 055007 (2016).

[202] J. Dana. Honeycutt and H. C. Andersen, *Molecular dynamics study of melting and freezing of small Lennard-Jones clusters*, The Journal of Physical Chemistry 91, 4950–4963 (1987).

[203] A. Ziletti, D. Kumar, M. Scheffler, and L. M. Ghiringhelli, *Insightful classification of crystal structures using deep learning*, Nature Communications 9, 2775 (2018).

[204] A. Leitherer, A. Ziletti, and L. M. Ghiringhelli, *Robust recognition and exploratory analysis of crystal structures via Bayesian deep learning*, Nature Communications 12, 6234 (2021).

[205] H. W. Chung, R. Freitas, G. Cheon, and E. J. Reed, *Data-centric framework for crystal structure identification in atomistic simulations using machine learning*, Physical Review Materials 6, 043801 (2022).

[206] R. S. DeFever, C. Targonski, S. W. Hall, M. C. Smith, and S. Sarupria, *A generalized deep learning approach for local structure identification in molecular simulations*, Chemical Science 10, 7503–7515 (2019).

[207] Y. Wang, Y. Sun, Z. Liu, S. E. Sarma, M. M. Bronstein, and J. M. Solomon, *Dynamic Graph CNN for Learning on Point Clouds*, ACM Transactions on Graphics 38, 146:1–146:12 (2019).

[208] H. d'Amour, W. Denner, and H. Schulz, *Structure determination of α-quartz up to 68 x 10^8 Pa*, Acta Crystallographica Section B: Structural Crystallography and Crystal Chemistry 35, 550–555 (1979).

[209] R. T. Downs and D. C. Palmer, *The pressure behavior of α cristobalite*, American Mineralogist 79, 9–14 (1994).

[210] G. Miehe and H. Graetsch, *Crystal structure of moganite: A new structure type for silica*, European Journal of Mineralogy 4, 693–706 (1992).

[211] H. Graetsch and I. Topalovic-Dierdorf, *29Si MAS NMR spectrum and superstructure of modulated tridymite L3-To(MX-1)*, European Journal of Mineralogy 8, 103–114 (1996).

[212] J. S. Tse, D. D. Klug, and Y. Le Page, *High-pressure densification of amorphous silica*, Physical Review B 46, 5933–5938 (1992).

[213] I. M. Svishchev, P. G. Kusalik, and V. V. Murashov, *Orthorhombic quartzlike polymorph of silica: A molecular-dynamics simulation study*, Physical Review B 55, 721–725 (1997).

[214] A. Kirfel and G. Will, *Ending the "P21/a coesite„ discussion*, Zeitschrift für Kristallographie - Crystalline Materials 167, 287–292 (1984).

[215] N. R. Keskar and J. R. Chelikowsky, *Structural properties of nine silica polymorphs*, Phys. Rev. B 46, 1–13 (1992).

[216] L. Zhang, D. Popov, Y. Meng, J. Wang, C. Ji, B. Li, and H.-k. Mao, *In-situ crystal structure determination of seifertite SiO_2 at 129 GPa: Studying a minor phase near Earth's core–mantle boundary*, American Mineralogist 101, 231–234 (2016).

[217] K. Vollmayr, W. Kob, and K. Binder, *Cooling-rate effects in amorphous silica: A computer-simulation study*, Physical Review B 54, 15808–15827 (1996).

[218] Y. Shen, S. B. Jester, T. Qi, and E. J. Reed, *Nanosecond homogeneous nucleation and crystal growth in shock-compressed SiO_2*, Nature Materials 15, 60–65 (2016).

[219] J. Tersoff, *Empirical interatomic potential for silicon with improved elastic properties*, Phys. Rev. B 38, 9902–9905 (1988).

[220] J. Tersoff, *Modeling solid-state chemistry: Interatomic potentials for multicomponent systems*, Physical Review B 39, 5566–5568 (1989).

[221] S. W. Rick, S. J. Stuart, and B. J. Berne, *Dynamical fluctuating charge force fields: Application to liquid water*, The Journal of Chemical Physics 101, 6141–6156 (1994).

[222] G. Nikoulis, J. Byggmästar, J. Kioseoglou, K. Nordlund, and F. Djurabekova, *Machine-learning interatomic potential for W–Mo alloys*, Journal of Physics: Condensed Matter 33, 315403 (2021).

[223] W. J. Szlachta, A. P. Bartók, and G. Csányi, *Accuracy and transferability of Gaussian approximation potential models for tungsten*, Physical Review B 90, 104108 (2014).

[224] L. Tang, Z. J. Yang, T. Q. Wen, K. M. Ho, M. J. Kramer, and C. Z. Wang, *Development of interatomic potential for Al–Tb alloys using a deep neural network learning method*, Physical Chemistry Chemical Physics 22, 18467–18479 (2020).

[225] V. L. Deringer and G. Csányi, *Machine learning based interatomic potential for amorphous carbon*, Physical Review B 95, 094203 (2017).

[226] N. Jakse, J. Sandberg, L. F. Granz, A. Saliou, P. Jarry, E. Devijver, T. Voigtmann, J. Horbach, and A. Meyer, *Machine learning interatomic potentials for aluminium: Application to solidification phenomena*, Journal of Physics: Condensed Matter 35, 035402 (2022).

[227] T. A. Young, T. Johnston-Wood, H. Zhang, and F. Duarte, *Reaction dynamics of Diels–Alder reactions from machine learned potentials*, Physical Chemistry Chemical Physics 24, 20820–20827 (2022).

[228] I. Y. Zhang and A. Grüneis, *Coupled Cluster Theory in Materials Science*, Frontiers in Materials 6 (2019).

[229] T. Demuth, Y. Jeanvoine, J. Hafner, and J. G. Ángyán, *Polymorphism in silica studied in the local density and generalized-gradient approximations*, J. Phys.: Condens. Matter 11, 3833–3874 (1999).

[230] D. Zagorac, H. Müller, S. Ruehl, J. Zagorac, and S. Rehme, *Recent developments in the Inorganic Crystal Structure Database: Theoretical crystal structure data and related features*, Journal of Applied Crystallography 52, 918–925 (2019).

[231] V. L. Deringer, D. M. Proserpio, G. Csányi, and C. J. Pickard, *Data-driven learning and prediction of inorganic crystal structures*, Faraday Discussions 211, 45–59 (2018).

[232] H. Eshet, R. Z. Khaliullin, T. D. Kühne, J. Behler, and M. Parrinello, *Ab initio quality neural-network potential for sodium*, Physical Review B 81, 184107 (2010).

[233] G. C. Sosso, G. Miceli, S. Caravati, J. Behler, and M. Bernasconi, *Neural network interatomic potential for the phase change material GeTe*, Physical Review B 85, 174103 (2012).

[234] N. Artrith and J. Behler, *High-dimensional neural network potentials for metal surfaces: A prototype study for copper*, Physical Review B 85, 045439 (2012).

[235] J. Vandermause, S. B. Torrisi, S. Batzner, Y. Xie, L. Sun, A. M. Kolpak, and B. Kozinsky, *On-the-fly active learning of interpretable Bayesian force fields for atomistic rare events*, npj Computational Materials 6, 1–11 (2020).

[236] R. Jinnouchi, F. Karsai, and G. Kresse, *On-the-fly machine learning force field generation: Application to melting points*, Physical Review B 100, 014105 (2019).

[237] Y. Lysogorskiy, A. Bochkarev, M. Mrovec, and R. Drautz, *Active learning strategies for atomic cluster expansion models*, Physical Review Materials 7, 043801 (2023).

[238] K. Gubaev, E. V. Podryabinkin, and A. V. Shapeev, *Machine learning of molecular properties: Locality and active learning*, The Journal of Chemical Physics 148, 241727 (2018).

[239] E. V. Podryabinkin and A. V. Shapeev, *Active learning of linearly parametrized interatomic potentials*, Computational Materials Science 140, 171–180 (2017).

[240] E. Podryabinkin, K. Garifullin, A. Shapeev, and I. Novikov, *MLIP-3: Active learning on atomic environments with moment tensor potentials*, The Journal of Chemical Physics 159, 084112 (2023).

[241] C. van der Oord, M. Sachs, D. P. Kovács, C. Ortner, and G. Csányi, *Hyperactive learning for data-driven interatomic potentials*, npj Computational Materials 9, 1–14 (2023).

[242] M. Hodapp and A. Shapeev, *In operando active learning of interatomic interaction during large-scale simulations*, Machine Learning: Science and Technology 1, 045005 (2020).

[243] L. Kong, J. Li, L. Sun, H. Yang, H. Hao, C. Chen, N. Artrith, J. A. G. Torres, Z. Lu, and Y. Zhou, *Overcoming the Size Limit of First Principles Molecular Dynamics Simulations with an In-Distribution Substructure Embedding Active Learner*, arXiv:2311.08177 (2023).

[244] J. Behler, *Atom-centered symmetry functions for constructing high-dimensional neural network potentials*, The Journal of Chemical Physics 134, 074106 (2011).

[245] N. Artrith and A. Urban, *An implementation of artificial neural-network potentials for atomistic materials simulations: Performance for TiO_2*, Computational Materials Science 114, 135–150 (2016).

[246] V. L. Deringer, A. P. Bartók, N. Bernstein, D. M. Wilkins, M. Ceriotti, and G. Csányi, *Gaussian Process Regression for Materials and Molecules*, Chemical Reviews 121, 10073–10141 (2021).

[247] A. Thompson, L. Swiler, C. Trott, S. Foiles, and G. Tucker, *Spectral neighbor analysis method for automated generation of quantum-accurate interatomic potentials*, Journal of Computational Physics 285, 316–330 (2015).

[248] D. P. Kovács, C. van der Oord, J. Kucera, A. E. A. Allen, D. J. Cole, C. Ortner, and G. Csányi, *Linear Atomic Cluster Expansion Force Fields for Organic Molecules: Beyond RMSE*, Journal of Chemical Theory and Computation 17, 7696–7711 (2021).

[249] Y. Lysogorskiy, C. van der Oord, A. Bochkarev, S. Menon, M. Rinaldi, T. Hammerschmidt, M. Mrovec, A. Thompson, G. Csányi, C. Ortner, and R. Drautz, *Performant implementation of the atomic cluster expansion (PACE) and application to copper and silicon*, npj Computational Materials 7, 1–12 (2021).

[250] M. A. Wood and A. P. Thompson, *Extending the accuracy of the SNAP interatomic potential form*, The Journal of Chemical Physics 148, 241721 (2018).

[251] A. Lomaka and T. Tamm, *Linearization of moment tensor potentials for multicomponent systems with a preliminary assessment for short-range interaction energy in water dimer and trimer*, The Journal of Chemical Physics 152, 164115 (2020).

[252] K. Gubaev, E. V. Podryabinkin, G. L. Hart, and A. V. Shapeev, *Accelerating high-throughput searches for new alloys with active learning of interatomic potentials*, Computational Materials Science 156, 148–156 (2019).

[253] Y. Zuo, C. Chen, X. Li, Z. Deng, Y. Chen, J. Behler, G. Csányi, A. V. Shapeev, A. P. Thompson, M. A. Wood, and S. P. Ong, *Performance and Cost Assessment of Machine Learning Interatomic Potentials*, J. Phys. Chem. A 124, 731–745 (2020).

[254] P. Rowe, V. L. Deringer, P. Gasparotto, G. Csányi, and A. Michaelides, *An accurate and transferable machine learning potential for carbon*, The Journal of Chemical Physics 153, 034702 (2020).

[255] Z. Deng, C. Chen, X.-G. Li, and S. P. Ong, *An electrostatic spectral neighbor analysis potential for lithium nitride*, npj Computational Materials 5, 1–8 (2019).

[256] N. Artrith, T. Morawietz, and J. Behler, *High-dimensional neural-network potentials for multicomponent systems: Applications to zinc oxide*, Physical Review B 83, 153101 (2011).

[257] T. W. Ko, J. A. Finkler, S. Goedecker, and J. Behler, *A fourth-generation high-dimensional neural network potential with accurate electrostatics including non-local charge transfer*, Nature Communications 12, 398 (2021).

[258] G. Csányi, S. Winfield, J. Kermode, M. C. Payne, A. Comisso, A. De Vita, and N. Bernstein, *Expressive programming for computational physics in Fortran 950+*, Newsletter of the Computational Physics Group, 1–24 (2007).

[259] J. R. Kermode, *F90wrap: An automated tool for constructing deep Python interfaces to modern Fortran codes*, Journal of Physics: Condensed Matter 32, 305901 (2020).

[260] S. N. Pozdnyakov, M. J. Willatt, A. P. Bartók, C. Ortner, G. Csányi, and M. Ceriotti, *Incompleteness of Atomic Structure Representations*, Physical Review Letters 125, 166001 (2020).

[261] G. Dusson, M. Bachmayr, G. Csányi, R. Drautz, S. Etter, C. van der Oord, and C. Ortner, *Atomic cluster expansion: Completeness, efficiency and stability*, Journal of Computational Physics 454, 110946 (2022).

[262] I. S. Novikov, K. Gubaev, E. V. Podryabinkin, and A. V. Shapeev, *The MLIP package: Moment tensor potentials with MPI and active learning*, Machine Learning: Science and Technology 2, 025002 (2021).

[263] R. Drautz and M. Fähnle, *Spin-cluster expansion: Parametrization of the general adiabatic magnetic energy surface with ab initio accuracy*, Physical Review B 69, 104404 (2004).

[264] J. M. Sanchez, F. Ducastelle, and D. Gratias, *Generalized cluster description of multicomponent systems*, Physica A: Statistical Mechanics and its Applications 128, 334–350 (1984).

[265] M. W. Finnis and J. E. Sinclair, *A simple empirical N-body potential for transition metals*, Philosophical Magazine A 50, 45–55 (1984).

[266] A. Bochkarev, Y. Lysogorskiy, S. Menon, M. Qamar, M. Mrovec, and R. Drautz, *Efficient parametrization of the atomic cluster expansion*, Physical Review Materials 6, 013804 (2022).

[267] M. Born and R. Oppenheimer, *Zur Quantentheorie der Molekeln*, Annalen der Physik 389, 457–484 (1927).

[268] P. Hohenberg and W. Kohn, *Inhomogeneous Electron Gas*, Phys. Rev. 136, B864–B871 (1964).

[269] W. Kohn and L. J. Sham, *Self-Consistent Equations Including Exchange and Correlation Effects*, Phys. Rev. 140, A1133–A1138 (1965).

[270] J. P. Perdew and Y. Wang, *Accurate and simple analytic representation of the electron-gas correlation energy*, Phys. Rev. B 45, 13244–13249 (1992).

[271] J. P. Perdew and A. Zunger, *Self-interaction correction to density-functional approximations for many-electron systems*, Physical Review B 23, 5048–5079 (1981).

[272] J. P. Perdew, K. Burke, and M. Ernzerhof, *Generalized Gradient Approximation Made Simple*, Phys. Rev. Lett. 77, 3865–3868 (1996).

[273] J. P. Perdew, A. Ruzsinszky, G. I. Csonka, O. A. Vydrov, G. E. Scuseria, L. A. Constantin, X. Zhou, and K. Burke, *Restoring the Density-Gradient Expansion for Exchange in Solids and Surfaces*, Phys. Rev. Lett. 100, 136406 (2008).

[274] J. Sun, A. Ruzsinszky, and J. P. Perdew, *Strongly Constrained and Appropriately Normed Semilocal Density Functional*, Physical Review Letters 115, 036402 (2015).

[275] E. B. Isaacs and C. Wolverton, *Performance of the strongly constrained and appropriately normed density functional for solid-state materials*, Physical Review Materials 2, 063801 (2018).

[276] G. Kresse and J. Furthmüller, *Efficiency of ab-initio total energy calculations for metals and semiconductors using a plane-wave basis set*, Computational Materials Science 6, 15–50 (1996).

[277] G. Kresse and J. Furthmüller, *Efficient iterative schemes for ab initio total-energy calculations using a plane-wave basis set*, Physical Review B 54, 11169–11186 (1996).

[278] P. E. Blöchl, *Projector augmented-wave method*, Physical Review B 50, 17953–17979 (1994).

[279] G. Kresse and D. Joubert, *From ultrasoft pseudopotentials to the projector augmented-wave method*, Physical Review B 59, 1758–1775 (1999).

[280] A. H. Larsen, J. J. Mortensen, J. Blomqvist, I. E. Castelli, R. Christensen, M. Dulak, J. Friis, M. N. Groves, B. Hammer, C. Hargus, E. D. Hermes, P. C. Jennings, P. B. Jensen, J. Kermode, J. R. Kitchin, E. L. Kolsbjerg, J. Kubal, K. Kaasbjerg, S. Lysgaard, J. B. Maronsson, T. Maxson, T. Olsen, L. Pastewka, A. Peterson, C. Rostgaard, J. Schiøtz, O. Schütt, M. Strange, K. S. Thygesen, T. Vegge, L. Vilhelmsen, M. Walter, Z. Zeng, and K. W. Jacobsen, *The atomic simulation environment—a Python library for working with atoms*, J. Phys.: Condens. Matter 29, 273002 (2017).

[281] C. R. Harris, K. J. Millman, S. J. van der Walt, R. Gommers, P. Virtanen, D. Cournapeau, E. Wieser, J. Taylor, S. Berg, N. J. Smith, R. Kern, M. Picus, S. Hoyer, M. H. van Kerkwijk, M. Brett, A. Haldane, J. F. del Río, M. Wiebe, P. Peterson, P. Gérard-Marchant, K. Sheppard, T. Reddy, W. Weckesser, H. Abbasi, C. Gohlke, and T. E. Oliphant, *Array programming with NumPy*, Nature 585, 357–362 (2020).

[282] P. Virtanen, R. Gommers, T. E. Oliphant, M. Haberland, T. Reddy, D. Cournapeau, E. Burovski, P. Peterson, W. Weckesser, J. Bright, S. J. van der Walt, M. Brett, J. Wilson, K. J. Millman, N. Mayorov, A. R. J. Nelson, E. Jones, R. Kern, E. Larson, C. J. Carey, İ. Polat, Y. Feng, E. W. Moore, J. VanderPlas, D. Laxalde, J. Perktold, R. Cimrman, I. Henriksen, E. A. Quintero, C. R. Harris, A. M. Archibald, A. H. Ribeiro, F. Pedregosa, and P. van Mulbregt, *SciPy 1.0: Fundamental algorithms for scientific computing in Python*, Nature Methods 17, 261–272 (2020).

[283] J. D. Hunter, *Matplotlib: A 2D Graphics Environment*, Computing in Science & Engineering 9, 90–95 (2007).

[284] S. P. Ong, W. D. Richards, A. Jain, G. Hautier, M. Kocher, S. Cholia, D. Gunter, V. L. Chevrier, K. A. Persson, and G. Ceder, *Python Materials Genomics (pymatgen): A robust, open-source python library for materials analysis*, Computational Materials Science 68, 314–319 (2013).

[285] L. C. Erhard, J. Rohrer, K. Albe, and V. L. Deringer, *Research data for "A machine-learned interatomic potential for silica and its relation to empirical models"*, Zenodo: 10.5281/zenodo.6353684 (2022).

[286] L. Erhard, J. Rohrer, K. Albe, and V. Deringer, *Research data for "Modelling atomic and nanoscale structure in the silicon-oxygen system through active machine-learning"*, Zenodo: 10.5281/zenodo.10419194 (2024).

[287] L. C. Erhard, D. Utt, A. J. Klomp, and K. Albe, *Research data for "Crystal structure identification with 3D convolutional neural networks with application to high-pressure phase transitions in SiO_2"*, tudatalib: 10.48328/tudatalib-1394 (2024).

[288] M.-J. Díaz-Cabañas and P. A. Barrett, *Synthesis and structure of pure SiO_2 chabazite: The SiO_2 polymorph with the lowest framework density*, Chem. Commun. 17, 1881–1882 (1998).

[289] K. Kato and A. Nukui, *Die Kristallstruktur des monoklinen Tief-Tridymits*, Acta Crystallogr B Struct Crystallogr Cryst Chem 32, 2486–2491 (1976).

[290] A. F. Wright and A. J. Leadbetter, *The structures of the β-cristobalite phases of SiO_2 and $AlPO_4$*, Philosophical Magazine 31, 1391–1401 (1975).

[291] A. Khlapova, *X-Ray Data on the α-to β-Quartz Phase Transition*, Soviet Physics, Crystallography 7, 458–463 (1962).

[292] K. Kihara, T. Matsumoto, and M. Imamura, *High-order thermal-motion tensor analyses of tridymite*, Zeitschrift für Kristallographie - Crystalline Materials 177, 39–52 (1986).

[293] K. Kihara, *An orthrohombic superstructure of tridymite existing between about 105 and 180°C*, Zeitschrift für Kristallographie - Crystalline Materials 146, 185–203 (1977).

[294] A. P. Bartók, J. Kermode, N. Bernstein, and G. Csányi, *Machine Learning a General-Purpose Interatomic Potential for Silicon*, Physical Review X 8, 041048 (2018).

[295] L. Himanen, M. O. J. Jäger, E. V. Morooka, F. Federici Canova, Y. S. Ranawat, D. Z. Gao, P. Rinke, and A. S. Foster, *DScribe: Library of descriptors for machine learning in materials science*, Computer Physics Communications 247, 106949 (2020).

[296] R. Bechmann, *Elastic and Piezoelectric Constants of Alpha-Quartz*, Physical Review 110, 1060–1061 (1958).

[297] A. Yeganeh-Haeri, D. J. Weidner, and J. B. Parise, *Elasticity of α-Cristobalite: A Silicon Dioxide with a Negative Poisson's Ratio*, Science 257, 650–652 (1992).

[298] D. J. Weidner and H. R. Carleton, *Elasticity of coesite*, Journal of Geophysical Research (1896-1977) 82, 1334–1346 (1977).

[299] D. J. Weidner, J. D. Bass, A. E. Ringwood, and W. Sinclair, *The single-crystal elastic moduli of stishovite*, Journal of Geophysical Research: Solid Earth 87, 4740–4746 (1982).

[300] P. Heyliger, H. Ledbetter, and S. Kim, *Elastic constants of natural quartz*, The Journal of the Acoustical Society of America 114, 644–650 (2003).

[301] L. Levien, C. T. Prewitt, and D. J. Weidner, *Structure and elastic properties of quartz at pressure*, American Mineralogist 65, 920–930 (1980).

[302] L.-g. Liu, *Bulk moduli of SiO_2 polymorphs: Quartz, coesite and stishovite*, Mechanics of Materials 14, 283–290 (1993).

[303] J.-M. Léger, J. Haines, and C. Chateau, *The high-pressure behaviour of the "moganite" polymorph of SiO_2*, European Journal of Mineralogy 13, 351–359 (2001).

[304] B. Dorner, H. Grimm, and H. Rzany, *Phonon dispersion branches in α-quartz*, Journal of Physics C: Solid State Physics 13, 6607 (1980).

[305] Q. Mei, C. J. Benmore, and J. K. R. Weber, *Structure of Liquid SiO_2: A Measurement by High-Energy X-Ray Diffraction*, Physical Review Letters 98, 057802 (2007).

[306] P. Richet, Y. Bottinga, L. Denielou, J. Petitet, and C. Tequi, *Thermodynamic properties of quartz, cristobalite and amorphous SiO_2: Drop calorimetry measurements between 1000 and 1800 K and a review from 0 to 2000 K*, Geochimica et Cosmochimica Acta 46, 2639–2658 (1982).

[307] S. S. Wise, J. L. Margrave, H. M. Feder, and W. N. Hubbard, *FLUORINE BOMB CALORIMETRY. V. THE HEATS OF FORMATION OF SILICON TETRAFLUORIDE AND SILICA* [1,2], The Journal of Physical Chemistry 67, 815–821 (1963).

[308] W. A. Roth and H. Troitzsch, *Beitrag zur Thermochemie der Kieselsäure und einiger Silikate*, Zeitschrift für anorganische Chemie 260, 337–344 (1949).

[309] A. C. Wright, *Crystalline-like ordering in melt-quenched network glasses?*, Journal of Non-Crystalline Solids 401, 4–26 (2014).

[310] M. F. Calegari Andrade and A. Selloni, *Structure of disordered TiO_2 phases from ab initio based deep neural network simulations*, Physical Review Materials 4, 113803 (2020).

[311] G. Sivaraman, L. Gallington, A. N. Krishnamoorthy, M. Stan, G. Csányi, Á. Vázquez-Mayagoitia, and C. J. Benmore, *Experimentally Driven Automated Machine-Learned Interatomic Potential for a Refractory Oxide*, Physical Review Letters 126, 156002 (2021).

[312] S. Sakaguchi, *Evaluation of the critical cooling rate in glass-forming materials based on viscosity*, Journal of Non-Crystalline Solids 185, 268–273 (1995).

[313] L. C. Gallington, Y. Ghadar, L. B. Skinner, J. K. R. Weber, S. V. Ushakov, A. Navrotsky, A. Vazquez-Mayagoitia, J. C. Neuefeind, M. Stan, J. J. Low, and C. J. Benmore, *The Structure of Liquid and Amorphous Hafnia*, Materials 10, 1290 (2017).

[314] V. Petkov, G. Holzhüter, U. Tröge, T. Gerber, and B. Himmel, *Atomic-scale structure of amorphous TiO_2 by electron, X-ray diffraction and reverse Monte Carlo simulations*, Journal of Non-Crystalline Solids 231, 17–30 (1998).

[315] N. Leimeroth, J. Rohrer, and K. Albe, *General purpose potential for glassy and crystalline phases of Cu-Zr alloys based on the ACE formalism*, Physical Review Materials 8, 043602 (2024).

[316] D. M. Teter, G. V. Gibbs, M. B. Boisen, D. C. Allan, and M. P. Teter, *First-principles study of several hypothetical silica framework structures*, Phys. Rev. B 52, 8064–8073 (1995).

[317] S. Ono, K. Hirose, M. Murakami, and M. Isshiki, *Post-stishovite phase boundary in SiO_2 determined by in situ X-ray observations*, Earth and Planetary Science Letters 197, 187–192 (2002).

[318] S. Petitgirard, C. Sahle, C. Weis, K. Gilmore, G. Spiekermann, J. Tse, M. Wilke, C. Cavallari, V. Cerantola, and C. Sternemann, *Magma properties at deep Earth's conditions from electronic structure of silica*, Geochemical Perspectives Letters, 32–37 (2019).

[319] P. Beck, P. Gillet, A. El Goresy, and S. Mostefaoui, *Timescales of shock processes in chondritic and martian meteorites*, Nature 435, 1071–1074 (2005).

[320] A. Togo and I. Tanaka, *Spglib: A software library for crystal symmetry search*, arXiv:1808.01590 (2018).

[321] M. Nagamori, J. A. Boivin, and A. Claveau, *Gibbs free energies of formation of amorphous Si_2O_3, SiO and Si_2O*, Journal of Non-Crystalline Solids 189, 270–276 (1995).

[322] F. T. Ferguson and J. A. Nuth, *Vapor Pressure of Silicon Monoxide*, Journal of Chemical & Engineering Data 53, 2824–2832 (2008).

[323] M. Mamiya, H. Takei, M. Kikuchi, and C. Uyeda, *Preparation of fine silicon particles from amorphous silicon monoxide by the disproportionation reaction*, Journal of Crystal Growth 229, 457–461 (2001).

[324] S. Batzner, A. Musaelian, L. Sun, M. Geiger, J. P. Mailoa, M. Kornbluth, N. Molinari, T. E. Smidt, and B. Kozinsky, *E(3)-equivariant graph neural networks for data-efficient and accurate interatomic potentials*, Nature Communications 13, 2453 (2022).

[325] I. Batatia, D. P. Kovacs, G. Simm, C. Ortner, and G. Csanyi, *MACE: Higher order equivariant message passing neural networks for fast and accurate force fields*, Advances in Neural Information Processing Systems (S. Koyejo, S. Mohamed, A. Agarwal, D. Belgrave, K. Cho, and A. Oh, eds.), vol. 35, Curran Associates, Inc., 2022, pp. 11423–11436.

[326] B. Deng, P. Zhong, K. Jun, J. Riebesell, K. Han, C. J. Bartel, and G. Ceder, *CHGNet as a pretrained universal neural network potential for charge-informed atomistic modelling*, Nature Machine Intelligence 5, 1031–1041 (2023).

[327] B. Kalita, L. Li, R. J. McCarty, and K. Burke, *Learning to Approximate Density Functionals*, Accounts of Chemical Research 54, 818–826 (2021).

[328] D. C. Palmer and L. W. Finger, *Pressure-induced phase transition in cristobalite: An X-ray powder diffraction study to 4.4 GPa*, American Mineralogist 79, 1–8 (1994).

[329] Y. Tsuchida and T. Yagi, *New pressure-induced transformations of silica at room temperature*, Nature 347, 267–269 (1990).

[330] A. Černok, K. Marquardt, R. Caracas, E. Bykova, G. Habler, H.-P. Liermann, M. Hanfland, M. Mezouar, E. Bobocioiu, and L. Dubrovinsky, *Compressional pathways of α-cristobalite, structure of cristobalite X-I, and towards the understanding of seifertite formation*, Nature Communications 8, 15647 (2017).

[331] L. S. Dubrovinsky, N. A. Dubrovinskaia, S. K. Saxena, F. Tutti, S. Rekhi, T. Le Bihan, G. Shen, and J. Hu, *Pressure-induced transformations of cristobalite*, Chemical Physics Letters 333, 264–270 (2001).

[332] T. Kubo, T. Kato, Y. Higo, and K.-i. Funakoshi, *Curious kinetic behavior in silica polymorphs solves seifertite puzzle in shocked meteorite*, Science Advances 1, e1500075 (2015).

[333] T. G. Sharp, A. E. Goresy, B. Wopenka, and M. Chen, *A Post-Stishovite SiO_2 Polymorph in the Meteorite Shergotty: Implications for Impact Events*, Science 284, 1511–1513 (1999).

[334] A. E. l. D. Goresy, T. G. Sharp, C. T. Prewitt, M. Chen, L. Dubrovinsky, B. Wopenka, N. Z. Boctor, and R. J. Hemley, *Seifertite, a dense orthorhombic polymorph of silica from the Martian meteorites Shergotty and Zagami*, European Journal of Mineralogy, 523–528 (2008).

[335] M. Miyahara, S. Kaneko, E. Ohtani, T. Sakai, T. Nagase, M. Kayama, H. Nishido, and N. Hirao, *Discovery of seifertite in a shocked lunar meteorite*, Nature Communications 4, 1737 (2013).

[336] D. Stöffler, R. Ostertag, C. Jammes, G. Pfannschmidt, P. R. S. Gupta, S. B. Simon, J. J. Papike, and R. H. Beauchamp, *Shock metamorphism and petrography of the Shergotty achondrite*, Geochimica et Cosmochimica Acta 50, 889–903 (1986).

[337] C. Zhang, L. Tang, Y. Sun, K.-M. Ho, R. M. Wentzcovitch, and C.-Z. Wang, *Deep machine learning potential for atomistic simulation of Fe-Si-O systems under Earth's outer core conditions*, Physical Review Materials 6, 063802 (2022).

[338] J. Deng, H. Niu, J. Hu, M. Chen, and L. Stixrude, *Melting of $MgSiO_3$ determined by machine learning potentials*, Physical Review B 107, 064103 (2023).